博士論文

Investigation on Grating-Based Dielectric Laser Accelerator Structures

（回折格子中におけるレーザー駆動誘電体加速器の構造の研究）

陳 昭福（Chen Zhaofu）

Abstract

Dielectric laser accelerator (DLA) is an advanced acceleration technique that has demonstrated high accelerating gradients at the GV/m level, 1 to 2 orders of magnitude above the ultimate gradient limit of conventional radio-frequency accelerators. Leveraging the well-developed industrial nanofabrication technology and commercial ultrafast laser technique, DLAs may enable more compact and more affordable accelerators. For these reasons, a DLA-based electron source has been proposed to study the damage effect of low radiation doses on the living cell. This thesis focuses on the development of DLA structures for such an electron source.

First, we describe a method to design a double-grating resonator for subrelativistic electron acceleration and present the development of a test station. We begin with the theory behind particle acceleration using single or double diffraction gratings. We show that a uniform accelerating mode can be obtained in a resonant double-grating structure. We present simulated examples of double-grating resonators for 50 keV electrons with different channel widths. We show that the dependence of reflectivity and phase on the SWG dimensions provides flexibility in controlling the enhancement factor and filling time, thus enabling high gradient acceleration driven by ultrashort low-power laser pulses. An appendix is included to describe the rigorous coupled-wave analysis as a method for grating field simulation. We estimate the parameters of a 1 MeV DLA electron source. In addition, we show the design of the experiments, in particular, the magnets for electron beam focusing and energy measurement. All the components for the experiment have been fabricated.

We also discuss a planar DLA waveguide which can accelerate electrons of different energies, using subwavelength gratings as reflectors. We show that an accelerating mode with a specified field distribution can be confined in the core by designing a matching layer. We present several examples of DLA waveguides with gratings for relativistic electron acceleration. We then discuss the waveguide performance regarding accelerating gradient and efficiency.

The DLA structures described in this work can support high-gradient acceleration with ultrafast laser pulses. They may enable a compact monolithically-integrated electron source, which is useful not only for radiobiology research, but also for a variety of other applications such as radiotherapy, material science, and high-energy physics.

Acknowledgements

This thesis would not be possible without the help of many talented and inspirational people who supported me during these years.

First and foremost, I would like to thank my advisor, Professor Mitsuru Uesaka. He trusted me and gave me the great freedom to pursue the aspects of this project I found most interesting. He taught me many lessons on the working of research. His leadership helped me to learn how to cooperate with others as a researcher. His great mind to promote human progress made me better realize the responsibility as a social being. His suggestions made me stronger and more mature.

I would like to thank Professor Kazuyoshi Koyama. His passion for research was contagious and his knowledge limitless. He was always willing to offer his insights and advice. He helped me in almost every aspect of the work. Most of the test station design would not be possible without his direct efforts. He also encouraged me to exchange ideas with colleagues and thoroughly edited my papers, which pushed my work to a higher level.

I would also like to thank Mitsuhiro Yoshida at KEK. He is one of the best scientific researchers I have ever seen. His knowledge impressed me, and his hardworking spirits moved me. He gave the opportunity to use those equipment in the laboratory. I am also grateful for the work he did for the laser system which could be used in the experiment.

I would like to thank Rui Zhang at KEK, who is my mentor and friend in these years. He was responsible for most of my operational knowledge of lasers. He also contributed to the laser system.

I am also grateful for those who contributed to the project over this years. Otsuki, Okamoto, Moriya, Zhou, Natsui, Shibuya, Satoh, and Takahashi, I thank you all.

I am also very thankful for the support from Ms. Sekiguchi in Uesaka laboratory, Ms. Nabeshima and all the other administrative staffs in the department office.

Last and most importantly, I would like to thank my family who have continually supported and encouraged me. Thank you to my longest, unwavering supporters: my parents and my brother. Thank you to my loving wife, you've always been my biggest supporter, my biggest fan.

Contents

List of Figures

List of Tables

Abbreviations

RF	**R**adio-**F**frequency
LINAC	**LIN**ear **AC**celerator
PhC	**P**hotonic **C**rystal
PBG	**P**hotonic **B**and **G**ap
DLA	**D**ielectric **L**aser **AC**celerator
SWG	**S**ub**W**avelength **G**rating
TE	**T**ransver **E**lectric
TM	**T**ransver **M**magnetic
RCWA	**R**igorous **C**oupled-**W**ave **A**nalysis
SEM	**S**canning **E**lectron **M**icroscope
DNA	**D**eoxyribonucleic **a**cid
CST	**C**omputer **S**imulation **T**echnology
MWS	**M**icro**W**ave **S**tudio
SOL	**S**peed-**O**f-**L**ight
MPB	**M**IT **P**hotonic-**B**ands
MCP	**M**icro- **C**hanel **P**late
DF	**D**efocus-**F**ocus
FD	**F**ocus-**D**efocus

Chapter 1

Introduction

In the past decades, radio-frequency linear accelerators, which is commonly abbreviated as RF linacs, have been essential tools to address many of the challenges in human life. RF linacs can be used, for instance, in huge electron-positron colliders, which serve for discovery across a wide variety of science. Light sources based on RF linacs, either incoherent (synchrotron radiation) or coherent (free-electron laser), enable advances in physics, chemistry, biology, medicine, and material science. Radiotherapy using RF linacs has become an efficient way for cancer treatment. RF linacs can also be used as an alternative for producing radioisotopes currently produced by nuclear reactors, some of which have been or will have to be decommissioned.

In the past decades, physicists have been developing more cost-effective accelerators because of their great potential to make greater contributions to human life. To this end, several advanced accelerator concepts are under development, including plasma-based acceleration and direct laser acceleration. Besides high gradients, these schemes also promise temporal and spectral control at scales well beyond those currently achievable with RF linacs.

In this chapter, RF linac structures are briefly reviewed from a historical perspective. A simple comparison between RF linacs and those advanced acceleration schemes are presented. Particularly, the current status of the direct laser acceleration is shown. In addition, the work in this dissertation is introduced.

1.1 Conventional RF linacs

1.1.1 The wideroe linac

The history of RF linacs starts from 1924 when Gustav Ising proposed the first accelerator of a sequence of metallic hollow-core drift tubes, where the particles could be accelerated in the gaps between them[1]. Wideroe conceived and experimentally demonstrated the first RF linac in 1927. Figure 1.1 depicted the Wideroe linac concept. The drift tubes of length $\beta_e\lambda/2$, with β_e being the ratio of particle's velocity to the speed of light, λ being the RF wavelength, are used to shield the beam during the decelerating half period of the RF. In Wideroe's experiment, an ion beam was accelerated to an energy of 50 keV with an RF voltage of 25 kV at a frequency of 1 MHz. The revolutionary device is the foregoer of all modern RF accelerators[2]. However, the Wideroe scheme is not suitable for the acceleration of high-energy particles. The large particle velocity requires an impractically long drift tube unless the frequency is increased to a gigahertz level. However, at high frequency, the Wideroe linac becomes lossy as a result of the electromagnetic radiation.

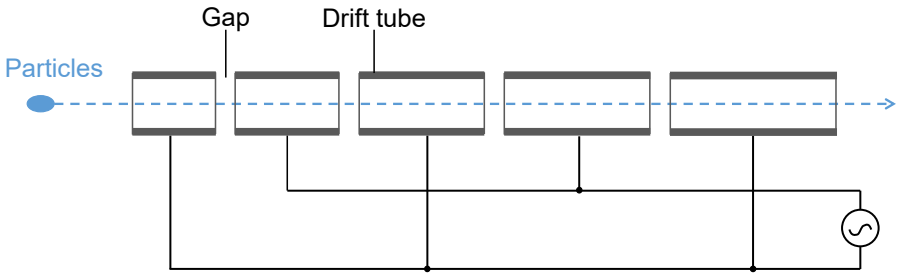

FIGURE 1.1: Schematic of the Wideroe linac.

1.1.2 Modern RF linacs

The high-power microwave sources, e.g., klystrons, developed for radar applications during World War II set the stage for the modern RF linacs which could overcome this problem. Alvarez proposed a linac in 1946[3], by including the Wideroe structure in a cavity where the electromagnetic fields could be confined, and realized a proton linac in 1955[4, 5]. Figure 1.2 illustrates the Alvarez linac concept. Unlike the Wideroe linac, in the Alvarez linac the length of the drift tubes is $\beta_e\lambda$. The high frequency of the microwave results in a reduction of the lengths of drift tubes, making the Alvarez scheme practical. In Alvarez's experiment, a linac length of 12 m at a resonant frequency of 200 MHz accelerated protons from 4 to 32 MeV. The Alvarez linacs are still widely used today to accelerate ions from a few hundred keV to a few hundred MeV. The Alvarez

linac is considered as a standing-wave structure because the accelerating field along the drift tubes oscillates in time, but its peak amplitude profile does not move in space.

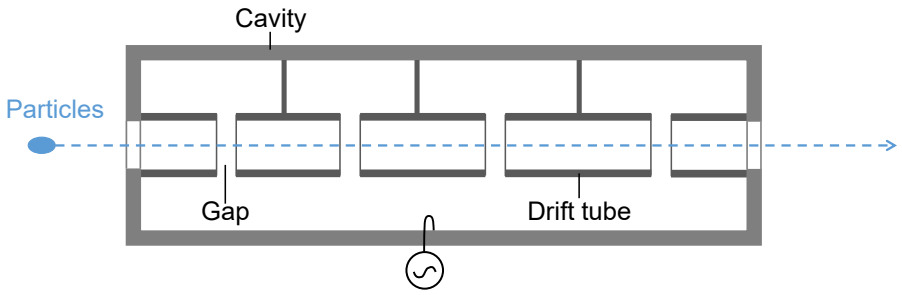

FIGURE 1.2: Schematic of the Alvarez linac.

At about the same time as the Alvarez scheme was demonstrated, Stanford University designed and experimentally tested a structure that is suitable for high-energy electrons. This structure, referred as a disk-loaded waveguide, consisted of an array of electromagnetically coupled cellschodorow1955stanford. In the experiment, with 21 klystrons with an average output power of about 9 MW at a frequency of 2.856 GHz, the maximum energy achieved is 630 MeV. The disk-loaded waveguide is considered as a traveling-wave structure because the accelerating mode propagates synchronously with particles along the waveguide. Compared with the standing-wave structures, traveling-wave structures usually need shorter filling times that is preferable for higher accelerating gradient, because the maximum sustainable RF field decreases with increasing pulse duration.

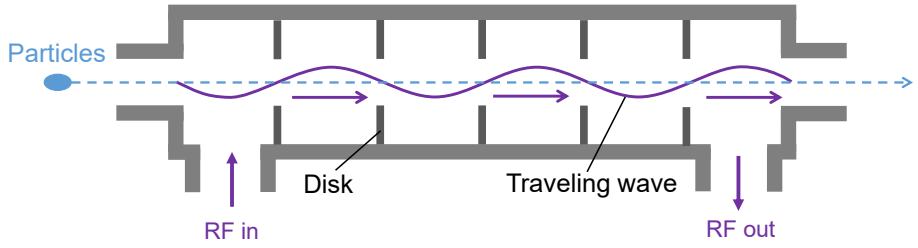

FIGURE 1.3: Schematic of a disk-loaded waveguide.

Since the invention of the first modern proton (Alvarez structure) and electron (disk-loaded waveguide) linacs, many linear accelerator structures have been proposed and constructed. Independent-cavity linacs have been constructed for acceleration of heavy ions and superconducting proton linacs. Coupled-cavity linacs, for instance, have been used for acceleration of electrons and protons in velocity rang $0.4 < \beta_e < 1$. They use multi-cavity accelerating structures formed by coupling an array of cavities, also referred as cells, together. Figure 1.4 illustrates a side-coupled structure in $\pi/2$ mode as an example of a coupled-cavity linac. Some other structures, e.g., independent-cavity linac and radio frequency quadrupole structures, have also been built for different purposes.

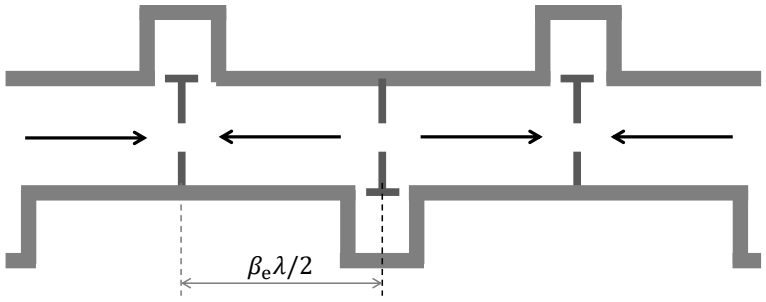

FIGURE 1.4: Schematics of a side-coupled linac structure.

1.1.3 Current status of RF linacs

RF linacs can operate with short pulse (microsecond), long pulse ($> 10\ \mu s$) and continuous wave (CW). For short-pulse applications, cavities made of copper are commonly used. Due to the electrical breakdown at the metal surface in the presence of strong electric fields, short-pulse RF linacs typically operate with accelerating gradients of 10 to 50 MV/m level, leading to a large size and high cost that severely limit their availability. Great efforts have been made to enhance the capability of existing accelerating technologies. Recent X-band accelerator structures have demonstrated accelerating gradient over 100 MV/m[6].

For applications requiring long-pulse or CW accelerating field, copper cavities are limited to gradients near 1 MV/m and become uneconomical because the ohmic power loss over the cavity walls increases as the square of the accelerating voltage[7, 8]. The use of superconducting RF (SRF) cavities made of niobium is a successful approach to solve this problem. The SRF niobium cavity has a surface resistance many orders of magnitude lower than the copper cavity, leading to a much higher quality factor in the $10^9 - 10^{10}$ range and in turn an overall power saving factor of several hundred. Accelerating gradients around 50 MV/m have been achieved with superconducting structures.

1.2 Advanced accelerator concepts

1.2.1 Plasma-based accelerator

Plasma-based accelerators using plasma waves for particle acceleration are attracting more and more attention due to their ability to reduce the size and cost of accelerators. Plasma waves in such kind of accelerators can be driven by high-power laser pulses or energetic particle beams[9, 10], as shown in Fig. 1.5(a) and (b), respectively.

Ionized plasmas can sustain electric fields for acceleration of charged particles in excess of $E_0 = cm_e\omega_p/e$ or $E_0 \simeq 96\sqrt{n_0(\mathrm{cm}^{-3})}$, with $\omega_p = (4\pi n_0 e^2/m_e)^{1/2}$ being the electron

plasma frequency, n_0 being the ambient electron number density, e and m_e being the electron charge and mass, respectively. It shows that, with a typical plasma density $n_0 = 10^{18}$ cm^{-3}, an electric field $E_0 \simeq 96$ GV/m is sustainable. Experiments have demonstrated accelerating gradients > 100 GV/m[11], which is about three orders of magnitude greater than that obtained in conventional RF linacs. Because of the high gradients, plasma-based accelerators can achieve a given electron energy in a shorter distance than RF linacs.

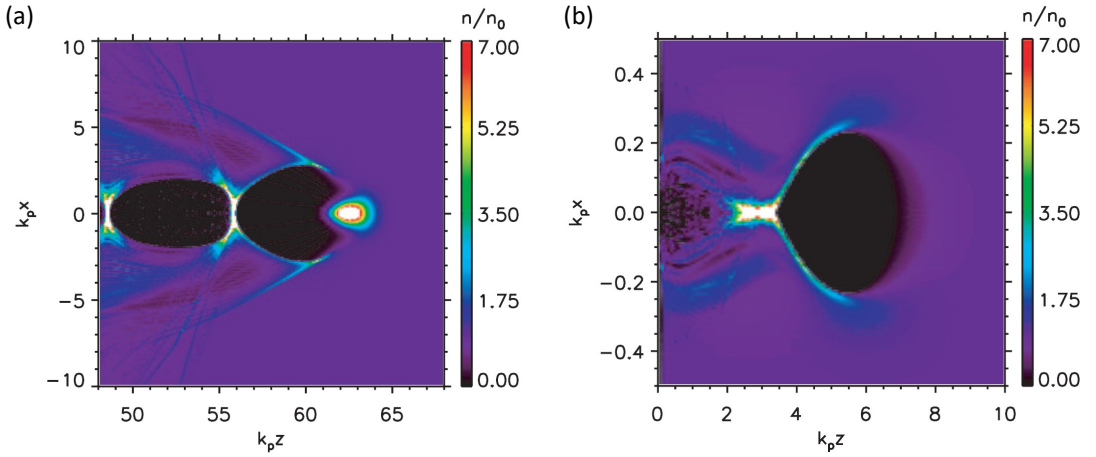

FIGURE 1.5: Examples of an electron density wake driven by an electron beam (a) and a laser pulse (b). (a) The electron beam is moving toward the right with its center located at $k_p z = 62.5$. Plasma density $n_0 = 5 \times 10^{17}$ cm^{-3}, electron energy 0.5 GeV, peak density $n_b = 5n_0$. (b) The laser is movign toward the right with its center located at $k_p z = 7$. Plasma density $n_0 = 1.2 \times 10^{16}$ cm^{-3}, laser length 68 μm, spot size $r_0 = 10$ μm. Taken from [10].

In addition to the high accelerating gradient, plasma-based accelerators can also produce an electron bunch with a short pulse duration, which depends on the plasma wavelength $\lambda_p = 2\pi c/\omega_p$, or $\lambda_p \simeq 3.3 \times 10^{10}/\sqrt{n_0(\text{cm}^{-3})}$. For examples, $n_0 = 10^{18}$ cm^{-3} yields $\lambda_p \simeq 33$ μm, resulting in an electron bunch duration $\tau_p < 100$ ps. An electron bunch length of ~ 1 fs has been demonstrated by using a near-single-cycle laser pulse of 3.4 fs duration[12]. The short electron bunches, for instance, can be used in the next-generation free electron lasers.

The up-to-date plasma-based acceleration experiments aim to generate multi-GeV electron bunches, optimize beam quality and better control plasma waves. A milestone is the demonstration of ~ 100 MeV electron bunch production with energy spreads of a few percent in 2004[13–15]. In 2014, an electron bunch of energy 4.25 GeV has been produced by a laser-driven plasma wakefield accelerator[16]. In 2015, particle-beam-driven plasma wakefield acceleration of initial 20.35-GeV positron bunch to around 25 GeV has also been demonstrated[17]. In 2016, staged acceleration has been realized to overcome the limitation to energy gain by laser depletion[18]. Production of electron bunch with higher energies is expected in the near future.

Although plasma-based accelerators have made great progress in the past two decades and are the most mature advanced acceleration scheme, so far, RF linacs still have superior performance for most accelerating beam properties than plasma-based accelerators, e.g., the beam quality and stability. Laser-driven wakefield plasma accelerators driven by large and expensive petawatt lasers can only operate with a low repetition rate.

1.2.2 Dielectric laser accelerator

Another advanced acceleration concept, referred as dielectric laser accelerator (DLA), are garnering increasing interest in recent years since their potential to miniaturize the accelerators[19]. Unlike the plasma-based accelerators, DLAs accelerate particles in the vacuum with laser-induced near fields. Due to the high power loss and low breakdown threshold of metallic materials at optical frequencies, as well as the difficulty in the fabrication of nano-scale metallic structures, it is more practical to use dielectrics in optical acceleration. The measurement of damage thresholds for dielectric materials (for example in Fig. 1.6), indicates that these materials can sustain a field at the GeV/m level in the optical to near-infrared regime. By leveraging the high damage thresholds of dielectrics, DLA can achieve accelerating gradients of one to two orders of magnitude higher than the typical gradients in RF linacs. The rapid progress in industrial fabrication capabilities and commercially available high-power lasers in recent years leads to the demonstration of dielectric laser acceleration in 2013[20, 21].

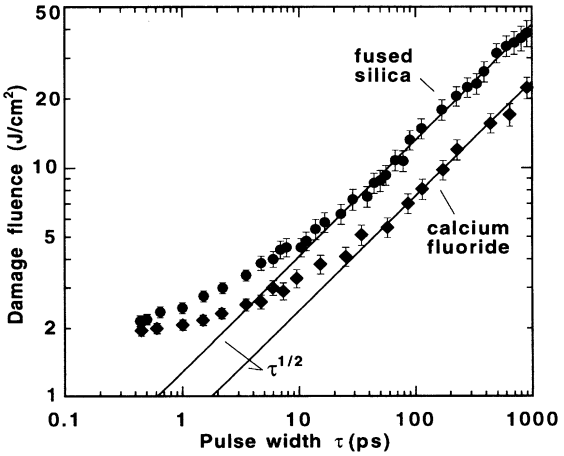

FIGURE 1.6: Damage threshold of a sused silica and CaF_2. Solid lines are $\tau^{1/2}$ fits to long pulse results. Taken from [22].

Although DLAs are still in an early stage of development, they have obvious characteristics. Their principal advantage over the RF linacs is the GV/m-level gradients, which lead to a reduction in the size of accelerators. Compared with plasma-based acceleration, DLA has a lower accelerating gradient, but has the advantage of supporting a better

beam quality. A significant challenge for DLAs in a number of applications is the low bunch charge at the fC level, as a result of the operation in the near fields. However, DLAs driven by moderate-power lasers can operate at a GHz-level repetition rate, which is much higher than that of the plasma-based accelerator and can compensate for the problem.

To accelerate electrons in a DLA, an accelerating mode with a longitudinal electric component and a phase velocity equals the speed of electron must be provided. Structures proposed to this end can roughly fall into three categories, i.e., diffraction gratings, waveguides, and total-reflection structures.

1.2.2.1 Diffraction gratings

Takeda and Matsui proposed a laser linac with a grating in 1968, using the near field of a single grating to accelerate electrons[23]. The mechanism is known as inverse Smith-Purcell effect, which was demonstrated in the 1980's with kV/m-level gradients by using THz radiation and metallic gratings[24]. About twenty years later, the well-developed industrial fabrication capability led to the demonstration of high-gradient acceleration with dielectric grating structures.

A fused-silica single grating was used in the first demonstration of dielectric laser acceleration of subrelativistic electrons in 2013[20]. The structure used in the experiment is shown in Fig. 1.7(a). Upon the incidence of a laser on the grating, the diffraction effect generated an evanescent mode that travels synchronously with and efficiently accelerates electrons. In the experiment, 28 keV electrons were accelerated by the 3rd diffraction order with a maximum accelerating gradient of 25 MV/m. In 2015, the 4th and 5th diffraction orders of the grating were utilized to accelerate electrons with energies of 15.2 and 9.6 keV, leading to the possibility of a novel compact electron source[25]. In 2015, a silicon single grating was fabricated, as shown by Fig. 1.7(b), and demonstrated accelerating gradients in excess of 200 MeV/m for 96.3 keV electrons[26]. In 2016, a gradient of 210 MV/m was measured using a single silicon grating to accelerate 30.7 keV electrons with a 20 fs laser pulse[27]. Besides, single gratings were also used in the demonstration of multi-stage acceleration, chirped-geometry acceleration to overcome the dephasing limit, and transverse focusing[28]. However, the evanescent accelerating fields provided by the single gratings distort the electron beam and result in large energy spread. In addition, they cannot generate an accelerating mode for speed-of-light electrons.

Plettner and coworkers conceived the laser-driven double-grating accelerating structure in 2006. By using such a double-grating structure, in 2013, efficient dielectric laser acceleration of relativistic electrons was demonstrated. The structure used in experiment

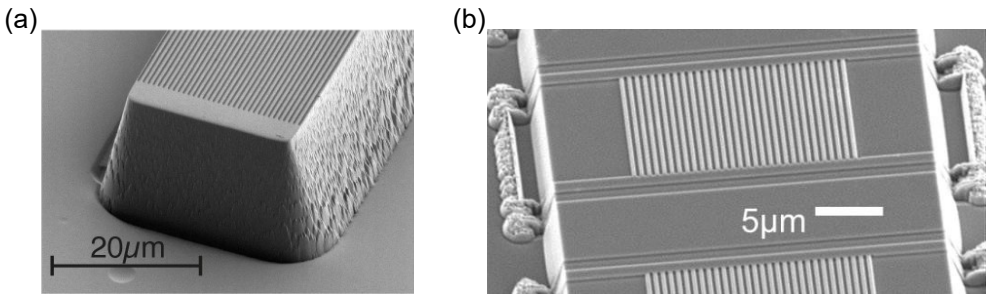

FIGURE 1.7: Fused-silica and silicon single-grating structures for subrelativistic electron acceleration. (a) Fused-silica single grating used for 28 keV electron acceleration, taken from [20]. (b) Silicon single grating used for 96.3 keV electron acceleration, taken from [26].

is shown in Fig. 1.8. In the experiment, 60 MeV electrons are energy modulated with a gradient beyond 250 MV/m, driven by a 800 nm, 1.24 ± 0.12 ps, Ti:sapphire laser. In 2016, by employing femtosecond-duration laser pulses, an accelerating gradient around 690 MV/m was measured.

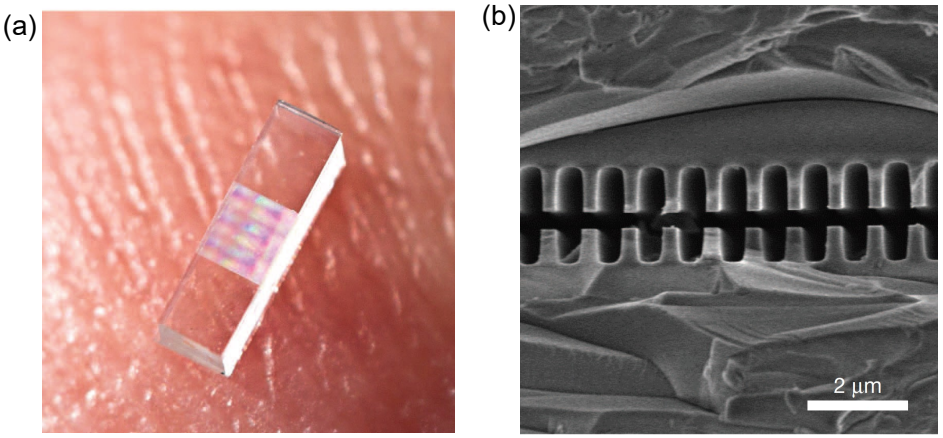

FIGURE 1.8: Fused-silica double-grating structure for relativistic electron acceleration. (a) Picture of a double-grating structure on a fingertip. (b) Scanning electron microscope image of the cross-section of a double-grating structure. Taken from [21].

Double-grating structures were also used for subrelativistic electron acceleration. In 2015, by using a silicon double-grating structure, also called dual-pillar structure as shown in Fig. 1.9(a), sub-100 keV electrons were accelerated with an accelerating gradient of 370 MV/m, driven by a Ti:sapphire laser. In 2018, phase-dependent laser acceleration and deflection of electrons with a symmetric silicon dual-pillar structure as shown in Fig. 1.9(b) were demonstrated, with an accelerating gradient of 200 MV/m, driven by 40 nJ, 300 fs, 1940 nm laser pulses.

Due to the easy coupling with a surface-normal laser, the capability to eliminate the pulse-slippage problem, and the compatibility for on-chip integration, research with diffraction structures points towards a promising future.

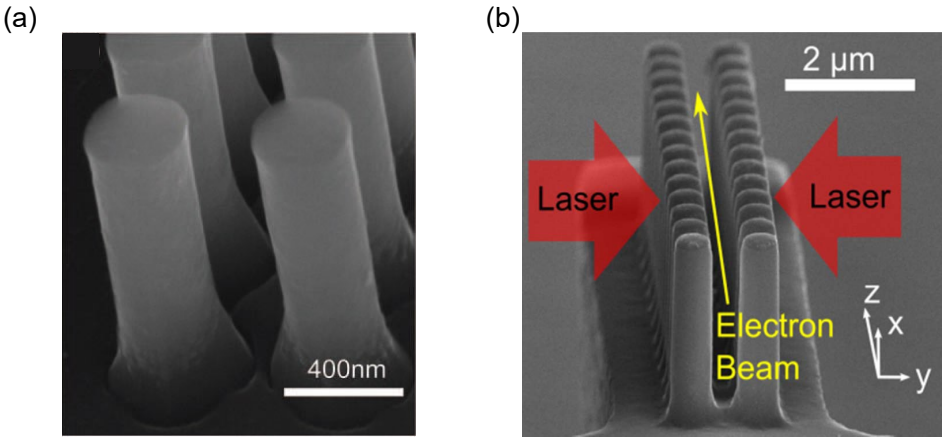

FIGURE 1.9: Scanning electron microscope images of the silicon double-grating structures for subrelativistic electron acceleration. (a) A double grating with a single-sided illumination, taken from [29]. (b) A double grating with dual-sided illumination, taken from [30].

1.2.2.2 Waveguide structures

Hollow-core waveguides have emerged as a promising candidate for a future DLA in the past two decades. They are considered as traveling-wave structures. Optical acceleration in the core requires a waveguide that is constructed out of dielectric materials and can confine the accelerating mode propagating along its core. Photonic crystals (PhCs), which are regular arrays or lattices of dielectric elements, are widely used to confine the accelerating wave to the core due to the photonic band gap (PBG) arising from constructive interference of distributed reflections from each periodic layer. Waveguide structures based on 1D, 2D, and 3D variations in dielectric constant have been proposed, some of which are shown in Fig. 1.10. However, so far, because of the difficulties in power coupling to the confined accelerating mode and the challenging fabrication, no successful experimental demonstration with waveguides has been reported.

1.2.2.3 Total-reflection structures

Total-reflection structures utilize the evanescent fields generated on the planar dielectric surface by total internal reflection for particle acceleration. Their accelerating fields represent properties similar to the grating structures. This approach requires simpler fabrication and can sustain high accelerating gradient due to the lack of field enhancement. In 2017, the acceleration of subrelativistic 28.4 keV electrons was experimentally demonstrated, with an accelerating gradient around 19 MV/m[36]. The experimental setup is shown in Fig. 1.11(a). This effect was also verified by directly measuring the longitudinally-polarized electric fields at the surface of a dielectric material driven by a terahertz source[37]. The interaction length can be extended with a waveguide structure, or a ring resonators as shown in Fig. 1.11(b)[38].

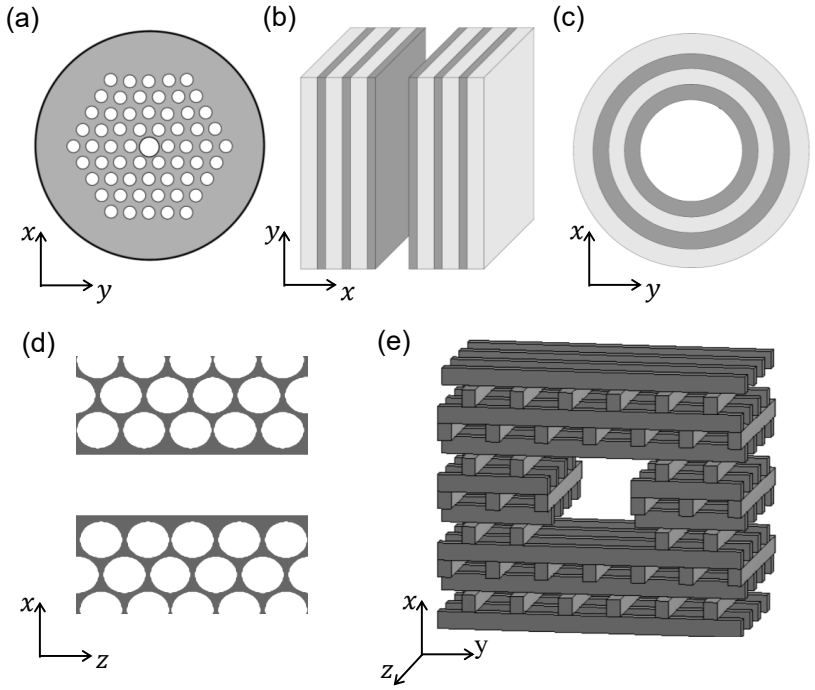

FIGURE 1.10: Examples of photonic-crystal accelerating waveguides. (a) transverse PBG structure, taken from [31]. (b) Planar Bragg structure, taken from [32, 33]. (c) Cylindrical Bragg structure, taken from [32, 33]. (d) Longitudinal PBG, taken from [34]. (e) Woodpile structure, taken from [31]. A double grating with dual-sided illumination, taken from [35]. Electrons travel in the z direction.

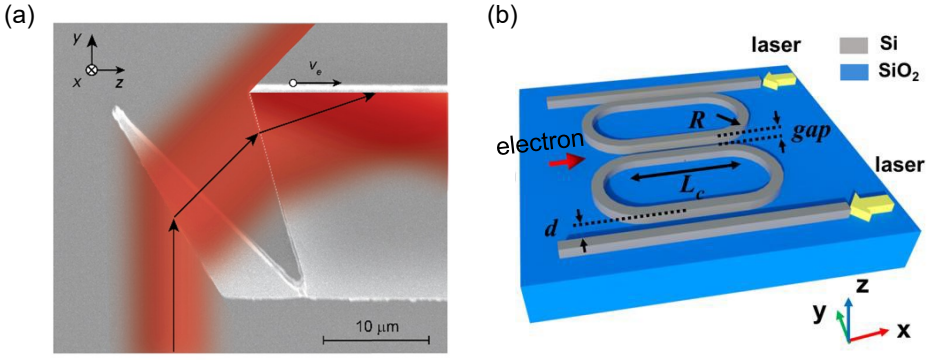

FIGURE 1.11: Microstructures for the production of evanescent accelerating fields with total reflection. (a) Scanning electron microscope image of the silicon structure for the excitation of an evanescent field using two subsequent refractions of the laser beam. Laser ray path indicated by the red overlay and the black arrows. Taken from [36]. (b) Schematic of a racetrack ring resonator accelerator. Taken from [38].

1.3 DLA for radiobiology research

DLAs could be used for a wide variety of applications. A single-stage DLA structure could be used for attosecond-bunch steering for ultrafast electron diffraction and microscopy[39]. Multi-stage DLA structures could be used for radiobiology research, radiotherapy, light sources, and colliders[19]. Here, we briefly introduce the application of DLAs for radiobiology research.

1.3.1 Radiobiology research with microbeams

The damage effect of low radiation doses ($\leq$ 50 mSv) on a living cell is important for a variety of issues, e.g., the cancer radiation treatment, nuclear accident, and radiobiological terrorism. One approach to evaluating the effect is to study the damage and repair processes of DNA. To this end, well-defined microbeams of ions, x-rays, lasers, and electrons have been widely used to irradiate a living cell for radiobiology research[40]. To clarify how radiobiology research can be conducted with microbeams, we introduce, for instance, an experiment for studying the function of WRN protein in the repairing process of a living cell with laser irradiation[41].

Figure 1.12(a) illustrates a UV micro-laser irradiation system for the experiment. It consisted of two laser sources and a confocal microscope. The left column shows a 365 nm laser source whose output pulse energy could be controlled by passing the laser through either an F20 or an F25 filter. Before irradiating the cells, the laser pulses were focused by a $\times$40 objective lens to obtain a spot size of 1 μm[42]. We will show how the 365 nm laser microbeam was used in the experiment.

First, irradiating the cells with different laser dose revealed the relationship between the types of DNA damage with the irradiation dose, as shown in Figure 1.12(b). In the experiment, single-strand DNA breaks and double-strand DNA breaks were detected by antibody against poly-ADP-ribose and γH2AX, respectively, and base damage was detected by accumulated GFP-OGG1 for 8-oxoGuanine. It is shown that using a laser pulse energy of 0.75 μJ led to single-strand DLA breaks while using a laser pulse energy of 2.5 μJ led to double-strand breaks and base damage in addition to the single-strand DLA breaks.

To analyze the accumulation of WRN in response to DNA damage, GFP-tagged WRN was used. Irradiating the cells with high-dose irradiation, revealed a time-dependent accumulation of WRN at the radiation cite, as shown in Fig. 1.12(c). About three minutes after the irradiation, the accumulation of WRN reached its maximum.

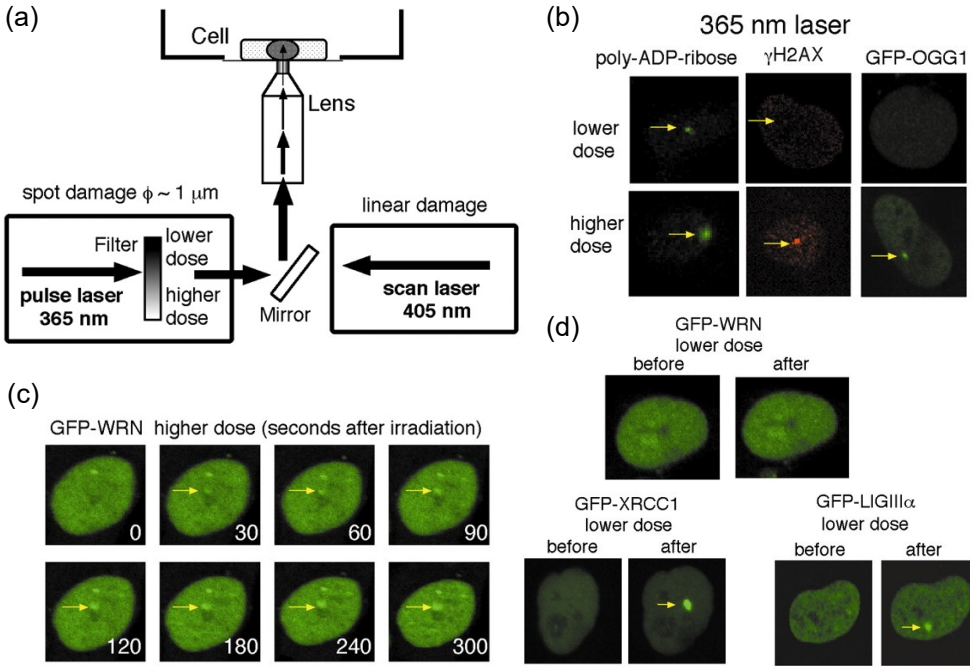

FIGURE 1.12: Laser microbeam irradiation systems and experiment results. (a) Laser microbeam irradiation system. The laser pulse energy was regulated by the filter. The laser spot size was compressed by a ×40 objective lens before irradiating the cells. (b) Three types of damage induced by low dose or high dose of 365 nm laser irradiation in HeLa cells. The HeLa cells were stained with anti-poly (ADP) ribose for single-strand breaks, or γH2AX antibody for double-strand breaks, or accumulation of GFP-tagged OGG1 at irradiated sites for base damage. (c) The dependence of accumulation of GFP-tagged WRN after higher dose irradiation with the 365 nm laser on time in HeLa cells. (d) Accumulation of GFP-tagged WRN, GFP-tagged XRCC1, and LIGIIIα after lower dose irradiation with the 365 nm laser in HeLa cells. Taken from [41].

To find the substrate for the accumulation of WRN, the cells were also irradiated with low-dose laser pulses, which induce only single-strand breaks. As shown in Fig. 1.12(d), after irradiation, XRCC1, and LIGIIIα, which were involved in the repair of single-strand breaks, efficiently accumulated, while WRN did not accumulate at all, indicating that the substrate for the accumulation of WRN was not single-strand breaks.

1.3.2 DLA-based electron source

The microbeams of ions, X-rays, electrons are essential tools to study the influence of ionization radiation on a living cell. Facilities have been built to produce those microbeams. For examples, cyclotrons were built to deliver MeV-class ion beams, and synchrotrons were built to generate X-rays with energies up to a few tens of keV. However, their availability is greatly limited because of their large size and high cost.

DLA is very suitable for radiobiology research due to its small size, low price and the capacity of delivering nanometer-sized beams with attosecond pulse durations[43]. Figure 1.13 shows a schematic of such an electron source based on DLA. Diffraction gratings, which have been experimentally demonstrated high accelerating gradient, can be used as accelerating structures. A photocathode using a thin gold film that has a diameter less than 100 nm as emitter can generate an electron beam that can be collimated to a size of less than 100 nm[44, 45]. Electrons generated by an emitter are accelerated between the anodes and then accelerated by a multi-stage DLA driven by a fiber laser. The phase of each laser pulse should be tuned for multi-stage acceleration.

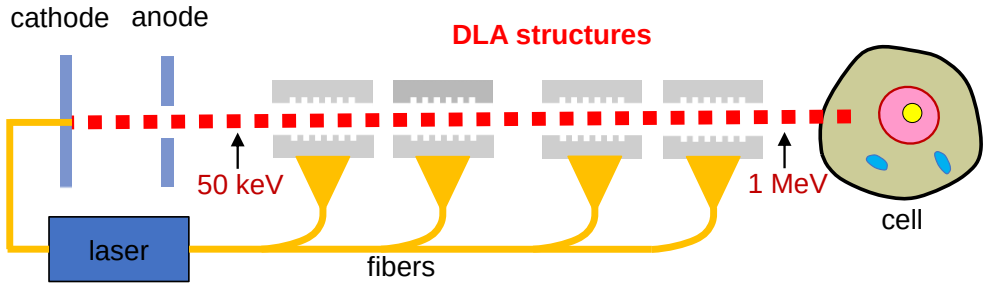

FIGURE 1.13: A conceptual drawing of a DLA-based electron source for radiobiology research.

The output electron parameters of the electron source are determined by the process of the energy absorption and electron beam blur via multiple Coulomb scattering in a cell. In order to locate the interaction area prior to the irradiation for a typical human cell with a size of 10 μm, an electron blur of 1 μm or less, which is nearly the resolution of an optical microscope, must be provided, requiring an electron beam with a radius < 0.5 μm and angular distribution < 0.05 rad[43]. Consequently, the electron energy must be at least 0.5 MeV to restrict the expansion of the electron beam. Considering the radiation safety regulations, we choose to use 1 MeV electrons. Energy loss in a Si_3N_4 vacuum window with a thickness of 100 nm is 50 eV at 1 MeV, which can be neglected. Since the collision stopping power of protons in water are ~ 160 times that of electrons, to generate the same energy deposition in the cell by electrons with that by a 1 MeV proton, one bunch should have ~ 160 electrons. The absorption dose D of these electrons can be measured by $D = \mathrm{d}E/\mathrm{d}m$, where $\mathrm{d}E$ is deposited energy and $\mathrm{d}m$ is the areal mass element. Energy deposition in the tissue is 180 eV/μm at 1 MeV. Since the cell thickness is 10 μm, the energy deposition will be 1800 eV/electron. For an electron beam with a size around 1 μm, we can roughly consider an irradiation volume of 10 $\mu\mathrm{m}^{-3}$, corresponding to $\sim 10^{-14}$ kg. Then the absorption dose can be evaluated to be 4.7 Gy/bunch. Operation in a high repetition rate can drastically increase the absorption dose, depending on the number of electron bunches. Important parameters of the electron source are summarized in Table 1.1.

TABLE 1.1: Electron source parameters required for radiobiology research.

Electron source parameters	
Electron energy (MeV)	1
Beam size (μm)	~ 0.5
Bunch length (attosec)	50
Bunch charge (fC)	0.026
Absorption dose (Gy/bunch)	4.7

Based on the above requirement, K.Koyama and coworkers have performed a parameter study for a DLA-based electron source using SiO_2 double grating with dual-sided illumination[43]. The 1030 nm laser pulse was assumed to have a flat-top pulse shape and intensity profile for simplicity, with a peak incident field of 2 GV/m. The double grating is shown in Fig. 1.14(a). The field distribution in the structure at the initial stage and steady stage are shown by Fig. 1.14(b) and Fig. 1.14(c), respectively. With a grating period of 1030 nm, the optimum pillar height and pillar width were calculated to be $H_{\rm p}/\lambda \approx 1$ and $L_{\rm p}/L_{\rm G} \approx 0.5$, respectively. To accelerate electrons from a few tens

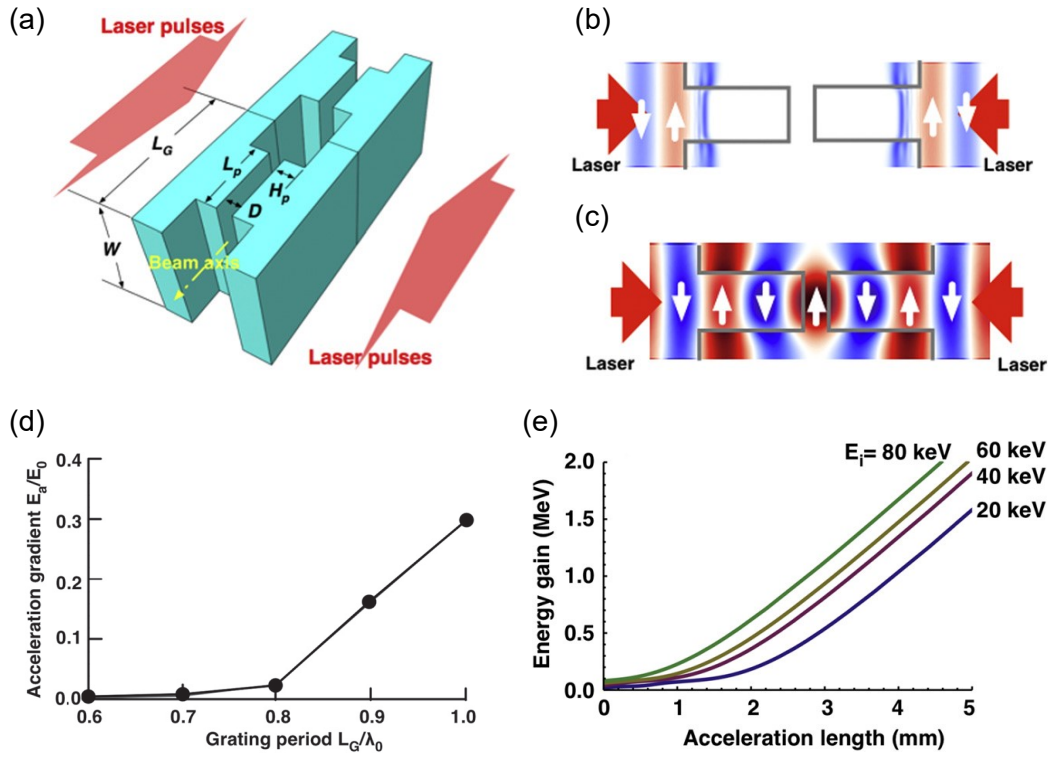

FIGURE 1.14: Parameter study of DLA electron source for radiobiology research. (a) Schematic of a double grating. (b) The wavefront in the structure at the initial stage. (c) The wavefront in the structure at the steady stage. (d)The accelerating gradient versus the grating pillar height $H_{\rm p}/\lambda$ and pillar width $L_{\rm p}/L_{\rm G}$, with $L_{\rm G}$ being the grating period. (e) The accelerating gradient versus the electron energy. Taken from [43].

of keV to 1 MeV, the grating period was changed to match the synchronicity condition for different electron energies. Figure 1.14(d) shows the resulting accelerating gradient as a function of grating period. The accelerating gradient drastically decreased when the grating period was reduced. The accelerating gradients were 20 MV/m for 20 keV electrons and 600 MV/m for relativistic electrons. Figure 1.14(e) shows the energy evolution of the electrons along the longitudinal direction at various initial electron energies. To accelerate electrons to an energy of 1 MeV, the interaction lengths were 4 mm and 3 mm for 20 keV electrons and 80 keV electrons, respectively.

To make a compact and reliable system, a fiber laser was used to pump the dielectric accelerator, as shown in Fig. 1.15. The width of the irradiation area was assume to be 5 μm. If only one pair of laser pulses were used to illuminate the entire structure, the required peak power and pulse energy were 200 MW and 10 mJ. By using N sequential laser pulses, the laser peak power and energy were reduced to $1/N$ and $1/N^2$, respectively. Table 1.2 shows the laser and accelerator parameters using 10 pairs of laser pulses.

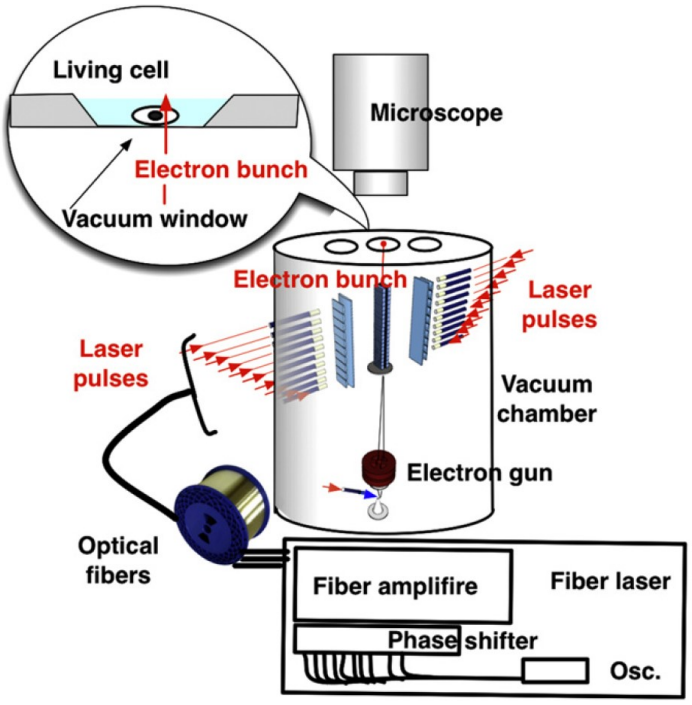

FIGURE 1.15: A conceptual drawing of the DLA-based electron source for radiobiology research. A fiber laser was used to drive the DLA, with the phase of each pulse properly tuned. Taken from [43].

TABLE 1.2: Parameters of a DLA-based electron source for radiobiology research.

Accelerator parameters	
Initial electron energy (keV)	20
Final electron energy (MeV)	1
Acceleration length (mm)	4
Acceleration time (ps)	50
Laser parameters	
Irradiation area (cm^2)	4×10^{-4}
Number of pulse pairs	10
Pulse duration (ps)	5
Peak power of each pulse (MW)	20
Pulse energy (μJ)	50
Total laser energy (mJ)	1

1.4 About the thesis

To realize a practical electron source for radiobiology research, a few technical challenges must be resolved, including (but not limited to): first, an emitter that can produce an electron beam with a transverse size $<$ 100 nm must be developed; second, a DLA structure that can produce a uniform accelerating mode must be provided; third, to accelerate electrons to the target energy, a multi-stage accelerator structures as well as focusing components should be integrated on a chip with a laser power delivery system to extend the interaction length to millimeter scale.

In this work, we focus on the development of DLA structures that can facilitate the realization of an electron source. It has been suggested that a double-grating structure could support phase-dependent acceleration and deflection by controlling the relative phase of the drive lasers illuminating each side[30]. In contrast, we proposed a resonant double-grating structure with a single-sided illumination by merging diffraction gratings with resonating Fabry-Perot cavities. In this way, a laser-power efficient way of electron acceleration may be enabled, and the complexity of an on-chip DLA system could be reduced. Moreover, we designed a planar waveguide structure with highly-reflective gratings as mirrors. Compared with the waveguides with PhCs, this structure needs only one layer of periodic structures to confine the mode, which may simplify the fabrication and enable easier integration. Additionally, we also designed a test station for diffraction gratings, all the components have been fabricated.

The thesis is organized as follows:

In Chapter 2 we present the physics of single-grating DLA structures. We also show the simulation results of particle acceleration at a single grating structure.

In Chapter 3 we show our design of a resonant double-grating structure with a single-sided illumination. We further discuss the performance of such a structure with the simulation results of particle acceleration.

In Chapter 4 we propose a planar waveguide with subwavelength gratings as reflectors. We further discuss the accelerator parameters with several examples of such waveguides.

In Chapter 5 we introduce the progress of developing a test station for DLA structures.

In Chapter 6 we conclude and briefly discuss the future work.

Chapter 2

Single grating structures

In this chapter, we consider a single grating structure for particle acceleration. We discuss the physics behind particle acceleration with a single-grating structure. We further numerically investigated the dependence of accelerator performance on the grating dimensions with CST Microwave Studio (MWS). In addition, we perform particle tracking of subrelativistic electrons which interact with the accelerating mode.

2.1 Accelerating mode of a single grating

A grating is a periodic structure widely used in optics, as shown in Fig. 2.1. Based on diffraction effect, it can split one light into several beams at different angles. Therefore, grating structures have been important components for monochromators and spectrometers. The major concern in these applications is the diffracted beams that can propagate.

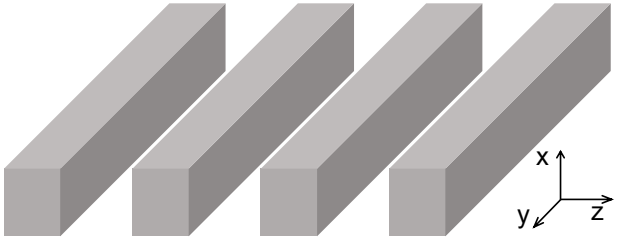

FIGURE 2.1: Schematic of a generic single grating structure.

In contrast, to accelerate electrons in the vacuum, we focus on a diffraction order, or a spatial harmonic, that is evanescent. For acceleration purpose, an accelerating mode with a longitudinal electric field and a phase velocity that matches the electron speed should be provided. In the following, we will show that an evanescent mode generated

by diffraction at a single grating can be used for dielectric laser acceleration by designing the grating period.

In an isotropic and source-free media, the Maxwell's equations of electrodynamics is given by

$$\begin{aligned} \nabla \cdot \widehat{\mathbf{D}} = 0, \qquad & \nabla \times \widehat{\mathbf{E}} = -\frac{\partial \widehat{\mathbf{B}}}{\partial t}, \\ \nabla \cdot \widehat{\mathbf{B}} = 0, \qquad & \nabla \times \widehat{\mathbf{H}} = \frac{\partial \widehat{\mathbf{D}}}{\partial t}, \end{aligned} \tag{2.1}$$

where $\widehat{\mathbf{D}}$, $\widehat{\mathbf{E}}$, $\widehat{\mathbf{B}}$, $\widehat{\mathbf{H}}$ represent the vectors of the displacement field, electric field, induction field and magnetic field, respectively.

For time-harmonic case, with ω being the angular frequency, any instantaneous field $\widehat{\mathbf{A}}(x, y, z, t)$ can be described in terms of a vector $\mathbf{A}(x, y, z)$ that depends on the space coordinates,

$$\widehat{\mathbf{A}}(x, y, z, t) = \mathbf{A}(x, y, z)\mathrm{e}^{-\mathrm{i}\omega t}. \tag{2.2}$$

For a grating as shown in Fig. 2.2, the magnetic permeability μ is considered homogeneous, $\mu = \mu_0$, where μ_0 is the magnetic permeability in vacuum, while the electric permittivity ε is considered space dependent, $\varepsilon = \varepsilon_0\varepsilon_r$, with ε_0 being the permittivity in vacuum and ε_r being the relative permittivity. Taking the curl of the last two equations in Eq. 2.1 yields

$$\nabla^2\mathbf{E} = -\omega^2\varepsilon\mu\mathbf{E} - \nabla\left(\mathbf{E} \cdot \frac{\nabla\varepsilon}{\varepsilon}\right), \tag{2.3}$$

$$\nabla^2\mathbf{H} = -\omega^2\varepsilon\mu\mathbf{H} + \mathrm{i}\omega\nabla\varepsilon \times \mathbf{E}. \tag{2.4}$$

In the case of a perfect dielectric that has no conductivity at all, the conductivity $\sigma = 0$ and the permittivity $\varepsilon = \varepsilon_0\varepsilon_r$ is real. In the case of a lossy media that has a non-negligible conductivity σ, the permittivity $\varepsilon = \varepsilon_0\varepsilon_r = \varepsilon' + \mathrm{i}\varepsilon''$ becomes complex, with the imaginary part $\varepsilon'' = \sigma/\omega$. In the rest of this text, we assume for simplicity that the dielectric materials in region I and II are lossless, i.e., $\sigma_\mathrm{I} = \sigma_\mathrm{II} = 0$.

The grating is assumed to be infinite in the y direction, i.e., the space-dependent vector $\mathbf{A} \equiv \mathbf{A}(x, z)$. Due to the one-dimensional nature, the grating structure can be treated as a stack of layers in which the permittivity depends only on the position z, i.e., the permittivity $\varepsilon \equiv \varepsilon(z)$.

For TM or TE polarization, the electric field of the incident light is perpendicular to or along the grating bars, respectively. The general case can be treated as the combination

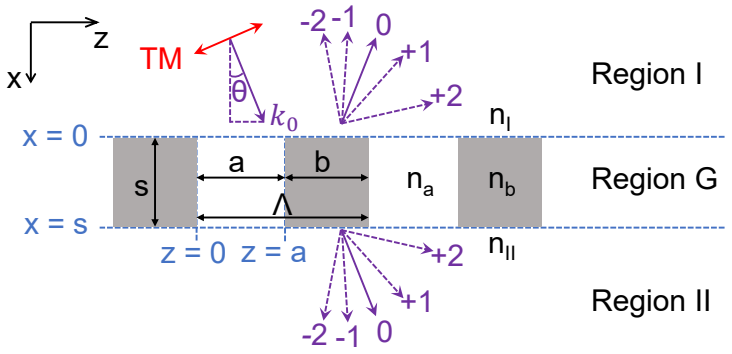

FIGURE 2.2: Cross section of a single grating and the wave vectors outside the grating. It consists of a periodic array of silicon bars with refractive index n_b, surrounded by materials with a refractive index n_I in the reflection region and n_II in the transmission region. The grating is assumed to be infinite in the y direction and infinitely periodic in the z direction. A TM wave is incident from above, with the electric field (red arrow) in the incidence plane. Λ, grating period; s, bar length; b, bar width, θ, incident angle. Electrons travel along the longitudinal (z) direction in the channel. Outside the grating, there are a number of diffraction orders.

of TE and TM polarization. Here, our discussion is limited to TM polarization which is required for particle acceleration. Fig. 2.2 shows the cross-section of the single grating structure.

In the case of TM polarization, $\mathbf{H} = [0, H_y, 0]$. The gradient of a vector $\mathbf{H}$ can be calculated by $\nabla\mathbf{H} = \left[\frac{\partial}{\partial x}, \frac{\partial}{\partial y}, \frac{\partial}{\partial z}\right]^\mathrm{T} [H_x, H_y, H_z]$. Therefore, Eq. 2.4 can be rewritten as

$$\nabla^2 H_y = \frac{1}{\varepsilon_r(z)} \frac{\mathrm{d}\varepsilon_r(z)}{\mathrm{d}z} \frac{\partial H_y}{\partial z} - k_0^2(z) H_y, \tag{2.5}$$

or, in the form

$$\frac{\partial^2 H_y}{\partial x^2} = -\varepsilon_r(z) \left\{ \frac{\partial}{\partial z} \left[\frac{1}{\varepsilon_r(z)} \frac{\partial H_y}{\partial z} \right] + k_0^2 H_y \right\}. \tag{2.6}$$

From Eq. 2.1, the relation between the field components can be derived

$$[E_x, 0, E_z] = \frac{1}{\mathrm{i}\omega\varepsilon} \left[\frac{\partial H_y}{\partial z}, 0, -\frac{\partial H_y}{\partial x} \right]. \tag{2.7}$$

The incident field can be described by its magnetic y component

$$H_y^\mathrm{inc} = H_0 \mathrm{e}^{\mathrm{i}n_\mathrm{I} k_0 (x\cos\theta + z\sin\theta)}. \tag{2.8}$$

where n_I is the refractive index in region I.

The grating structure is periodic in the z direction with a period of Λ. The linear transformation of the incident field E_y^inc into the total field E_y suggest that, in any region,

$$H_y(x, z+\Lambda) = \mathrm{e}^{\mathrm{i}n_\mathrm{I} k_0 \Lambda \sin\theta} H_y(x, z), \tag{2.9}$$

so the function $F(x,z) = \mathrm{e}^{-\mathrm{i}k_{\mathrm{I}}z\sin\theta}H_y(x,z)$ is periodic in z direction with a period of Λ. The Fourier expansion of $F(x,z)$ yields

$$F(x,z) = \sum_{n=-\infty}^{+\infty} f_n(x)\mathrm{e}^{\mathrm{i}n\frac{2\pi}{\Lambda}z}. \tag{2.10}$$

Therefore, the field $H_y(x,z)$ can be given by

$$H_y(x,z) = \sum_{n=-\infty}^{+\infty} f_n(x)\mathrm{e}^{\mathrm{i}k_{z,n}z}, \tag{2.11}$$

where

$$k_{z,n} = k_{\mathrm{I}}\sin\theta + n\frac{2\pi}{\Lambda} = k_0\left(n_{\mathrm{I}}\sin\theta + n\frac{\lambda}{\Lambda}\right), \tag{2.12}$$

with $n = 0, \pm1, \pm2, \ldots$ being the diffraction order, $k_{z,n}$ being the z wavenumber, k_0 and $k_{\mathrm{I}} = n_{\mathrm{I}}k_0$ being the wavenumbers corresponding to the free space and material in region I, respectively. Eq. 2.12 is known as the diffraction law. The x-dependent coefficients $f_n(x)$ remain to be determined.

In region I, the constant electric permittivity ε_{I} indicates that Eq. 2.5 takes the form of the Helmholtz equation

$$\nabla^2 H_y^{\mathrm{I}} = -\varepsilon_{\mathrm{I}}k_0^2 H_y^{\mathrm{I}}. \tag{2.13}$$

Substituting for H_y^{I} the Fourier expansion (Eq. 2.11) yields

$$\left(\frac{\mathrm{d}^2}{\mathrm{d}x^2} + k_{\mathrm{I},x,n}^2\right) f_n^{\mathrm{I}}(x) = 0, \tag{2.14}$$

where $k_{\mathrm{I},x,n} = (k_{\mathrm{I}}^2 - k_{z,n}^2)^{1/2}$ is the x-wavenumber of the nth diffraction order in the region I. Since the dielectric materials in the region I is lossless, the x-wavenumber $k_{\mathrm{I},n}$ is real when $k_{\mathrm{I}} \geq k_{z,n}$, and imaginary when $k_{\mathrm{I}} < k_{z,n}$; in the latter case, we assume that the imaginary part is positive. Therefore, the general solution of Eq. 2.14 is given by

$$f_n^{\mathrm{I}}(x) = A_n\mathrm{e}^{\mathrm{i}k_{\mathrm{I},x,n}x} + B_n\mathrm{e}^{-\mathrm{i}k_{\mathrm{I},x,n}x}, \tag{2.15}$$

where A_n and B_n are the coefficients of the forward $(+x)$ and backward $(-x)$ propagating components, respectively.

With a single incident plane wave from $x = -\infty$, the total fields in region I can be expressed as the sum of the incident field and the reflected diffraction modes:

$$H_y^{\mathrm{I}} = H_0 \mathrm{e}^{\mathrm{i}k_{\mathrm{I}}(x\cos\theta + z\sin\theta)} + \sum_{n=-\infty}^{\infty} r_n H_0 \mathrm{e}^{\mathrm{i}\left(-k_{\mathrm{I},x,n}x + k_{z,n}z\right)}, \tag{2.16}$$

$$E_z^{\mathrm{I}} = -\frac{\cos\theta}{n_{\mathrm{I}}}\sqrt{\frac{\mu_0}{\varepsilon_0}} H_0 \mathrm{e}^{\mathrm{i}k_{\mathrm{I}}(x\cos\theta + z\sin\theta)} + \sum_{n=-\infty}^{\infty} \frac{k_{\mathrm{I},x,n} r_n}{k_0 \varepsilon_{\mathrm{I},r}} \sqrt{\frac{\mu_0}{\varepsilon_0}} H_0 \mathrm{e}^{\mathrm{i}\left(-k_{\mathrm{I},x,n}x + k_{z,n}z\right)}, \tag{2.17}$$

$$E_x^{\mathrm{I}} = \frac{\sin\theta}{n_{\mathrm{I}}}\sqrt{\frac{\mu_0}{\varepsilon_0}} H_0 \mathrm{e}^{\mathrm{i}k_{\mathrm{I}}(x\cos\theta + z\sin\theta)} + \sum_{n=-\infty}^{\infty} \frac{k_{z,n} r_n}{k_0 \varepsilon_{\mathrm{I},r}} \sqrt{\frac{\mu_0}{\varepsilon_0}} H_0 \mathrm{e}^{\mathrm{i}\left(-k_{\mathrm{I},x,n}x + k_{z,n}z\right)}, \tag{2.18}$$

where $k_{\mathrm{I}}\cos\theta = k_{\mathrm{I},x,0}$ is the x wavenumber of the incident field , $k_{\mathrm{I}}\sin\theta = k_{z,0}$ is the z wavenumber, and $r_n = |r_n|\exp(\mathrm{i}\psi_{\mathrm{R,n}})$ is a complex known as the reflection coefficient of the nth diffraction order, with $\psi_{\mathrm{R,n}}$ being the reflection phase and $|r_n|^2$ being the reflectivity.

In region II, by following the same procedures for region I, with $k_{\mathrm{II},x,n} = (\varepsilon_{\mathrm{II}}k_0^2 - k_{z,n}^2)^{1/2}$ being the x-wavenumber, the fields can also be derived and are expressed as the sum of the transmitted diffraction modes:

$$H_y^{\mathrm{II}} = \sum_{n=-\infty}^{\infty} t_n H_0 \mathrm{e}^{\mathrm{i}\left(k_{\mathrm{II},x,n}(x-s) + k_{z,n}z\right)}, \tag{2.19}$$

$$E_z^{\mathrm{II}} = -\sum_{n=-\infty}^{\infty} \frac{k_{\mathrm{II},x,n} t_n}{k_0 \varepsilon_{\mathrm{II},r}} \sqrt{\frac{\mu_0}{\varepsilon_0}} H_0 \mathrm{e}^{\mathrm{i}\left(k_{\mathrm{II},x,n}(x-s) + k_{z,n}z\right)}, \tag{2.20}$$

$$E_x^{\mathrm{II}} = \sum_{n=-\infty}^{\infty} \frac{k_{z,n} t_n}{k_0 \varepsilon_{\mathrm{II},r}} \sqrt{\frac{\mu_0}{\varepsilon_0}} H_0 \mathrm{e}^{\mathrm{i}\left(k_{\mathrm{II},x,n}(x-s) + k_{z,n}z\right)}, \tag{2.21}$$

where t_n is the transmission coefficient of the mode.

To accelerate electrons, there should be a vacuum channel in which the electrons travel. In the following, we assume that the media in both region I and region II have a refractive index of 1, i.e., region I and region II are vacuum. In region I, the z wavenumber of the nth diffraction order as shown in Eq. 2.12 can be rewritten as

$$k_{z,n} = k_0 \left(\sin\theta + n\frac{\lambda}{\Lambda}\right). \tag{2.22}$$

In the longitudinal direction, the phase velocity of these diffraction modes can be expressed in term of the z wavenumber as

$$v_{\mathrm{ph},n} = \frac{\omega}{k_{z,n}}. \tag{2.23}$$

For continuous acceleration of the electrons, the synchronicity condition that requires the phase velocity of one diffraction mode to be equal to the electron velocity (v_e) needs to be satisfied. This diffraction order is known as the accelerating mode, or synchronous mode. Using m as the order number of the synchronous mode, the synchronicity condition can be written as

$$v_{\mathrm{ph},m} = v_\mathrm{e} = \beta_\mathrm{e} c, \tag{2.24}$$

with β_e being the electron velocity v_e normalized to the speed of light c.

For the grating period, this result in

$$\Lambda = \frac{m\lambda}{1/\beta_\mathrm{e} - \sin\theta}. \tag{2.25}$$

Obviously, given the electron velocity (β_e), the required grating period (Λ) is determined by the order number of the synchronous mode (m) and the incident angle (θ). Using a higher order or larger incident angle requires a larger grating period, which may simplify the fabrication. However, the first order is preferable since it usually has a higher amplitude than the higher orders.

To explore the property of the accelerating mode, we consider to use a surface-normal incident laser for acceleration, consistent with how experiments with such structures have been typically conducted[20, 21, 26, 27, 29, 30]. In this case, using the first diffraction order requires a grating period that is not longer than the light wavelength,

$$\Lambda = \beta_\mathrm{e}\lambda. \tag{2.26}$$

For the accelerating mode, Eq. 2.26 results in

$$k_{z,m} = k_0/\beta_\mathrm{e}, \tag{2.27}$$

$$k_{x,m} = \mathrm{i}k_0/(\beta_\mathrm{e}\gamma_\mathrm{e}). \tag{2.28}$$

with $\gamma_\mathrm{e} = \sqrt{1-\beta_\mathrm{e}^2}$ being the Lorentz factor. The imaginary value of $k_{x,m}$ indicates that all the diffraction orders other than zeroth order are evanescent and fall off exponentially with an increasing distance from the grating surface in x direction. The decay constant that defines this near wave existing at the surface of the grating is given by

$$\Gamma = \frac{\mathrm{i}}{k_{x,m}} = \frac{\beta_\mathrm{e}\gamma_\mathrm{e}\lambda}{2\pi}. \tag{2.29}$$

Later, it is convenient to rewrite the accelerating mode profiles in region I in terms of the electron parameters,

$$H_{y,m}(x,z) = r_m H_0 \mathrm{e}^{x/\Gamma}\mathrm{e}^{\mathrm{i}k_{z,m}z}, \tag{2.30}$$

$$E_{x,m}(x,z) = \frac{1}{\beta_\mathrm{e}}\sqrt{\frac{\mu_0}{\epsilon_0}}H_{y,m}(x,z), \tag{2.31}$$

$$E_{z,m}(x,z) = \frac{\mathrm{i}}{\beta_\mathrm{e}\gamma_\mathrm{e}}\sqrt{\frac{\mu_0}{\epsilon_0}}H_{y,m}(x,z). \tag{2.32}$$

The accelerating mode profiles in region II can be rewritten as

$$H^{\mathrm{II}}_{y,m}(x,z) = t_m H_0 \mathrm{e}^{-(x-l)/\Gamma}\mathrm{e}^{\mathrm{i}(k_{z,m}z)}, \tag{2.33}$$

$$E^{\mathrm{II}}_{x,m}(x,z) = \frac{1}{\beta_\mathrm{e}}\sqrt{\frac{\mu_0}{\epsilon_0}}H^{\mathrm{II}}_{y,m}(x,z), \tag{2.34}$$

$$E^{\mathrm{II}}_{z,m}(x,z) = -\frac{\mathrm{i}}{\beta_\mathrm{e}\gamma_\mathrm{e}}\sqrt{\frac{\mu_0}{\epsilon_0}}H^{\mathrm{II}}_{y,m}(x,z). \tag{2.35}$$

In the accelerating mode, the Lorentz forces experienced by an electron in region I and region II can be given by Eq. 2.36 and Eq. 2.37, respectively, where ϕ_0 is the start phase of electron in the optical cycle. From the perspective of the accelerating field, a larger start phase ϕ_0 corresponds to a later start time of the electron.

$$F(x,z,t) = \begin{bmatrix}F_x\\F_y\\F_z\end{bmatrix} = \begin{bmatrix}\frac{r_m q}{\beta_\mathrm{e}\gamma_\mathrm{e}^2}\sqrt{\frac{\mu_0}{\epsilon_0}}H_0\mathrm{e}^{x/\Gamma}\mathrm{e}^{\mathrm{i}(k_{z,m}z-\omega t-\phi_0)}\\0\\\frac{\mathrm{i}r_m q}{\beta_\mathrm{e}\gamma_\mathrm{e}}\sqrt{\frac{\mu_0}{\epsilon_0}}H_0\mathrm{e}^{x/\Gamma}\mathrm{e}^{\mathrm{i}(k_{z,m}z-\omega t-\phi_0)}\end{bmatrix}, \tag{2.36}$$

$$F(x,z,t) = \begin{bmatrix}F_x\\F_y\\F_z\end{bmatrix} = \begin{bmatrix}\frac{t_m q}{\beta_\mathrm{e}\gamma_\mathrm{e}^2}\sqrt{\frac{\mu_0}{\epsilon_0}}H_0\mathrm{e}^{-(x-l)/\Gamma}\mathrm{e}^{\mathrm{i}(k_{z,m}z-\omega t-\phi_0)}\\0\\-\frac{\mathrm{i}t_m q}{\beta_\mathrm{e}\gamma_\mathrm{e}}\sqrt{\frac{\mu_0}{\epsilon_0}}H_0\mathrm{e}^{-(x-l)/\Gamma}\mathrm{e}^{\mathrm{i}(k_{z,m}z-\omega t-\phi_0)}\end{bmatrix}. \tag{2.37}$$

The Lorentz forces described in Eq. 2.36 and Eq. 2.37, in which the longitudinal and transverse components serve for acceleration and deflection of particles, respectively, are illustrated in Fig. 2.3. The accelerating force (i.e., longitudinal force) is exerted by the z component of the electric field while the deflecting force (i.e., transverse force) is the combined force exerted by the transverse electric field in the x direction and the transverse magnetic field in the y direction. It is shown that the force experienced by the electrons depends on the start phase and the distance to the grating. The characteristics of the accelerating mode generated by a single grating structure can be seen, e.g., the accelerating mode is a non-radiative wave which exists only close to the grating surface, the acceleration and the deflection are $\pi/2$ out of phase. It shows that an accelerating

scheme using a single grating only allows a small distance between the electron beam and the grating.

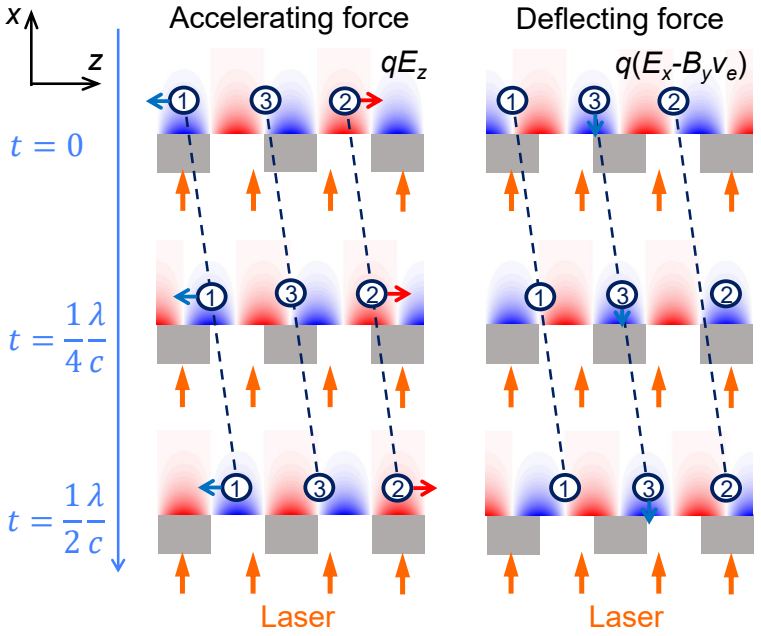

FIGURE 2.3: Illustration of the Lorentz force experienced by an electron in the accelerating mode. The phase velocity of the accelerating mode is matched to the electron velocity. The fields of the accelerating mode decay exponentially away from the grating. The force experienced by the electron can be decelerating (1), accelerating (2), and deflecting (3).

2.2 Field simulation

A crucial advantage of the DLAs compared to the conventional accelerator based on metallic cavities is the high gradient which may enable a compact accelerator. To maximize the accelerating gradient which is limited by the damage threshold of the dielectric material is the primary target for optimization.

To characterize the performance of an accelerating structure, the figure of merit is the accelerating gradient, G_a, which is the average longitudinal electric field experienced by the electrons in an optical cycle. The ratio of the accelerating gradient G_a to the incident electric field E_0, i.e., G_a/E_0, notes the grating's ability to convert the incident field into accelerating field. The ratio of accelerating gradient G_a to the maximum field E_max in vacuum at the grating surface, i.e., $G_\mathrm{a}/E_\mathrm{max}$, notes the fraction of the maximum electric field that can be converted into accelerating field. When an accelerator works with a low input laser power that causes no damage, the highest value of G_a/E_0 should be chosen to maximize the accelerating gradient. When the accelerator works close to the damage threshold, which can be expressed as the maximum sustainable field in the vacuum at

the dielectric surface, the highest ratio of G_a/E_{max} should be chosen to maximize the sustainable accelerating gradient.

In this section, we calculate the accelerating gradient with CST MWS. In addition, the dependence of accelerating gradient on the grating geometries and materials is investigated.

2.2.1 Simulation with CST MWS

CST MWS is commercial software for three-dimensional high-frequency electromagnetic simulation[46]. It can provide a precise calculation for many applications including photonic crystals, cavities, and antennas.

Considering the possibility to conduct the acceleration experiment using a laser system and an electron gun which are being developed at KEK, the grating structure is designed based on the target parameters of those systems, as shown in Table 2.1.

TABLE 2.1: Simulation parameters for electron and laser pulse.

Electron energy (keV)	50
Laser wavelength (μm)	1030
Laser pulse duration (ps)	30
Laser pulse energy (μJ)	> 10
Laser repetition rate (Hz)	20

To utilize the first spatial harmonic to accelerate electrons, a grating period $\Lambda = 425$ nm is required to achieve the phase synchronicity as shown in Eq. 2.26. In this section, we will use fused silica, which has been widely used in previous experiments[20, 21, 47], as the grating material. It has a refractive index of 1.45 and a damage threshold of 3.5 J/cm^2. In Sec. 2.2.2, we will discuss the choice of materials.

To make a single grating structure, the easiest way would probably be to pattern a one-dimensional grating on a wafer with electron-beam lithography and then etch the grating pattern, yielding a periodic structure on the top of a slab, or substrate. Such a structure, namely the slab grating, can be driven by either a laser from the vacuum side or a laser from the slab side, as shown by Figs. 2.4[(a) and (b)], respectively. Using the transmission mode, an anti-reflection layer will be required at the interface between the slab and air. Besides, our simulation shows that sustainable accelerating gradients for transmission mode and reflection mode are almost the same. As such, the incidence of laser from the vacuum side is considered as a better solution and will be studied in this section. The rectangular pillar grating in Fig. 2.4(c) and elliptical pillar grating in

Fig. 2.4(d) require extra efforts for fabrication due to their three-dimensional nature, so they will not be considered in the simulation of single-grating structures. However, in Chapter 3, such structures will be considered for double gratings.

In Fig. 2.5(a), the setup in the simulation is shown. Only one period of the grating is needed in the field simulation, with periodic boundary conditions in the z direction, open boundary conditions in the x direction, and magnetic boundary conditions in the y direction. Grating dimensions: pillar height s, pillar width b, grating period Λ. A TM-polarized plane wave with a wavelength of λ is incident from above at normal incidence to the grating surface, with the electric field along the z direction. The electrons of velocity $v_\mathrm{e} = \beta_\mathrm{e} c$ are assumed to propagate in z direction. The mesh coarseness is $\lambda/80$.

As an example to illustrate the simulation method, we use a grating thickness $s = 288$ nm and a pillar width $b = 225$ nm. In the simulation, CST time domain solver calculate the electromagnetic fields at a steady state on a Cartesian grid. Extracting the fields, we can obtain the field amplitude $\mathbf{A}(x, y, z)$ and phase $\varphi_0(x, y, z)$ on the grid. Since the grating structure is two-dimensional, the field is constant in the y direction. The instantaneous field oscillating with time can be given by

$$\widehat{\mathbf{A}}(x, z, t) = \mathbf{A}(x, z)\mathrm{e}^{\mathrm{i}(\varphi_0(x,z)-\omega t)}. \tag{2.38}$$

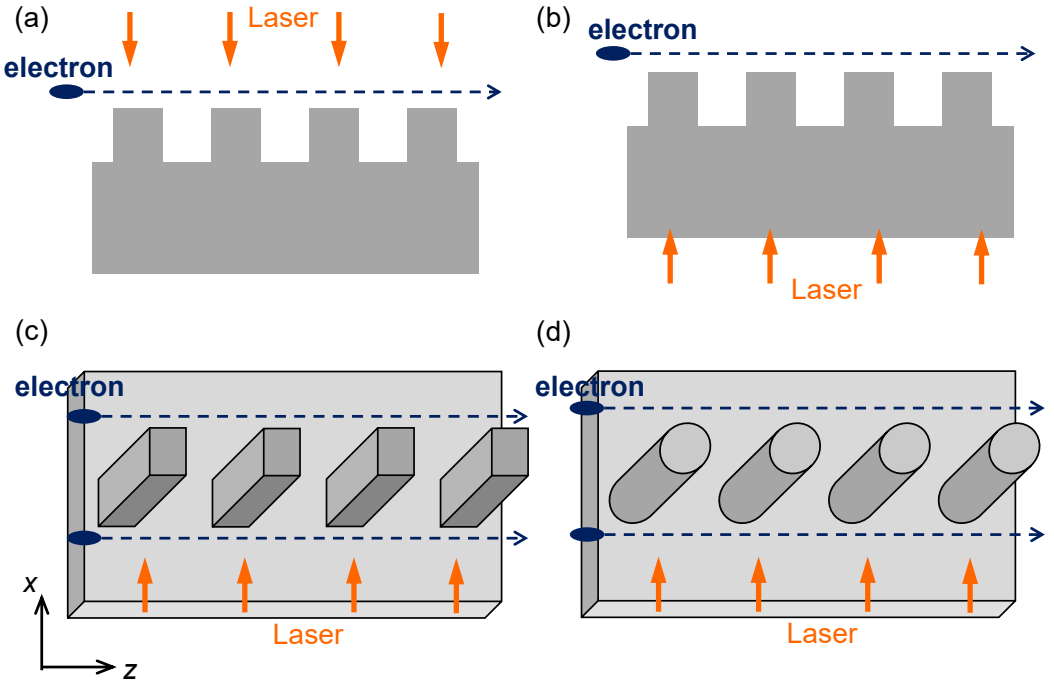

FIGURE 2.4: Different designs of single grating structures. (a) Slab grating driven by a laser from the vacuum side[26, 27]. (b) Slab grating driven by a laser from the substrate side[20, 47]. (c) Rectangular pillar grating. (b) Elliptical pillar grating.

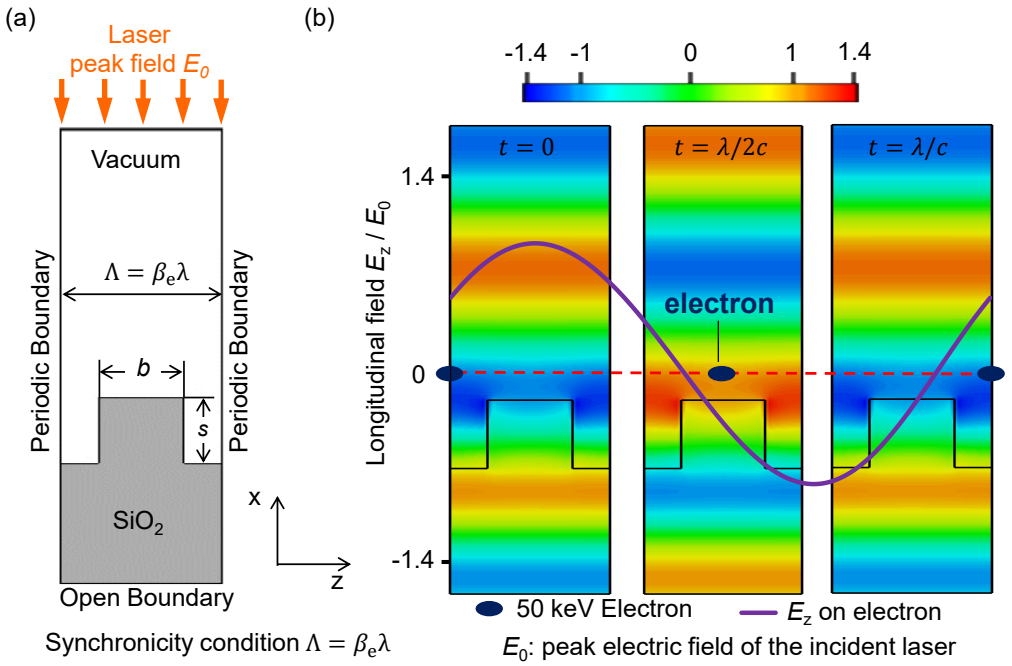

FIGURE 2.5: Field simulation of a single grating with CST MWS. (a) Simulation setup showing the boundary conditions. Grating pillar height s, pillar width b, grating period Λ, laser wavelength λ, electron velocity $v_e = \beta_e c$. (b) Snapshots of the longitudinal field at every half optical cycle $E_z(t = 0, \lambda/2c, \lambda/c)$. The instantaneous longitudinal field E_z experienced by the electron launched at $t = 0$ from the left is shown by the purple curve, while the red dashed line represents $E_z = 0$. $x = 0$ is located at the pillar upper surface of the grating. Simulation parameters: $\lambda = 1030$ nm, $\beta_e = 0.41$, $\Lambda = 425$ nm, $s = 288$ nm, $b = 225$ nm.

The accelerating gradient G_a and deflection gradient G_d can be calculated by Eq. 2.39 and Eq. 2.40, respectively, where ϕ_0 is the phase of electron in the optical cycle at $z = 0$, namely start phase. For convenience, in the simulation we can assume an incident wave with a peak field $E_0 = 1$, so the calculated gradients can be treated as the value normalized to the incident field E_0. Since the energy gain of electrons in a grating period is rather small, we can neglect the energy variation and assume $z(t) = v_e t$.

$$G_a(x_0, \phi_0) = \frac{1}{\Lambda}\int_0^{\Lambda} E_z[x_0, z(t, \phi_0), t(z)]dz, \tag{2.39}$$

$$G_d(x_0, \phi_0) = \frac{1}{\Lambda}\int_0^{\Lambda} (E_x[x_0, z(t, \phi_0), t] - v_e B_y[z(t), t])dz. \tag{2.40}$$

In Fig. 2.5(b), we show the snapshots of the calculated electric field at every half optical cycle, which is comprised of a series of diffraction modes. The maximum longitudinal electric field is located around the corner of the pillar. Above the grating, the fields closer to the grating are modulated more significantly due to the evanescent fields existing close to the grating surface. For an electron launched $t = 0$, the electric field experienced by the electron, $E_z[x_0, z(t, \phi_0), t]$, is shown by the purple curve. The red dashed line at

the center represents $E_z = 0$. The average longitudinal electric field experienced by the electron is above zero, so the electron can experience net energy gain over every optical cycle and be accelerated.

Once the gradient G_a, field ratios G_a/E_0, and $G_\mathrm{a}/E_\mathrm{max}$ are obtained, the performance of the single grating structure can be estimated based on the laser parameters as shown in Table 2.1. The laser pulse duration $\tau_\mathrm{p} = 30$ ps corresponds to a damage threshold $F_\mathrm{th} = 7$ J/cm^2 for fused-silica bulk[22]. The dependence of peak electric field on the fluence F_in of a Gaussian laser pulse can be given by

$$E_0 = \sqrt{0.94\frac{2F_\mathrm{in}}{c\varepsilon_0\tau_\mathrm{p}}}. \tag{2.41}$$

Therefore, the acceleration gradient at the damage threshold can be given by

$$G_\mathrm{a} = \left(\frac{G_a}{E_\mathrm{max}}\right)\sqrt{0.94\frac{2F_{th}}{c\epsilon_0\tau_\mathrm{p}}} = 1.29\left(\frac{G_\mathrm{a}}{E_\mathrm{max}}\right)\ (\mathrm{GV/m}), \tag{2.42}$$

where $G_\mathrm{a}/E_\mathrm{max}$ is the ratio of the accelerating gradient to the maximum in-vacuum field at the grating surface calculated in the simulation.

Figure 2.6(a) shows the maximum sustainable accelerating gradient G_a and deflecting gradient G_d in the vicinity of the grating as shown in Fig. 2.5(b), with a start phase that can maximize the gradient. Figure 2.6(b) shows the maximum sustainable gradients as a function of the start phase ϕ_0, at a distance of 50 nm. The characteristics of the accelerating mode at a single grating shown here are in agreement with those shown in Fig. 2.3, e.g., the fields decay exponentially with the distance, the acceleration and deflection are 90 degrees out of phase. For one electron starting at a distance of 50 nm to the grating, the maximum accelerating gradient is about 60 MV/m.

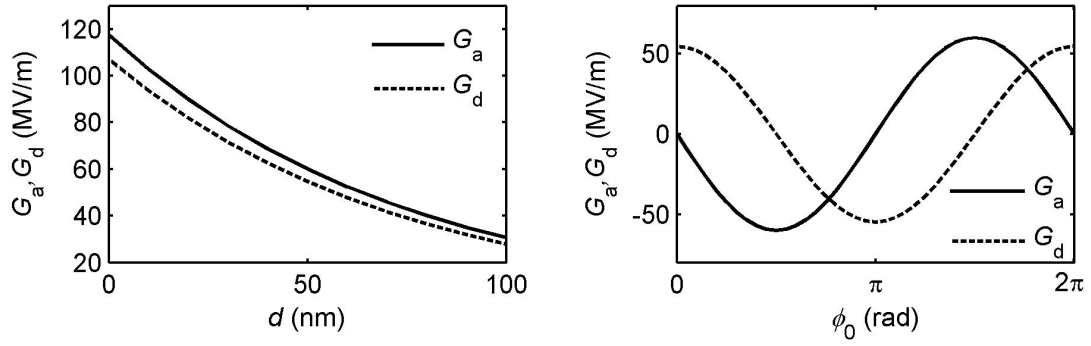

FIGURE 2.6: Sustainable gradients in the vicinity of the grating. (a) Accelerating gradient G_a and delecting gradient G_d versus distance d to the grating, with an optimum start phase. (b) Gradients as a function of start phase ϕ_0, at a distance of 50 nm to the grating. Refer to Fig. 2.5(b) for simulation parameters.

2.2.2 Optimization of grating dimensions and materials

The maximum sustainable gradient of a single grating structure depends on the field ratio G_a/E_{max} and the damage threshold of the material. First, we will show how to maximize G_a/E_{max} by optimizing the grating dimensions, including the pillar width b and pillar height s.

In the simulation, as shown in Sec. 2.2.1, both the accelerating and deflecting gradients depend on the start phase and the distance to the grating. Therefore, when we optimize the structure dimensions and materials, we always set the start phase as the one that can maximize the gradients and assume a distance of 50 nm.

The grating dimensions can be optimized with a parameter scan. In Fig. 2.7(a) and Fig. 2.7(b), we show the $s-b$ maps of the field ratio G_a/E_0 and G_a/E_{max}, respectively. Comparison between Fig. 2.7(a) and Fig. 2.7(b) shows that the optimum dimensions for G_a/E_0 and G_a/E_{max} are very close. As a result, the optimized grating are chosen to have a pillar height $s = 288$ nm and a pillar width $b = 225$ nm, with $G_a/E_{max} = 0.047$ and $G_a/E_0 = 0.065$. Please note that the optimized grating dimensions correspond to the structure which has been studied in the Sec. 2.2.1, as shown in Fig. 2.5(b). Since later in this chapter, the optimized fused-silica grating will be frequently used, we summarize its parameters in Table 2.2.

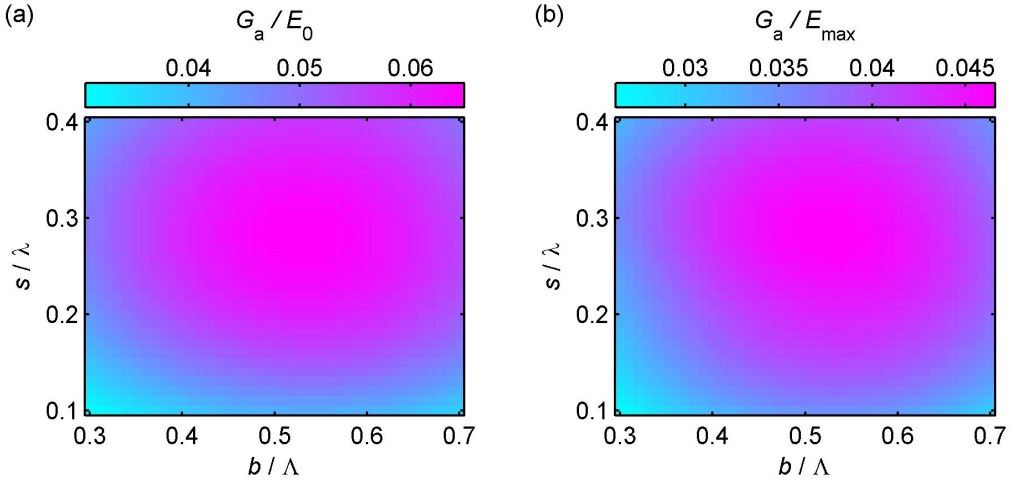

FIGURE 2.7: Maps of ratio G_a/E_0 (a) and G_a/E_{max} (b) resulting from a parameter scan of grating pillar height s and pillar width b for a fused-silica grating.

The capability of dielectrics to sustain high electric field is one of the most important reasons that make DLA attractive. Many dielectric materials can be used in DLA, whose damage thresholds are shown in Fig. 2.8, with a laser pulse duration of 1 ps and wavelength of 800 nm. However, to utilize the well-developed fabrication technique in semiconductor industry, here we will consider only fused silica and silicon. The threshold

TABLE 2.2: Parameters of the optimized fused-silica single grating.

Grating period Λ	425 nm
Pillar width b	225 nm
Pillar height s	288 nm
Field ratio G_a/E_0 ($d = 50$ nm)	0.065
Field ratio G_a/E_{max} ($d = 50$ nm)	0.047

fluence is 2.02 J/cm^2 for SiO_2, and 0.18 J/cm^2 for Si. With Eq. 2.41, the sustainable in-vacuum fields E_{th} are calculated to be 3.79 GV/m for SiO_2 and 1.13 GV/m for Si, and consequently $E_{th}(SiO_2)/E_{th}(Si) = 3.35$.

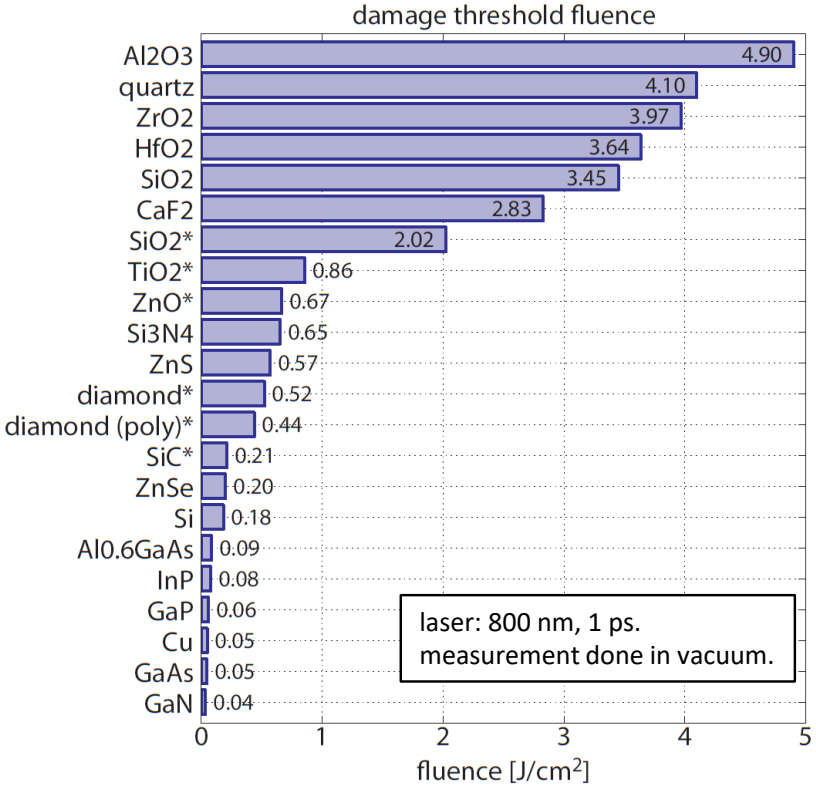

FIGURE 2.8: Damage threshold of a variety of materials. Measurements were conducted with a 1 ps, 800 nm, 600 Hz Ti:Sapphire laser. Taken from [48].

To compare these materials, we need to estimate their highest sustainable gradients. In Fig. 2.7, the gradients of fused-silica grating have been presented. Although they were obtained by assuming a laser wavelength of 1030 nm, because Maxwell's equations are linear and scalable in both space and time, the normalized values of pillar width b and pillar height s also apply to a wavelength of 800 nm, neglecting the small change in permittivity.

In Fig. 2.9 we show the field ratios G_a/E_0 and G_a/E_{max} resulting from a parameter scan of grating pillar height s and pillar width b for a silicon grating, with a laser wavelength

of 1030 nm. The maximum $G_a/E_{max} = 0.086$, and the maximum $G_a/E_{max} = 0.29$.

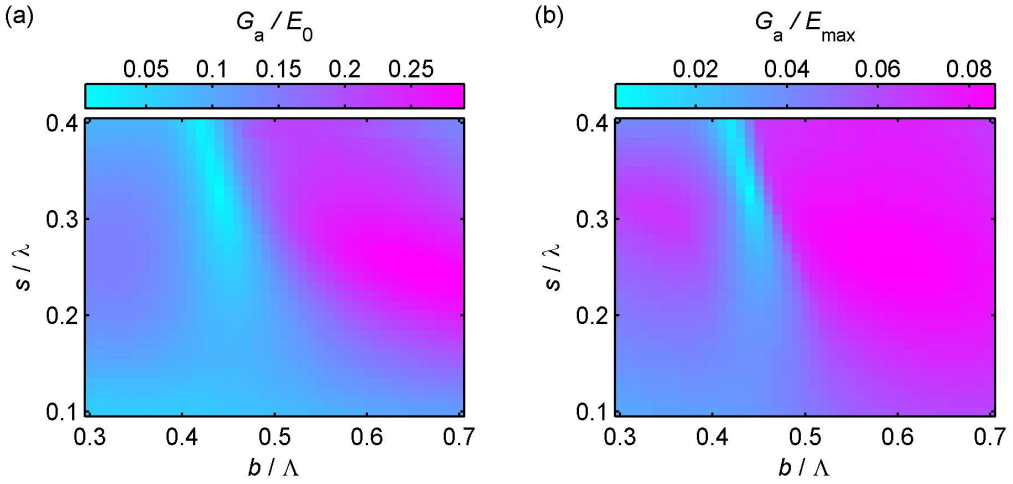

FIGURE 2.9: Maps of ratio G_a/E_0 (a) and G_a/E_{max} (b) resulting from a parameter scan of grating pillar height s and pillar width b for a silicon grating.

Based on Fig. 2.7 and Fig. 2.9, the performance of fused-silica grating and silicon grating can be compared. On one hand, the silicon grating has a four-fold larger ratio G_a/E_0 than the fused-silica grating. To excite a given accelerating gradient without damage, fused-silica grating needs a four-fold higher incident field than silicon grating. On the other hand, assuming a laser pulse length of 1 ps, by using the damage threshold as shown in Fig. 2.8, the sustainable accelerating gradient at a distance of 50 nm is 177 MV/m for the fused-silica grating and 97 MV/m for the silicon grating. Currently, the commercial laser system can deliver laser pulses with a power higher than that required by DLA. Considering this, fused-silica is a better material to enable high-gradient acceleration of 50 keV electrons.

It is worth noting that, in the DLA, the electrical conductivity of materials is another factor that might need to be considered in the experiment. Semiconductor materials, e.g., silicon material, don't any special treatment to handle the charging problem, which is severe in subrelativistic electron acceleration due to the deflection. By comparison, insulating materials, e.g., fused silica, need a conductive coating or the laser illumination to dissipate charge buildup[47, 48].

Furthermore, the fabrication and integration capabilities for materials should also be considered. In this respect, silicon is superior to the others due to its wide application in the semiconductor industry. Lithography and etching techniques can ensure the high-resolution fabrication of silicon structures. Silicon also provides an excellent platform for monolithically integrating the accelerator structures and the laser-power-delivery system.

For these reasons, fused-silica and silicon are considered to have their advantages and can be applied to actual design according to different requirements. In Chapter 3 and 4, we will design two silicon DLA structures by making use of a unique characteristic of high-contrast subwavelength gratings.

2.3 Particle tracking simulation

To study the electron acceleration above a single grating, a particle tracking simulation is needed. CST Particle Studio is widely used for this purpose. However, it is time-consuming and requires a large memory. Therefore, we develop a particle tracking program based on motion equations to evaluate the energy gain of electrons. We will show that the deflecting fields cause severe electron loss and the dephasing effect limit the energy gain.

2.3.1 Particle tracking method

In the calculation, we assume $\Delta\beta_\mathrm{e}/\beta_\mathrm{e} \ll 1$ over one grating period, which is true when the electron's energy gain over one wavelength of the incident field is well below the electron's rest energy m_0c^2, i.e., $G_\mathrm{a} \ll m_0c^2/\lambda \approx 496$ GV/m. In a DLA driven by an infrared laser, the general acceleration gradient $G_\mathrm{a} < 10$ GV/m, so that the assumption is valid.

A Gaussian laser beam is used to drive many periods of grating. Since the effect of asynchronous modes is averaged to zero over time, they can be neglected in the simulation[49]. To begin with, the acceleration gradient for the synchronous electron is rewritten as

$$G_\mathrm{a}(x,z,t) = \frac{c}{\beta_\mathrm{e}\gamma_\mathrm{e}} B_y(z,t) e^{-x/\Gamma}. \tag{2.43}$$

In Sec. 2.2.1, we have already obtained with CST MWS the field ratio G_a/E_0 as a function of start phase at a distance $x_0 = 50$ nm. With $G_{\mathrm{a},0}$ denoting the maximum accelerating gradient at a distance of 50 nm to the grating, the longitudinal field of the accelerating mode can be rewritten as

$$E_z(x,z,t) = \left(\frac{G_{\mathrm{a},0}}{E_0}\right) E_\mathrm{in} e^{-(x-x_0)/\Gamma} \sin(k_z z - \omega t + \psi_{R,1}). \tag{2.44}$$

The x electric field and y magnetic field of the accelerating mode are also rewritten in terms of E_z.

$$E_x(x,z,t) = \gamma_\mathrm{e} E_z(x,z,t),, \tag{2.45}$$

$$B_y(x,z,t) = \frac{\gamma_\mathrm{e}\beta_\mathrm{e}}{c} E_z(x,z,t).. \tag{2.46}$$

As a Gaussian beam, the incident laser pulse has a field profile that can be described as

$$E_\mathrm{in} = E_0 \mathrm{e}^{-(\frac{z-z_0}{w_0})^2 - 2\ln(2)(\frac{t-t_0}{\tau_\mathrm{p}})^2} \cos(-k_0 x - \omega t). \tag{2.47}$$

Based on Eqs. 2.44-2.47, the instantaneous fields of the accelerating mode can be obtained,

$$E_\mathrm{a}(x,z,t) = \left(\frac{G_{\mathrm{a},0}}{E_0}\right) e^{-(x-x_0)/\Gamma} E_0 \mathrm{e}^{-(\frac{z-z_0}{w_0})^2 - 2\ln(2)(\frac{t-t_0}{\tau_\mathrm{p}})^2} \sin(k_z z - \omega t + \psi_{R,1}). \tag{2.48}$$

Next, we need to calculate the electron's energy and x position after interaction with the accelerating mode. For clarity, β and γ without subscript are used to represent the instantaneous parameters for the electrons traversing the grating, while β_e and γ_e are used to represent the initial parameters of those electrons that satisfy the synchronicity condition. Note that in the calculation, we assume the charge of the electron to be $e = 1.6 \times 10^-19$ C, ignoring the minus sign. We use $\phi_0 = \omega t_0 - \psi_{R,1}$ to denote the start phase of electron, $\phi = k_z z - \omega t + \psi_{R,1} = k_z z - \omega(t - t_0) - \phi_0$ to denote the phase of the electron in the optical cycle, with t_0 being the time when the electron is launched at $z = 0$. Since the electrons' transverse velocity is much smaller than the longitudinal velocity, so we can neglect the contribution of the transverse velocity to the total kinetic energy. From the theorem of kinetic energy, we obtain the longitudinal motion equation

$$\frac{\mathrm{d}\gamma m_0 c^2}{\mathrm{d}z} = e\left(\frac{G_{\mathrm{a},0}}{E_0}\right) e^{-(x-x_0)/\Gamma} E_0 \mathrm{e}^{-(\frac{z-z_0}{w_0})^2 - 2\ln(2)(\frac{t-t_0}{\tau_\mathrm{p}})^2} \sin\phi, \tag{2.49}$$

$$\frac{\mathrm{d}\phi}{\mathrm{d}z} = k_0\left(\frac{1}{\beta_e} - \frac{\gamma}{\sqrt{\gamma^2-1}}\right). \tag{2.50}$$

From the theorem of momentum, the transverse motion equation can be given by

$$\frac{\mathrm{d}\gamma_e m_0 v_x}{\mathrm{d}t} = e\gamma_\mathrm{e}\left(1 - \beta_\mathrm{e}\beta\right)\left(\frac{G_{\mathrm{a},0}}{E_0}\right) \mathrm{e}^{-(x-x_0)/\Gamma} E_0 \mathrm{e}^{-(\frac{z-z_0}{w_0})^2 - 2\ln(2)(\frac{t-t_0}{\tau_\mathrm{p}})^2} \cos\phi \tag{2.51}$$

$$\frac{\mathrm{d}x}{\mathrm{d}t} = v_x \tag{2.52}$$

By using $\frac{\mathrm{d}}{\mathrm{d}t} = \beta c \frac{\mathrm{d}}{\mathrm{d}z}$, equation (2.51) and (2.52) can rewritten as

$$\frac{\mathrm{d}\gamma m_0 v_x}{\mathrm{d}z} = e\frac{\gamma_\mathrm{e}\left(1-\beta_\mathrm{e}\beta\right)}{\beta c}\left(\frac{G_{\mathrm{a},0}}{E_0}\right)\mathrm{e}^{-(x-x_0)/\Gamma}E_0\mathrm{e}^{-(\frac{z-z_0}{w_0})^2-2\ln(2)(\frac{t-t_0}{\tau_\mathrm{p}})^2}\cos\phi \tag{2.53}$$

$$\frac{\mathrm{d}x}{\mathrm{d}z} = \frac{v_x}{\beta c} \tag{2.54}$$

Based on the motion equations (Eqs. 2.49, 2.50, 2.53 and 2.54), we could track the particle powered by a gaussian laser pulse.

To verify the method, a code was developed accordingly. It the following, the code will be verified by comparing the results obtained with it with those obtained with CST. In the simulation, we assume a laser pulse with wavelength $\lambda = 1030$ nm, beam waist radius $w_0 = 1$ μm and pulse duration $\tau_\mathrm{p} = 50$ fs. We use the optimized fused-silica single grating calculated in Sec. 2.2.1 as the accelerator structure. The grating is 11 periods long, with a grating period $\Lambda = 425$ nm, a pillar height $s = 288$ nm and a pillar width

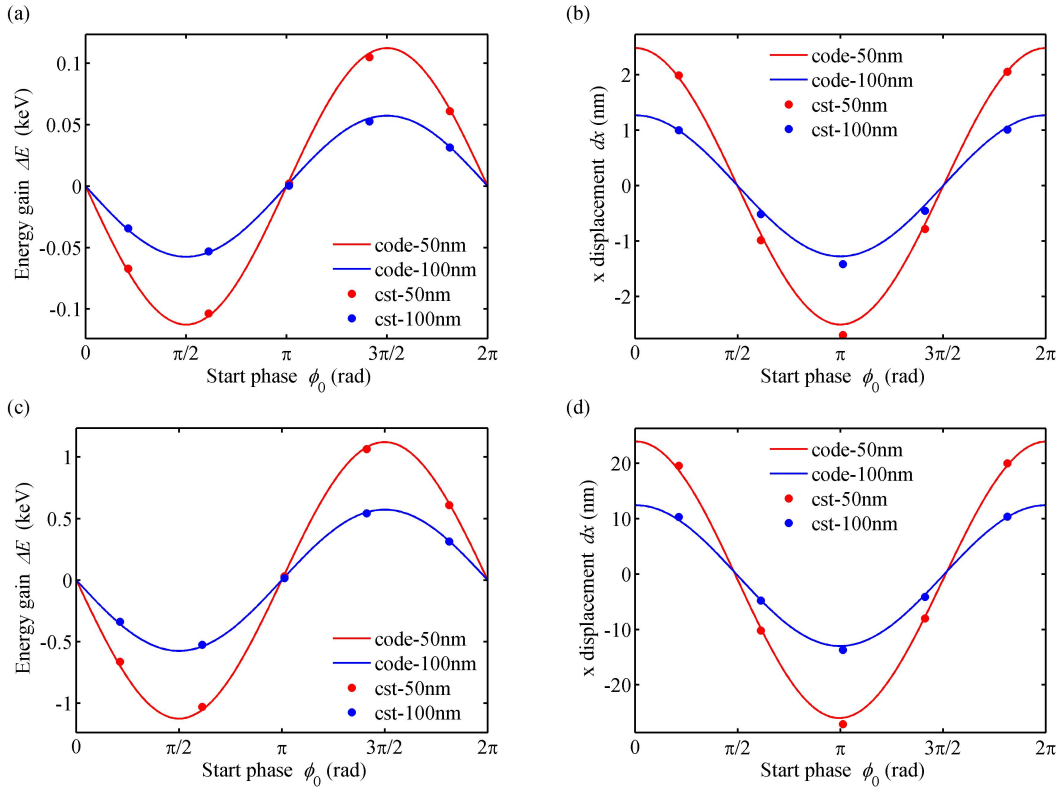

FIGURE 2.10: Comparison of electron parameters at the exit from the code and CST particle tracking solver. The curves show the energy gain ΔE [(a) and (c)] and the x displacement [(b) and (d)] as a function of start phase ϕ_0 at an initial distance 50 nm (red) and 100 nm (blue), respectively. The peak field $E_0 = 1$ GV/m [(a) and (b)], $E_0 = 10$ GV/m [(c) and (d)]. The electrons with an energy of 50 keV are launched at different start phases and distances from the grating surface. The structure has 11 periods of grating, with grating period $\Lambda = 425$ nm, pillar height $s = 288$ nm and pillar width $b = 225$ nm, is illuminated by a laser with wavelength $\lambda = 1030$ nm, beam waist radius $w_0 = 1$ μm, and pulse duration $\tau_\mathrm{p} = 50$ fs.

$b = 225$ nm. In Fig. 2.10, we show the final electron parameters obtained from the code and CST particle tracking solver. The curves show the energy gain ΔE [Fig. 2.10(a) and Fig. 2.10(c)] and the displacement in the x direction [Fig. 2.10(b) and Fig. 2.10(d)] as a function of start phase ϕ_0 at an initial electron-grating distance of 50 nm (red) and 100 nm (blue), respectively. The laser has a peak field of $E_0 = 1$ GV/m in Fig. 2.10(a) and Fig. 2.10(b), and $E_0 = 10$ GV/m in Fig. 2.10(c) and Fig. 2.10(d). It can be seen that the results obtained from the code are in agreement with the results obtained with CST.

In Fig. 2.11, we show the instantaneous electron parameters, including electron energy and distance to the grating surface, as a function of z position obtained from the code (red) and CST particle tracking solver (blue). The parameters correspond to the second left red dot in Figs. 2.10[(c) and (d)]. An electron with an initial energy of 50 keV are launched at a start phase $\phi_0 = 1.91$ rad and an initial distance $d = 50$ nm to the grating surface, powered by a laser pulse with a peak electric field $E_0 = 10$ GV/m. It can be seen that at the end of the grating, the electron energy and displacement obtained by the code are in agreement with the results obtained with CST. However, there are significant differences in the electron energy before it arrives at the end, which is because in the code the spatial harmonics other than the accelerating mode are neglected. The oscillation of the curve obtained by CST is mainly caused by the zeroth diffraction mode.

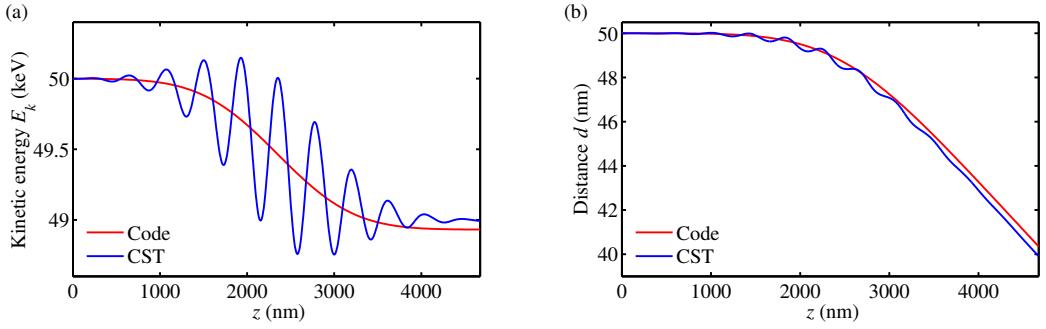

FIGURE 2.11: Comparison of instantaneous electron parameters as a function of z position obtained with the code and CST particle tracking solver. The curves show the energy gain ΔE (a) and the lateral displacement in the x direction (b) as a function of z position. Identical parameters for the second left red dot in Figs. 2.10[(c) and (d)] are used. The electrons with an initial energy of 50 keV are launched at a start phase $\phi_0 = 1.91$ rad and initial distances $d = 50$ nm from the grating surface, powered by a laser pulse with a peak electric field $E_0 = 10$ GV/m. The structure has 11 periods of grating, with a grating period $\Lambda = 425$ nm, pillar height $s = 288$ nm, and pillar width $W_p = 225$ nm. The laser pulse is with a wavelength $\lambda = 1030$ nm, a beam waist radius $w_0 = 1$ μm, and a pulse duration $\tau_{\mathrm{p}} = 50$ fs.

2.3.2 Particle tracking of electrons above a single grating

Using this code, we can evaluate the energy gain and x displacement of electrons above a grating structure powered by a Gaussian laser pulse. We will show that the relative

phase of the electron with respect to the accelerating mode changes as the electron gains energy, known as the dephasing process. This effect which may lead to the reduction of the acceleration gradient, or even result in deceleration. In this case, the energy gain depends not only on the field ratio G_a/E_0 but also on the variation of the phase of an electron in the optical cycle.

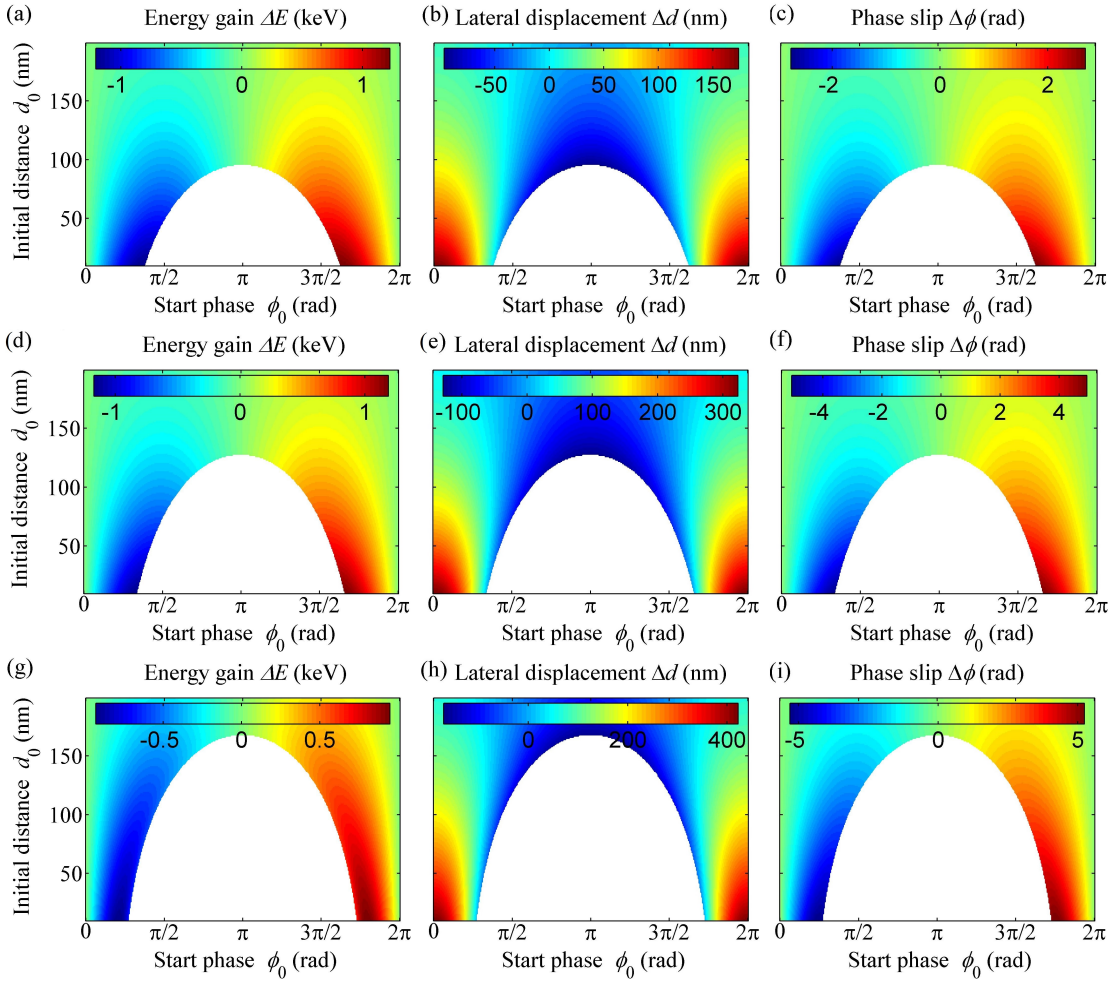

FIGURE 2.12: Particle tracking results for a double grating structure. The electrons with an initial energy of 50 keV are launched at different start phases and initial distances from the grating surface. The colored maps show the energy gain ΔE [(a), (d) and (g)], the deflected lateral displacement dx [(b), (e), and (h)] and the phase slip of the electrons in the accelerating mode $\Delta\phi$ [(c), (f), and (i)]. The white areas represents those electrons crashed into the grating structures. The structures with a grating period $\Lambda = 1030$ nm and total widths $W = 30$ μm [(a)–(c)], $W = 60$ μm [(d)–(f)] are illuminated by a laser with a wavelength $\lambda = 1550$ nm, laser beam waist radiuses $w_0 = 10$ μm [(a)–(f)], $w_0 = 20$ μm [(g)–(i)], a peak fluence $F_{\text{in}} = 3.62$ J/cm^2 and a pulse duration $\tau_{\text{p}} = 20$ ps.

In Fig. 2.12 we show the particle tracking results for 50 keV electrons in the vicinity of the optimized fused-silica grating. The laser parameters are shown in Table 2.1, and the grating parameters are show in Table 2.2. The electrons with an initial energy of 50 keV are launched at different start phases and initial distances from the grating surface. Here, the start time for a zero start phase is set that those electrons can experience

the maximum peak electric field around the grating center. The white areas represent those electrons crashed into the grating structures, or lost electrons. We change the total number of grating periods and the waist radius w_0 of the laser beam. As suggested in Sec.2.2.1, we use a peak incident electric field $E_0 = 0.92$ GV/m, corresponding to a maximum fluence $F_{\text{in}} = 3.62$ J/cm^2 below the damage threshold[22], considering the field enhancement.

Figures 2.12[(a), (d) and (g)] show the energy gain of electrons with different initial distances and start phases. Comparison between Fig. 2.12(a) and Fig. 2.12(d) shows that with a given laser pulse, increasing the total grating length does not lead to an increase in energy gain. A total grating width of 30 μm is long enough to cover the effective interaction length with a laser beam waist of 5 μm. Comparison between Fig. 2.12(d) and Fig. 2.12(g) shows that for a given total grating width, increasing the laser waist may not necessarily lead to higher energy gain. This is caused by the dephasing effect during the interaction, as shown in Figs. 2.12[(d), (f) and (i)]. The phase of an electron in the optical cycle changes as the electron gains energy. For example, one electron starting at an optimum start phase $\phi_0 = 3\pi/2$ and a distance of 50 nm experience a phase slip around -2 rad during the interaction. In this case, the electron moves from the accelerating phase to the decelerating phase, leading to a decreasing of the energy gain. The maximum energy gain is expected to be ~ 1 keV in the experiment.

Despite the dephasing effect, the characteristics of the single-grating DLA for non-relativistic electrons can be seen in Figs. 2.12, e.g., the accelerating mode is a non-radiative wave and can only accelerate electrons close to the grating surface, the strong deflection force could result in electron loss, and the acceleration and the deflection are $\pi/2$ out of phase. By comparing Figs. 2.12[(a)–(c)] and Figs. 2.12[(d)–(f)], one can see that with fixed laser parameters, the maximum energy gain of electron is affected by the total width of the grating which determines the number of grating periods. Due to the dephasing effect and the deflection, one may obtain a smaller energy gain with more grating periods. By comparing Figs. 2.12[(d)–(f)] and Figs. 2.12[(g)–(i)], we can see that, given a grating structure, higher laser energy may lead to a lower energy gain as a result of the dephasing problem.

Figure 2.13 shows the simulated electron parameters along z direction. We show the instantaneous kinetic energy E_k, the acceleration gradient G_{a}, the distance between electron and grating surface d, the deflection gradient G_{d}, the laser electric field amplitude experienced by the electron E_{in} and the phase of electron in the optical cycle ϕ. The 50 keV electrons at an initial distance of $d = 50$ nm from the grating surface are launched at the optimal start phases that enable the maximum energy gain without crashing into the grating. It is shown that the dephasing effect could be so severe that

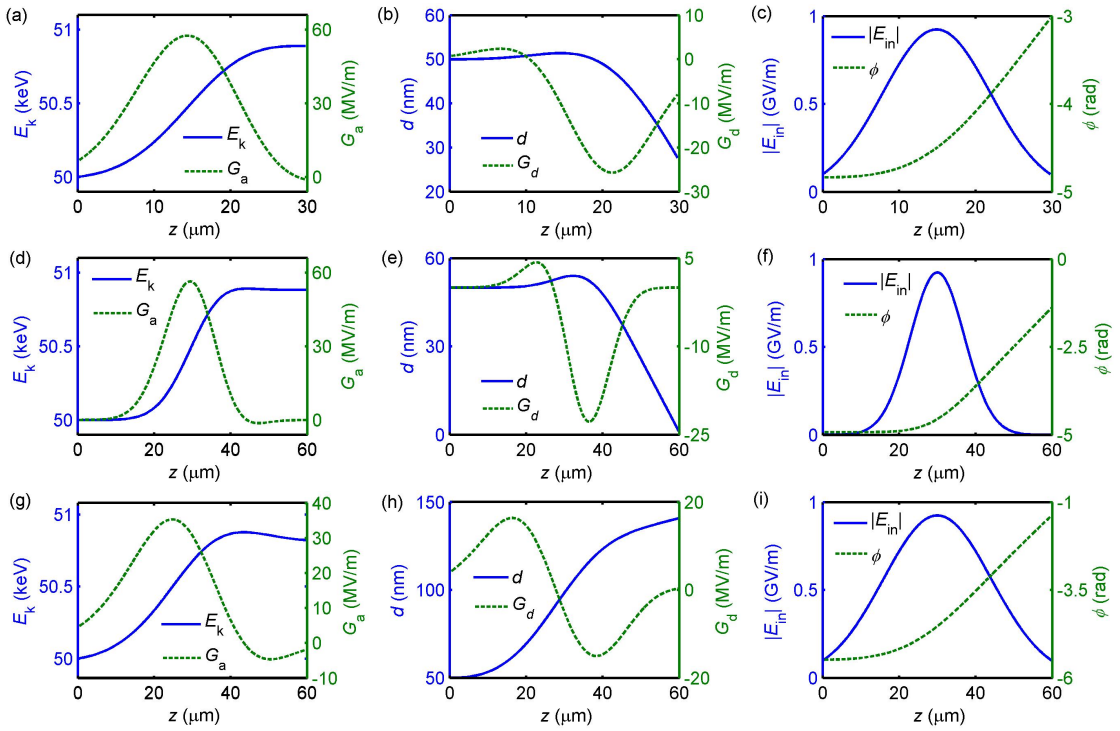

FIGURE 2.13: Instantaneous electron parameters as a function of z position. We show the instantaneous kinetic energy E_k [blue curves in (a), (d), and (g)], the acceleration gradient G_a [green curves in (a), (d), and (g)], the distance between electron and grating surface d [blue curves in (b), (e), and (h)]), the deflection gradient G_d [green curves in (b), (e), and (h)], the laser electric field amplitude experienced by the electron E_{in} [blue curves in (c), (f), and (i)] and the phase of electron in the optical cycle ϕ [green curves in (c), (f), and (i)]. The 50 keV electrons at an initial distance of $d = 50$ nm from the grating surface are launched at the optimal start phases enabling the maximum energy gain without crashing into the grating. (a)–(c) Identical parameters in Figs. 2.12[(a)–(c)] are used, with start phase $\phi_0 = 4.83$ rad. (d)–(f) Identical parameters in Figs. 2.12[(d)–(f)] are used, with start phase $\phi_0 = 4.92$ rad. (g)–(i) Identical parameters in Figs. 2.12[(g)–(i)] are used, with start phase $\phi_0 = 5.48$ rad.

the electron may be decelerated after initial acceleration, i.e., the electron moves from the acceleration phase to the deceleration phase. To mitigate the dephasing problem, we can change the grating period in accordance with electron energy. In this case, a higher energy gain could be obtained.

2.3.3 The limitations of a single grating

As is shown in Section 2.3.2, the accelerating field at a single grating is evanescent and fall off exponentially with an increasing distance from the grating surface in x direction. The skew profile is not desirable for a practical accelerator since it results in a large energy spread.

To clarify this point, in the particle tracking simulation as shown in Fig. 2.12(a), we assume a Gaussian electron beam profile in the x direction, with a beam waist of 20 nm

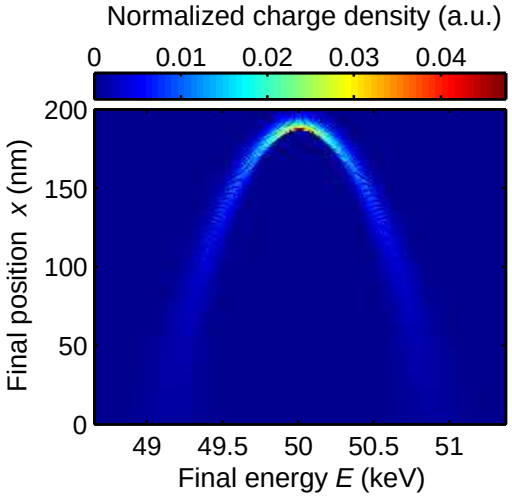

FIGURE 2.14: Charge density map as a function of x position and energy E after interaction. The electron beam has a Gaussian profile in the x direction, with a beam waist of 20 nm and the beam center being $x_0 = 75$ nm. The other simulation parameters are identical with those in Figs. 2.12[(a)–(c)].

and the beam center being $x_0 = 75$ nm. This beam configuration can be treated as the acceleration of a longitudinally uniform electron beam with a pulse duration of one optical cycle and a Gaussian profile in the x direction. In Fig. 2.14, the charge density as a function of x position and energy E after interaction is shown. As those electrons with litter energy gain experience a high deflecting gradient, they are pushed away from the electron beam axis. Those electrons which experience a large deflecting force in minus x direction crash into the grating structures and cannot survive after the interaction.

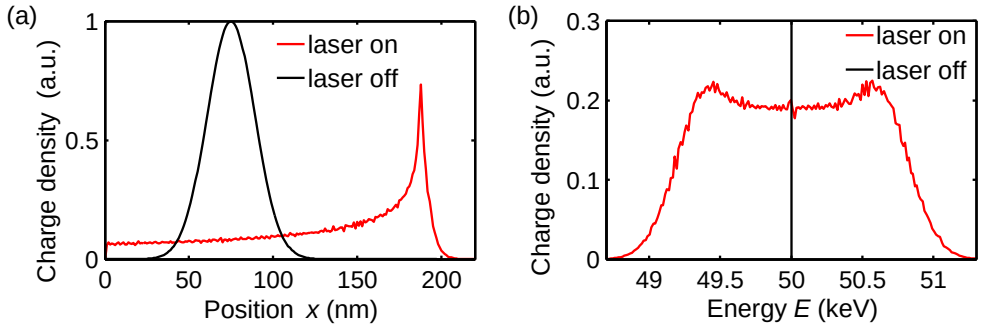

FIGURE 2.15: Charge density versus x position (a) and energy E (b) before (black) and after (red) the interaction at a single grating. The electron beam has a Gaussian profile in the x direction, with a beam waist of 20 nm and the beam center being $x_0 = 75$ nm. The other simulation parameters are identical with those in Figs. 2.12[(a)–(c)].

Figure. 2.15(a) shows the normalized charge density before and after the interaction. About 78% of the electrons can survive after the interaction, but most of these survived electrons have moved away from the original electron beam axis. Figure. 2.15(b) shows the energy of the electrons before and after the interaction. It is shown that, during the

interaction, some of the electrons are accelerated while some are decelerated, depending on the start phase.

Since a single grating can only provide an accelerating mode which causes a large energy spread, an accelerating structure that provides a better field profile should be developed. In the next chapter, we will discuss the double gating structure that enables a more uniform accelerating field.

Chapter 3

Resonant double grating structures

In an accelerator, the beam quality is a figure of merit to characterize its performance. In a single grating structure, as discussed in Chapter 2, the evanescent accelerating field leads to a large energy spread, which severely limits its usefulness. In this chapter, we present a method to generate a uniform accelerating mode by using a double-grating resonator with single-sided illumination. We further discuss its performance based on the field simulation and particle tracking simulation results. Additionally, we discuss the accelerator parameters of a 1 MeV electron source for radiobiology research. Part of the content of this chapter follows [50].

3.1 Theory of a resonant double grating

In this section, we will show that, by introducing a second grating, a more uniform synchronous field can be produced in the channel. We discuss the mechanism of forming a symmetric mode with a double grating. A method to design a double grating that can provide a quasi-symmetric accelerating mode with single-sided illumination will be introduced.

3.1.1 Accelerating mode of a double grating

In this part, we focus on the theory of how a symmetric accelerating field is formed in a double grating, leaving alone the excitation of the mode. Figure 3.1 shows a general double-grating structure consisting of a vacuum channel surrounded by two grating structures.

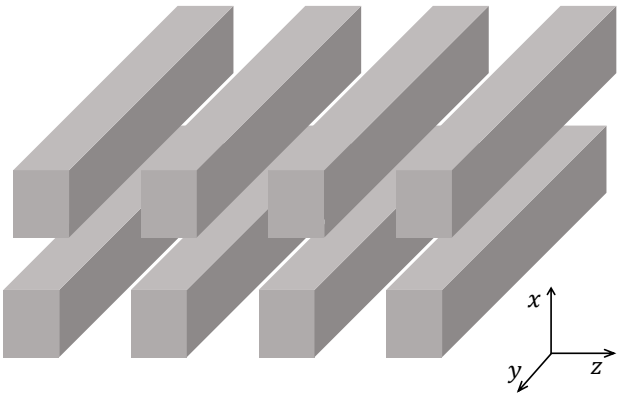

FIGURE 3.1: Schematic of a double grating for particle acceleration. Electrons travel in the channel between the two gratings. The channel width is d. $x = 0$ is located at the channel center.

We assume that, in a double grating, synchronous modes at the single gratings on either side of the channel have been excited. The profile of an accelerating mode from above can be given by

$$H_{y,s}(x,z) = -H_{\mathrm{u}}\mathrm{e}^{x/\Gamma}\mathrm{e}^{i(k_z z)},, \tag{3.1}$$

$$E_{x,s}(x,z) = -\frac{1}{\beta_{\mathrm{e}}}\sqrt{\frac{\mu_0}{\epsilon_0}}H_{\mathrm{u}}\mathrm{e}^{x/\Gamma}\mathrm{e}^{i(k_z z)},, \tag{3.2}$$

$$E_{z,s}(x,z) = -\frac{i}{\beta_{\mathrm{e}}\gamma_{\mathrm{e}}}\sqrt{\frac{\mu_0}{\epsilon_0}}H_{\mathrm{u}}\mathrm{e}^{x/\Gamma}\mathrm{e}^{i(k_z z)}, \tag{3.3}$$

where H_{u} is the amplitude of the magnetic field of the synchronous mode at a distance of $d/2$ from the grating surface, or at the channel center. The profile of the accelerating mode from below can be given by

$$H_{y,s}(x,z) = +H_{\mathrm{d}}\mathrm{e}^{-x/\Gamma}\mathrm{e}^{i(k_z z+\delta)}, \tag{3.4}$$

$$E_{x,s}(x,z) = +\frac{1}{\beta_{\mathrm{e}}}\sqrt{\frac{\mu_0}{\epsilon_0}}H_{\mathrm{d}}\mathrm{e}^{-x/\Gamma}\mathrm{e}^{i(k_z z+\delta)}, \tag{3.5}$$

$$E_{z,s}(x,z) = -\frac{i}{\beta_{\mathrm{e}}\gamma_{\mathrm{e}}}\sqrt{\frac{\mu_0}{\epsilon_0}}H_{\mathrm{d}}\mathrm{e}^{-x/\Gamma}\mathrm{e}^{i(k_z z+\delta)}, \tag{3.6}$$

where H_{d} is the amplitude of the magnetic field of the synchronous mode at a distance of $d/2$ from the grating surface, or at the channel center, δ is the phase difference between the mode from above and from below.

In the channel, the superposition of evanescent modes from either side can form different field patterns, depending on the relative phase difference of δ. If $\delta = 0$, the longitudinal electric field in the channel formed by the superposition of two evanescent fields take

the form of a cosh mode,

$$H_y(x,z) = -2\sqrt{H_\mathrm{u}H_\mathrm{d}}\sinh\left[\frac{x}{\Gamma}+\ln(\frac{H_\mathrm{u}}{H_\mathrm{d}})\right]\mathrm{e}^{\mathrm{i}(k_z z)}, \tag{3.7}$$

$$E_x(x,z) = -\frac{2\sqrt{H_\mathrm{u}H_\mathrm{d}}}{\beta_\mathrm{e}}\sqrt{\frac{\mu_0}{\epsilon_0}}\sinh\left[\frac{x}{\Gamma}+\ln(\frac{H_\mathrm{u}}{H_\mathrm{d}})\right]\mathrm{e}^{\mathrm{i}k_z z}, \tag{3.8}$$

$$E_z(x,z) = -\frac{\mathrm{i}2\sqrt{H_\mathrm{u}H_\mathrm{d}}}{\beta_\mathrm{e}\gamma_\mathrm{e}}\sqrt{\frac{\mu_0}{\epsilon_0}}\cosh\left[\frac{x}{\Gamma}+\ln(\frac{H_\mathrm{u}}{H_\mathrm{d}})\right]\mathrm{e}^{\mathrm{i}k_z z}. \tag{3.9}$$

The Lorentz force experienced by the synchronous particle in the channel can be given by

$$F(x,z,t)=\begin{bmatrix}F_x\\F_y\\F_z\end{bmatrix}=\begin{bmatrix}-\frac{2e\sqrt{H_\mathrm{u}H_\mathrm{d}}q}{\beta_\mathrm{e}\gamma_\mathrm{e}^2}\sqrt{\frac{\mu_0}{\epsilon_0}}\sinh\left[\frac{x}{\Gamma}+\ln(\frac{H_\mathrm{u}}{H_\mathrm{d}})\right]\mathrm{e}^{\mathrm{i}(k_z z-\omega t)},\\0\\-\frac{\mathrm{i}2e\sqrt{H_\mathrm{u}H_\mathrm{d}}}{\beta_\mathrm{e}\gamma_\mathrm{e}}\sqrt{\frac{\mu_0}{\epsilon_0}}\cosh\left[\frac{x}{\Gamma}+\ln(\frac{H_\mathrm{u}}{H_\mathrm{d}})\right]\mathrm{e}^{\mathrm{i}(k_z z-\omega t)}\end{bmatrix}. \tag{3.10}$$

It is apparent that only when the two evanescent modes are excited equally strong, i.e., $H_\mathrm{u}=H_\mathrm{d}=H_0$, the accelerating mode would be symmetric with respect to the channel center ($x=0$). In this case, the Lorentz force could be rewritten as

$$F(x,z,t)=\begin{bmatrix}F_x\\F_y\\F_z\end{bmatrix}=\begin{bmatrix}-\frac{2eH_0}{\beta_\mathrm{e}\gamma_\mathrm{e}^2}\sqrt{\frac{\mu_0}{\epsilon_0}}\sinh\left(\frac{x}{\Gamma}\right)\mathrm{e}^{\mathrm{i}(k_z z-\omega t)}\\0\\-\frac{\mathrm{i}2eH_0}{\beta_\mathrm{e}\gamma_\mathrm{e}}\sqrt{\frac{\mu_0}{\epsilon_0}}\cosh\left(\frac{x}{\Gamma}\right)\mathrm{e}^{\mathrm{i}(k_z z-\omega t)}\end{bmatrix} \tag{3.11}$$

The Lorentz force experienced by a particle in the double-grating structure is illustrated by Fig. 3.2. It can be seen that the accelerating field is rather uniform at the channel center, which is desirable for particle acceleration. On the axis where the acceleration reaches its minimum, the mode has vanishing deflection. There is a focusing or defocusing force towards the axis, depending on the phase of a particle in the optical cycle. It can also be seen that the acceleration and deflection are $\pi/2$ out of phase, indicating that longitudinal focusing of the beam results in transverse defocusing, and vice versa, which is in agreement with Earnshaw's theorem.

3.1.2 Resonant enhancement of accelerating mode

In this part, we discuss how to use a single laser to excite equally strong synchronous modes on either side of the channel, with their phase matched with each other.

As is discussed in Chapter 2, upon the incidence of a plane wave, a series of diffraction modes are excited at a single grating. The longitudinal electric field of the reflected nth

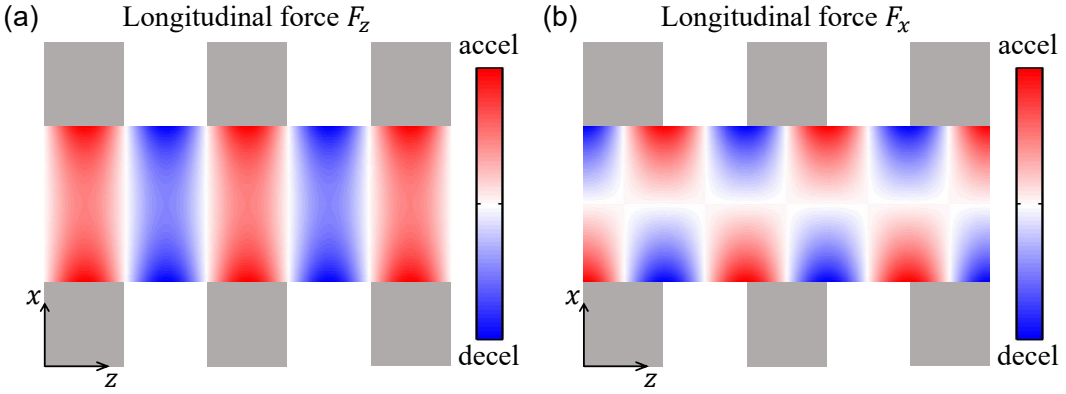

FIGURE 3.2: Illustration of the Lorentz force on the particle in a double grating.

diffraction order is given by:

$$E_{z,n} = |r_n| E_0 e^{i(k_{z,n}z + k_{x,n}x - \omega t + \psi_{R,n})}, \; x > 0, \tag{3.12}$$

where E_0 is the peak incident field, ω is the angular frequency, and $k_{x,n}$, r_n, and $\psi_{R,n}$ are the x wavenumber, reflection coefficient, and reflection phase of the nth order, respectively.

Among these modes, the synchronous mode and higher orders are evanescent modes, which can only exist close to the single grating. However, the zeroth diffraction order, which is a plane wave with a real x wavenumber, can propagate and carry energy. In a double grating with one-sided illumination, if not all of the optical power is reflected back at the first grating, in the transmission region there exists a propagating zeroth diffraction order. The arrival of this zeroth diffraction order at the opposite grating causes diffraction effect again, leading to the generation of a synchronous mode at the opposite grating.

In 2015, a double grating with a single-sided illumination was experimentally demonstrated[29]. To produce a cosh mode, a single grating, or a row of pillars, with low reflectivity was designed so that the incident laser can transmit to the second grating. An off-center cosh accelerating mode was produced because the excitation of the synchronous modes from each side was unequal.

The accelerating modes can also be excited by using two lasers from each side. In 2018, by using a symmetrically driven silicon dual pillar grating structure, the phase-dependent laser acceleration and deflection of electrons was demonstrated by controlling the relative phase of the laser at each sides[30]. Highly-reflective single grating was used to make sure the excitation of the synchronous mode on each side of the channel is governed by the incident laser from that respective side.

It is apparent that using dual-sided illumination increases the system complexity. Thus, we propose a method to produce a symmetric cosh mode in the channel with a single-sided illumination. The idea behind this method is to merge diffraction gratings with resonating Fabry-Perot cavities. To realize such a resonator, we make use of the high reflectivity feature of subwavelength gratings (SWGs) to resonant with the zeroth diffraction order (plane wave) in the channel, where the circulating plane wave in the channel serves to excite phase-matched synchronous modes on both sides. It not only simplifies the power delivery system but also enables a laser efficient acceleration due to the resonant enhancement of accelerating mode in the channel.

The high reflectivity feature of SWGs was discovered in 2004[51, 52]. After that, high-reflectivity SWGs have been applied as mirrors in a number of applications such as vertical-cavity surface-emitting lasers (VCSELs)[53, 54], Fabry-Perot resonators[55–57],

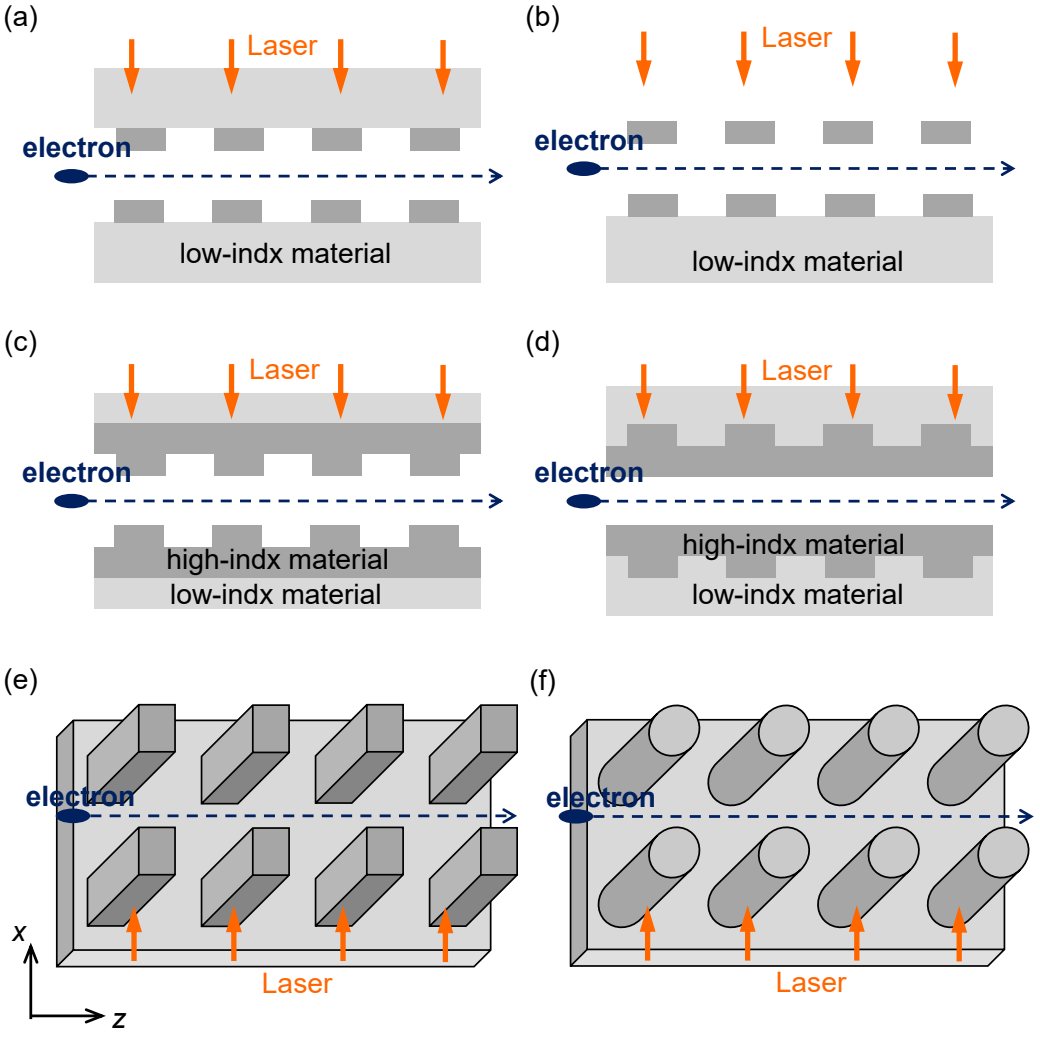

FIGURE 3.3: Different designs of double-grating structures. (a) High-contrast slab grating. (b) Asymmetric high-contrast grating. (c) Hybrid slab grating. (d) Inversed hybrid slab grating. (e) High-contrast rectangular pillar grating. (f) High-contrast elliptical pillar grating.

and hollow-core waveguides [58, 59]. To provide high reflectivity, we can use a high-contrast SWG that consists of an array of high-index bars with low-index materials[60], or a hybrid grating reflector or zero-contrast grating that consists of a sub-wavelength grating layer and an unpatterned layer[61]. In Fig. 3.3, we show several possible shapes of double-grating resonators. Among those structures, the difficulty in aligning the two pieces of single gratings in a double slab grating makes the fabrication rather difficult[62]. In contrast, the double pillar grating of silicon can be etched directly out of a wafer[48]. Besides, the pillar structure on a slab can be easily integrated with a laser delivery system[63]. Therefore, from the perspective of fabrication and integration, pillar grating structure would probably be a better choice.

In this work, we use the high-contrast rectangular pillar grating as an example to show how to design a double-grating resonator. The method can be generalized to other structures. Referring to [29, 30], we choose silicon material, which can provide a perfect platform for integration. As is apparent, It would be better if the silicon is transparent for the laser. Hence, we choose to use a laser wavelength of 1550 nm in the simulation. However, it is also possible to use the 1030 nm laser which is being developed at KEK for the experiment, since the absorption length of silicon at 1030 nm is much longer than the x dimension of the double pillar grating.

In the simulation, the laser is focused on the pillars so that we will neglect the effect of the substrate. Figure 3.4 shows the cross-section of the pillar structure. Electrons travel in the channel between two gratings. For simplicity, we use identical gratings on either side of the channel.

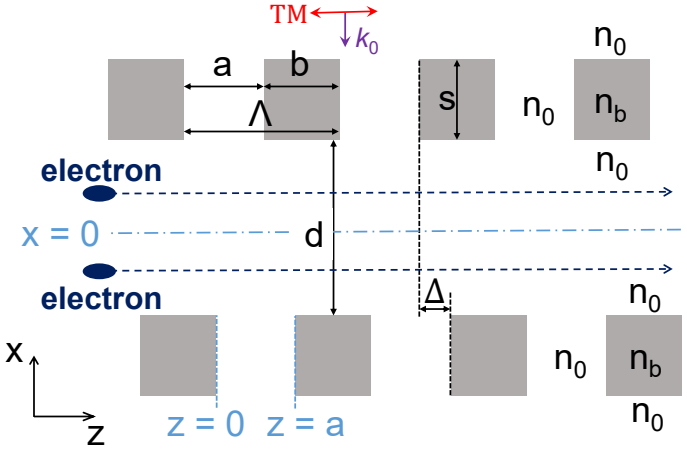

FIGURE 3.4: Cross section of the pillars in a high-contrast rectangular pillar grating. A periodic array of silicon bars with a high refractive index n_b surrounded by vacuum, compose a high-reflectivity mirror. Dimensions: d channel width; Δ, longitudinal offset between the two SWGs. $x = 0$ is located at the channel center.

When using high-reflectivity gratings as mirrors in a dual-grating resonator, the channel width d is determined by the round-trip phase condition for a plane wave:

$$\varphi = 2\psi_{\mathrm{R},0} + 2k_0 d = 2p\pi, \text{ with } p \text{ being an integer,} \tag{3.13}$$

where φ is the round-trip phase of the zeroth order. A circulating-field approach in the steady state is illustrated in Fig. 3.5[64], showing the fields for a plane wave incident on a Fabry-Perot cavity with mirror reflectivity R and reflection phase $\psi_{\mathrm{R},0}$. In Fig. 3.5, indicated are the electric fields (black) and phase shifts (red): incident field, E_{i}; propagating backward, E_{r}; transmitted through the cavity, E_{t}; circulating downward and upward between the mirrors, E_{c} and E_{b}, respectively; phase accumulated through the channel, $k_0 d$.

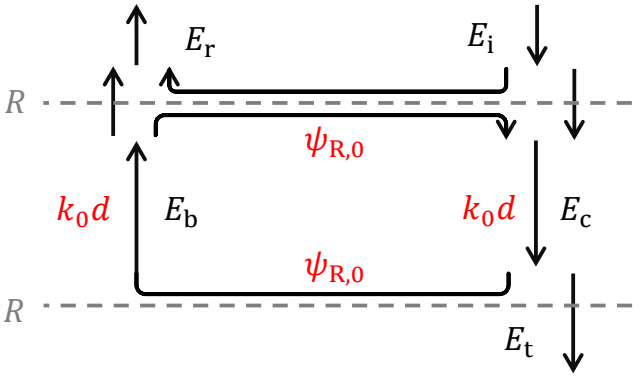

FIGURE 3.5: The field approach of a plane wave in a Fabry-Perot cavity with mirror reflectivity R and reflection phase $\psi_{\mathrm{R},0}$. The electric fields (black) and phase shifts (red) are indicated,incident field E_{i}, E_{r} propagating backward, E_t transmitted through the cavity, E_{c} and E_{b} circulating downward and upward between the mirrors, respectively, and phase $k_0 d$ accumulated through the channel.

At the resonant angular frequency ω, the enhancement factor A_{c} is defined as the ratio of the circulating field E_{c} propagating downward inside the channel to the incident field E_{i},

$$A_{\mathrm{c}} = \frac{E_{\mathrm{c}}}{E_{\mathrm{i}}} = \frac{1}{\sqrt{1-R}}. \tag{3.14}$$

In such a resonator, the circulating field propagating upward E_{b} is related to E_{c} by $E_{\mathrm{b}} = RE_{\mathrm{c}}$. With a high reflectivity, $R \approx 1$, we have $E_{\mathrm{b}} \approx E_{\mathrm{c}}$. Inside the channel, besides the evanescent modes excited by E_{i}, there are evanescent modes excited by E_{c} and E_{b} on either side of the channel. If the enhancement factor A_{c} is high, the evanescent fields excited by E_{c} and E_{b} will be much stronger than that by E_{i}. In this case, the accelerating mode is governed by a cosh accelerating mode formed by the superposition of evanescent modes excited by E_{c} and E_{b}, as shown by Eq. 3.9. The Lorentz force

experienced by an electron is given by

$$F = \begin{bmatrix} F_x \\ F_y \\ F_z \end{bmatrix} \approx \begin{bmatrix} -2A_c r_1/\gamma_e e E_0 \mathrm{e}^{-d/(2\Gamma)} \sinh(x/\Gamma)\cos\phi \\ 0 \\ 2A_c r_1 e E_0 e^{-d/(2\Gamma)} \cosh(x/\Gamma)\sin\phi \end{bmatrix}. \tag{3.15}$$

Here, $\gamma_e = (1-\beta_e^2)^{-1/2}$ is the Lorentz factor of electrons, $\Gamma = \beta_e\gamma_e\lambda/(2\pi)$ is the decay constant of the evanescent mode, and $\phi = k_{z,1}z - \omega(t-t_0) - \phi_0$ is the phase of electron in the optical cycle.

The relative phase of the synchronous modes on either side of the channel is determined by the round-trip phase φ. When $p = 0, \pm2, \pm4, \ldots$, the evanescent fields are in phase, forming a cosh mode in the channel. When $p = \pm1, \pm3, \ldots$, the evanescent fields are π out of phase, forming a sinh mode in the channel. In the latter case, the evanescent fields on each side can be synchronized to form a cosh mode by applying a longitudinal offset $\Delta = \Lambda/2$ to the lower grating (see Fig. 3.4). As discussed in Sec. 3.1.1, this mode has a net accelerating force at the channel center and phase-dependent focusing force directed towards the channel center.

When the reflectivity of the grating is not high enough, the enhancement factor A_c becomes low such that the synchronous mode excited at the upper grating by the incident field E_i cannot be neglected, an off-center cosh mode is produced.

When the grating has a high reflectivity but the round-trip phase condition is not satisfied, only the upper grating can be excited, the field in the channel resembles that of a single grating.

3.2 Simulation of a resonant double grating

In this section, we use several examples to show how to design a resonant double grating for dielectric laser acceleration. We investigate the reflectivity of a single grating and use it as mirrors in the resonator. We show how the performance of the resonator can be controlled.

3.2.1 High-reflectivity grating design

To begin with, we will explore the dependence of reflectivity and reflection phase on the SWG dimensions to show the extraordinary characteristics provided by the resonator.

The reflection of a plane wave at an SWG can be intuitively understood by using the waveguide-array (WGA) modes formalism published by Chang-Hasnain and co-workers[60, 65]. Figure 3.6 shows the cross-section of a generic pillar single-grating structure. Along the x-direction, we treat an SWG as a periodic array of waveguides. One or more WGA modes that are excited by the incident plane wave can propagate inside the grating. Here we will derive the dispersion relation for the WGA modes. To get a generic solution which can also be applied for the other structures in Fig. 3.3, we assume the refractive indices for the grating gap, the grating pillar, and the incident media are n_{a}, n_{b} and n_{I}, respectively, as shown in Fig. 2.2.

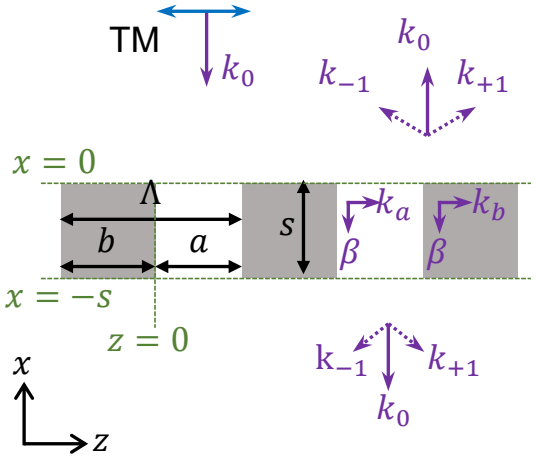

FIGURE 3.6: Cross section of a single grating and the wavenumbers. It consists a periodic array of silicon bars with refractive index n_{b}, surrounded by materials with refractive index n_{a} in the grating gaps, n_1 in the reflection region, and n_2 in the transmission region, comprise a phase mask. The grating is assumed to be infinite in y direction and infinitely periodic in z direction.

With k_0 being the wavenumber in free space and $\varepsilon(z)$ being the profile of permittivity in the grating, the eigenvalue equation is given by

$$\frac{d^2 H_y}{dz^2} + [k_0^2 \varepsilon(z) - k_x^2] H_y = 0. \tag{3.16}$$

The solution of the field $H_{y,m}(z)$ can be written as

$$H_y(z) = A^+ \mathrm{e}^{\mathrm{i}k_{\mathrm{a}}z} + A^- \mathrm{e}^{-\mathrm{i}k_{\mathrm{a}}z}, \qquad 0 < z < a, \tag{3.17}$$

$$H_y(z) = B^+ \mathrm{e}^{\mathrm{i}k_{\mathrm{b}}z} + B^- \mathrm{e}^{-\mathrm{i}k_{\mathrm{b}}z}, \qquad a < z < \Lambda, \tag{3.18}$$

where the z wavenumber k_{a} for the gap and and the z wavenumber k_{b} for the bar are determined by

$$k_{\mathrm{a}}^2 = n_{\mathrm{a}}^2 k_0^2 - k_x^2, \qquad 0 < z < a, \tag{3.19}$$

$$k_{\mathrm{b}}^2 = n_{\mathrm{b}}^2 k_0^2 - k_x^2, \qquad a < z < \Lambda. \tag{3.20}$$

Enforcing the continuity of tangential electric and magnetic field at the bar-gap interfaces

$$H_y(a^-) = H_y(a^+), \tag{3.21}$$
$$E_x(a^-) = E_x(a^+), \tag{3.22}$$
$$H_y(\Lambda^-) = H_y(\Lambda^+), \tag{3.23}$$
$$E_x(\Lambda^-) = E_x(\Lambda^+), \tag{3.24}$$

and the Bloch periodic boundary condition

$$H_y(z+\Lambda) = H_y(z)\mathrm{e}^{\mathrm{i}n_\mathrm{I}k_0\sin(\theta)\Lambda}, \tag{3.25}$$

yields

$$A^+\mathrm{e}^{\mathrm{i}k_\mathrm{a}a} + A^-\mathrm{e}^{-\mathrm{i}k_\mathrm{a}a} = B^+\mathrm{e}^{\mathrm{i}k_\mathrm{b}a} + B^-\mathrm{e}^{-\mathrm{i}k_\mathrm{b}a}, \tag{3.26}$$
$$\frac{k_\mathrm{a}}{n_\mathrm{a}^2}\left(A^+\mathrm{e}^{\mathrm{i}k_\mathrm{a}a} - A^-\mathrm{e}^{-\mathrm{i}k_\mathrm{a}a}\right) = \frac{k_\mathrm{b}}{n_\mathrm{b}^2}\left(B^+\mathrm{e}^{\mathrm{i}k_\mathrm{b}a} - B^-\mathrm{e}^{-\mathrm{i}k_\mathrm{b}a}\right), \tag{3.27}$$
$$\mathrm{e}^{\mathrm{i}n_\mathrm{I}k_0\sin(\theta)\Lambda}(A^+ + A^-) = B^+\mathrm{e}^{\mathrm{i}k_\mathrm{b}\Lambda} + B^-\mathrm{e}^{-\mathrm{i}k_\mathrm{b}\Lambda}, \tag{3.28}$$
$$\frac{k_\mathrm{a}}{n_\mathrm{a}^2}\mathrm{e}^{\mathrm{i}n_\mathrm{I}k_0\sin(\theta)\Lambda}(A^+ - A^-) = \frac{k_\mathrm{b}}{n_\mathrm{b}^2}\left(B^+\mathrm{e}^{\mathrm{i}k_\mathrm{b}\Lambda} - B^-\mathrm{e}^{-\mathrm{i}k_\mathrm{b}\Lambda}\right). \tag{3.29}$$

Based on Eqs, [3.26-3.29], the dispersion relations for the WGA modes of an SWG can be obtained,

$$\begin{aligned} &2n_\mathrm{a}^2n_\mathrm{b}^2k_\mathrm{a}k_\mathrm{b}[\cos(k_\mathrm{a}a)\cos(k_\mathrm{b}b) - \cos(n_\mathrm{I}k_0\sin(\theta)\Lambda)] \\ &\quad = (n_\mathrm{b}^4k_\mathrm{a}^2 + n_\mathrm{a}^4k_\mathrm{b}^2)\sin(k_\mathrm{a}a)\sin(k_\mathrm{b}b). \end{aligned} \tag{3.30}$$

For the pillar single-grating and wave vectors as shown in Fig. 3.6, $n_\mathrm{a} = n_\mathrm{I} = 1$, and the dispersion relationship can be rewritten as

$$k_\mathrm{b}\tan(k_\mathrm{b}b/2) = -n_\mathrm{b}^2k_\mathrm{a}\tan(k_\mathrm{a}a/2). \tag{3.31}$$

In Fig. 3.7, we show the dispersion curves of WGA modes in SWGs with different duty cycle b/Λ. With a surface-normal incidence, we cannot excite the odd modes ($\mathrm{TM}_{1,3,5,\ldots}$) since the incident plane wave has a constant profile in the z direction. In the figure, we show the cutoff frequency ω_{cn} of the nth-order WGA mode with a duty cycle of $b/\Lambda = 0.6$. It is shown that the WGA mode dispersion curves shift in response to the variation of b/Λ.

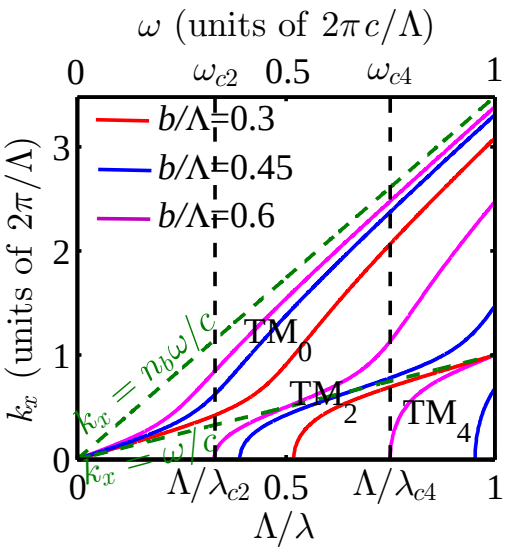

FIGURE 3.7: Dispersion curves of WGA modes in an SWG with duty cycles of 0.3, 0.45 and 0.6. Silicon is used as the bar material.

In a single grating with finite thickness s, the WGA modes are confined in the grating by the grating boundaries in the x direction and thus forms a cavity with coupling to the diffraction modes outside the grating. The interference of the WGA modes at the grating boundaries, which depends on the phases accumulated by the WGA modes through the waveguide array, determines the reflection of an SWG. In Fig. 3.8(a) and Fig. 3.8(b), we visualize the effect of the grating thickness t on the reflection using the $t-\Lambda/\lambda$ (i.e., ω in units of $2\pi c/\Lambda$) maps of the reflectivity and phase, with $b/\Lambda = 0.6$. The different reflectivity patterns in different wavelength regions reveal a strong dependence of the dispersion relation on the wavelength, as shown in Fig. 3.7. In the dual-mode region ($\omega_{c2} < \omega < \omega_{c4}$), an ordered checkerboard pattern was formed as the result of the interference of two WGA modes at the grating boundaries. When there is a destructive interference at the exit boundary $x = -t$, high reflectivity is obtained, e.g., the regions marked by the white circles in Fig. 3.8(a). On the other hand, when there is a constructive interference at both the input and exit boundaries, a high-Q resonator with strong fields in the dielectric is formed, which is undesirable for our purpose, e.g., the regions marked by the black circles.

Significant shifts of the reflectivity and phase patterns in the $t/\Lambda-\Lambda/\lambda$ maps is caused by the shifts of the mode dispersion due to the variation in duty cycle as shown in Fig. 3.7, enabling the resonator scalability to different values of Λ/λ, or different electron energies. Figs. 3.8[(c)–(d)] show the reflectivity and reflection phase with $b/\Lambda = 0.3$, respectively. Comparing with Fig. 3.8[(a)–(b)] with $b/\Lambda = 0.6$, a smaller duty cycle corresponds to shifting the high-reflectivity regions towards larger Λ/λ, which is consistent with the shift of the cutoff frequencies in Fig. 3.7. For electrons with lower energies (e.g., 10 keV), the

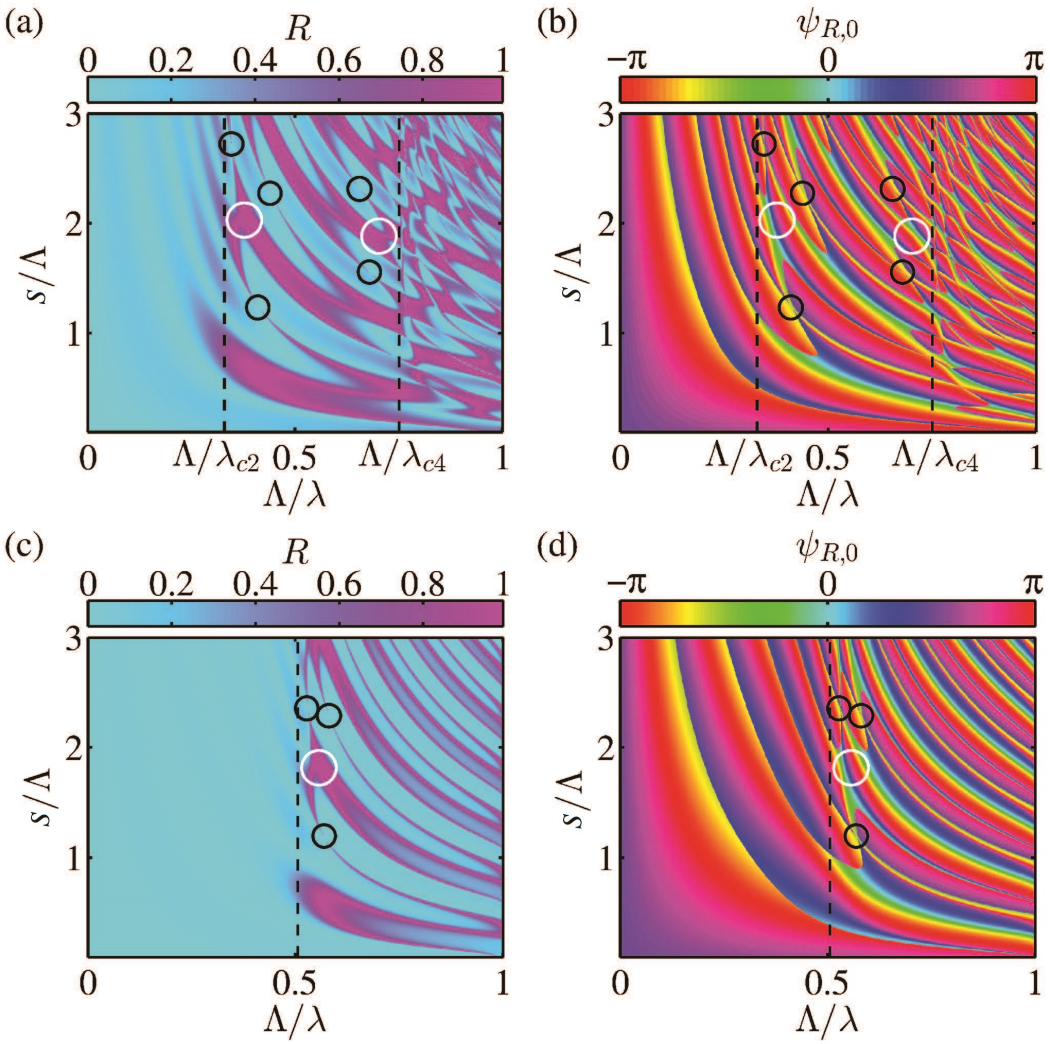

FIGURE 3.8: $t/\Lambda - \Lambda/\lambda$ maps of the reflectivity [(a) and (c)] and reflection phase [(b) and (d)], with duty cycles of $b/\Lambda = 0.6$ [(a) and (b)] and $b/\Lambda = 0.3$ [(c) and (d)]. The cutoff frequencies of the WGA modes obtained in Fig. 3.7 are shown by the black dashed lines. Some of the high-reflectivity regions useful for DLA are marked by the white circles. Some of the unfavorable high-Q resonant points are marked by the black circles.

grating period required by the synchronicity condition becomes too small. In this case, higher diffraction orders ($n > 1$) that requires a larger grating period can be used for acceleration [20, 25].

3.2.2 Enhanced accelerating mode of a double grating

In this part, we show how to design a double-grating resonator for given electron energy. For electron energy of 50 keV and a laser wavelength of 1550 nm, the grating period is determined by the synchronicity condition to be 640 nm. Figure 3.9(a) shows that when $b/\Lambda > 0.41$, there are two propagating WGA modes. In the dual-mode region, the interference of propagating WGA modes leads to highly ordered reflectivity and

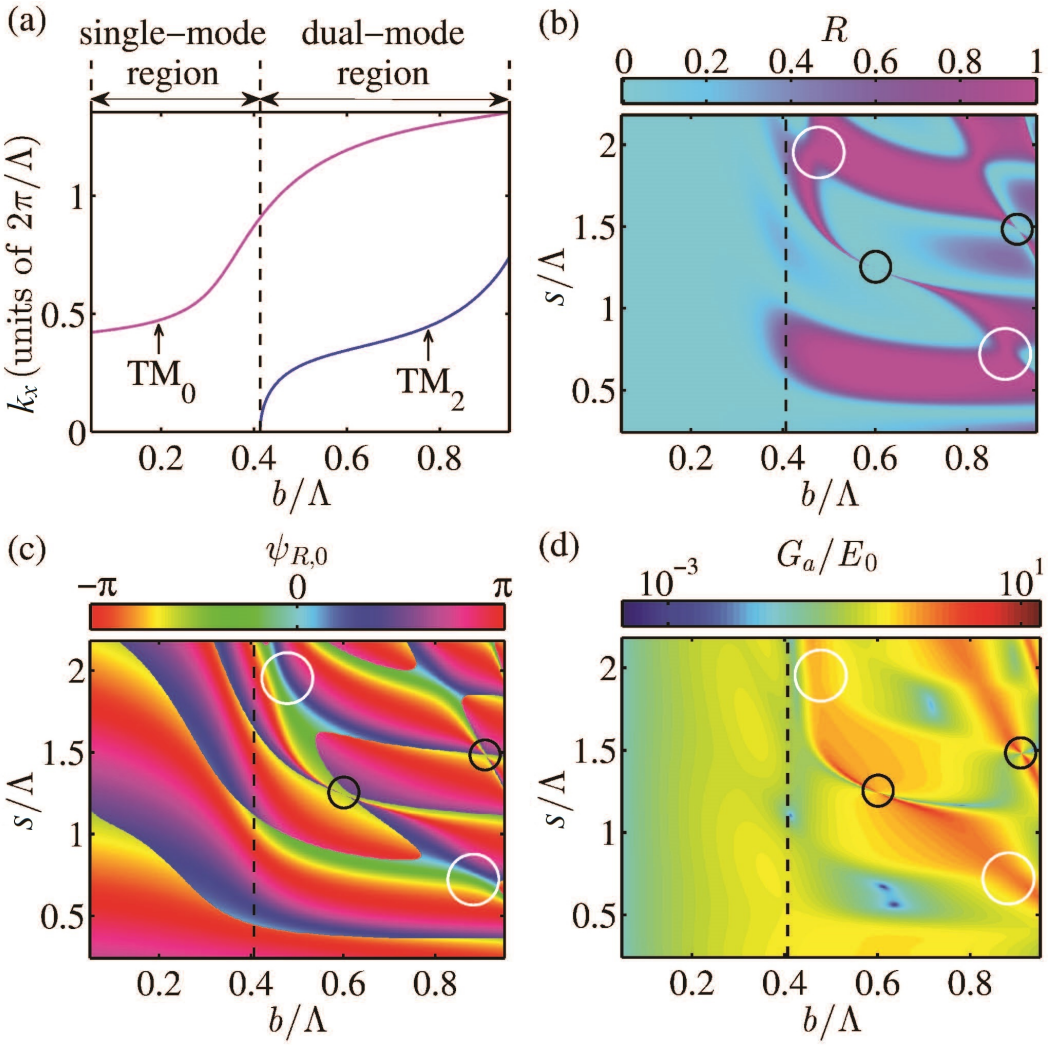

FIGURE 3.9: x wavenumber of WGA modes as a function of b/Λ (a) and $s-b$ maps of reflectivity R (b), reflection phase $\psi_{\mathrm{R},0}$ (c), and reflected gradient at the grating surface G_a/E_0 (d). The boundary between the single- and dual-mode regions, which correspond to the ranges of b/Λ with one and two propagating WGA modes, respectively, is indicated by the black dashed line. White circles indicate some of the high-reflectivity regions useful for DLA, while black circles indicate some of the undesirable high-reflectivity regions with high-Q resonance in the grating. Parameters: $\Lambda = 640$ nm, $\lambda = 1550$ nm.

reflection phase patterns, as shown in Fig. 3.9(b) and Fig. 3.9(c), respectively. The $s-b$ map of the reflection coefficient of the first diffraction mode, r_1, which represents the normalized gradient G_a/E_0 at the grating surface ($x = 0$ in Fig. 3.6), is shown in Fig. 3.9(d). The points with ultra-high gradients correspond to the high-Q resonances in SWGs, which is not desirable for our purpose.

In Fig. 3.9(b), we show the $s-b$ map of SWG reflectivity, which ranges from zero to near unity and enables the control of the enhancement factor and filling time of the resonator. The damage threshold of dielectric materials is higher for ultrashort exposure times to strong fields [22]. In a Fabry-Perot resonator, the exposure time depends on the

cavity filling time $t_{fill} = Q/\omega$, where the quality factor can be approximately calculated by $Q = -k_0 d/\ln(R)$[64]. In Eq. 3.14, it is suggested that a high enhancement factor can be obtained with high reflectivity. However, the filling time also increases with the reflectivity, requiring a longer pulse duration. Therefore, we need a trade-off between the enhancement factor and the achievable accelerating gradient when choosing the reflectivity. In order to sustain a high accelerating gradient, a relatively low reflectivity that enables a low enhancement factor but an ultrashort filling time is desirable. For a given reflectivity, Eq. 3.13 shows that the channel width d is determined by the reflection phase. In Eq. 3.10, it is shown that a smaller channel enables a higher gradient at channel center (see Eq. 3.10) and a reduced filling time. Despite the association of permitted charge with the channel width, a small channel width would be desirable for a high gradient.

In the following, we use eight examples of SWGs, with different reflection phases but identical reflectivities $R = 0.997$, as mirrors in the cavity simulation. In the simulation, we found it took too much time to reach a steady state in CST MWS. Thus, we developed our code using rigorous coupled-wave analysis (RCWA)[66], which is depicted in the Appendix A. The dimensions of these SWGs are located in the vicinity of the uppermost white circle in Figs. 3.9[(b)–(d)]. In Table 3.1, we summarize the parameters for the eight examples of SWGs.

Table 3.1: Parameters of SWG1–8.

	b (nm)	t (nm)	R	$\psi_{R,0}$
SWG1	341	1318	0.997	-3.14
SWG2	288	1217	0.997	-1.59
SWG3	293	1231	0.997	-0.79
SWG4	296	1238	0.997	-0.39
SWG5	298	1243	0.997	0.00
SWG6	322	1225	0.997	1.57
SWG7	350	1208	0.997	2.36
SWG8	376	1194	0.997	2.74

For each SWG, we investigate resonators with two different round-trip phases (φ) which enable Fabry-Perot resonance. We also analytically calculate the parameters with the theory in Sec. 3.1.2. In Fig. 3.10, we compare the analytical results with the RCWA simulation results. The channel widths calculated analytically with Eq. 3.13 are presented by the solid black lines. The enhancement factor $A_c = 18.3$ obtained analytically with Eq. 3.14 is presented by the width of the shades. The crosses and widths of the bars represent the two resonant channel widths d that enable resonance with different round-trip phases φ and the corresponding enhancement factors calculated with RCWA

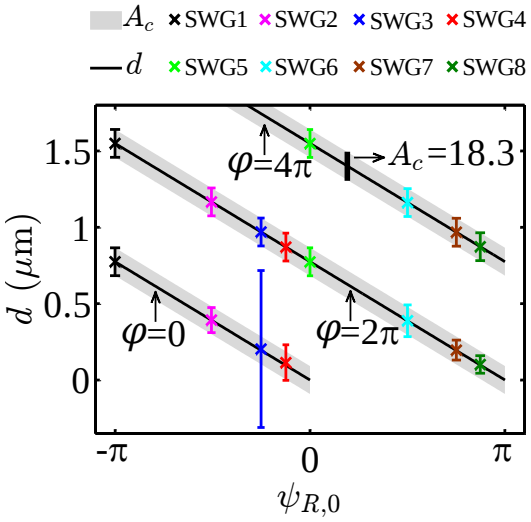

FIGURE 3.10: Comparison of resonant channel widths d and enhancement factors A_c calculated by analytical solution and RCWA, using SWGs as show in Table 3.1 as the mirrors. The black solid lines represent the channel widths calculated analytically with Eq. 3.13. The width of the shades represents the enhancement factor calculated analytically with Eq. 3.14. The width corresponding to $A_c = 18.3$ is indicated. For each SWG, two resonant channel widths d that enable resonance with different round-trip phases ϕ calculated by RCWA and the corresponding enhancement factors are shown by the crosses and widths of the bars, respectively. The parameters of the SWGs and SWG-SWG resonator ($\varphi = 0$) are listed in Table 3.1 and Table 3.2, respectively; $\Lambda = 640$ nm, $\lambda = 1550$ nm.

TABLE 3.2: Parameters of SWG-SWG resonators as shown in Fig. 3.10.

	ϕ	d_0 (nm)	$A_{c,0}$	$t_{fill,0}$ (ps)	$d_0{}'$	$A_{c,0}{}'$	$t_{fill,0}{}'$ (ps)
SWG1-SWG1	0	775	18.3	0.86	775	18.3	0.86
	2π	1550	18.3	1.72	1550	18.2	1.72
SWG2-SWG2	0	392	18.3	0.43	393	16.4	0.35
	2π	1167	18.3	1.30	1167	18.3	1.29
SWG3-SWG3	0	195	18.3	0.22	203	102.8	7.16
	2π	970	18.3	1.08	970	18.3	1.08
SWG4-SWG4	0	96	18.3	0.11	114	23.3	0.21
	2π	871	18.3	0.97	871	18.3	0.97
SWG5-SWG5	2π	774	18.3	0.86	774	18.4	0.87
	4π	1549	18.3	1.72	1549	18.3	1.72
SWG6-SWG6	2π	387	18.3	0.43	388	20.8	0.56
	4π	1162	18.3	1.29	1162	18.2	1.29
SWG7-SWG7	2π	193	18.3	0.21	196	13.1	0.11
	4π	968	18.3	1.07	968	18.2	1.07
SWG8-SWG8	2π	98	18.3	0.11	102	11.5	0.04
	4π	873	18.3	0.97	873	18.2	0.97

for each SWG, respectively. The parameters are listed in Table 3.2, where d_0, $A_{c,0}$, and $t_{fill,0}$ represent the round-trip phase, enhancement factor, and filling time calculated analytically, respectively, and $d_0{}'$, $A_{c,0}{}'$, and $t_{fill,0}{}'$ correspond to the results obtained by the RCWA simulation.

Figure 3.10 shows that, when the channel is large, the simulation results are in agreement with the analytical solution, while when the channel is small, there are differences in both the resonant channel width and enhancement factor; the latter can be more clearly seen. We infer that the discrepancy arises from an effect that is not considered in the analytical solution, referred as evanescent wave coupling, or tunneling: with a small channel, the evanescent fields at one grating could arrive at the opposite grating and excite WGA modes before vanishing, thereby changing the resonator parameters. In Fig. 3.10, it is shown that the variation in enhancement factor is more significant. The reason is, a small change in reflection phase leads to a slight variation in channel width, but a small change in reflectivity could cause a significant variation in enhancement factor. For instance, a variation of the reflection phase by 5° leads to a variation of the resonant channel width by only 21.5 nm, which is relatively small compared to the large channel width in the simulation. However, a variation of the reflectivity from 0.997 to 0.999 leads to a variation of the enhancement factor from 18.3 to 31.6. When the reflectivity approaches 1, the enhancement factor increases more dramatically, e.g., a reflectivity of ~ 0.9999 corresponds to an enhancement factor of ~ 100, which is the case for the SWG3-SWG3 cavity ($\phi = 0$). In this case, to obtain a smaller enhancement factor, e.g., $A_c = 18.3$, one could use an SWG with lower reflectivity.

In a double-grating resonator, the fields in the channel and dielectric are enhanced, depending on the enhancement factor. In Fig. 3.12, we show the longitudinal field in the SWG2-SWG2 cavity ($\phi = 0$). The field modulation in the channel is a result of the superposition of the resonant zeroth diffraction order and higher orders.

Figure 3.12(a) shows the field ratio G_a/E_0 in the channels of the SWG-SWG resonators. The resonators have an enhanced accelerating mode in the channel, leading to a high accelerating gradient. To obtain a given accelerating gradient without damage, a higher enhancement factor can be chosen, allowing significantly reducing the input laser power. However, the highest sustainable accelerating gradient is limited by the damage threshold; thus, the ratio $G_\mathrm{a}/E_\mathrm{max}$ as shown in Fig. 3.12(d) is an important metric, with E'_max being the maximum field in the dielectric. In order to sustain a higher accelerating gradient, a maximum ratio $G_\mathrm{a}/E'_\mathrm{max}$ should be chosen. In the case of a small channel, the effect of the evanescent fields on the enhancement factor and channel width still applies here, leading to higher values of G_a/E_0 at the grating surface in the channel. Note that, in Chapter 3 and Chapter 4, we calculate the damage threshold in terms of

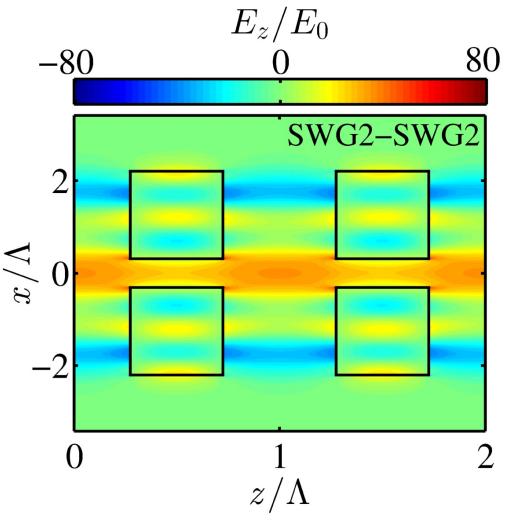

FIGURE 3.11: The ratio of the longitudinal electric field E_z to the peak incident field E_0 of an SWG2-SWG2 cavity with $\varphi = 0$. The parameters of the SWG2 and SWG2-SWG2 resonator ($\varphi = 0$) are shown in Table 3.1 and Table 3.2, respectively; $\Lambda = 640$ nm, $\lambda = 1550$ nm.

the maximum field in the material $E'_{\max}$, but not the maximum in-vacuum field at the grating surface $E_{\max}$, because the maximum field may not be located in the vacuum, e.g., for the structure as shown in Fig. 3.3(d). The procedure to calculate the sustainable accelerating gradient is also different accordingly.

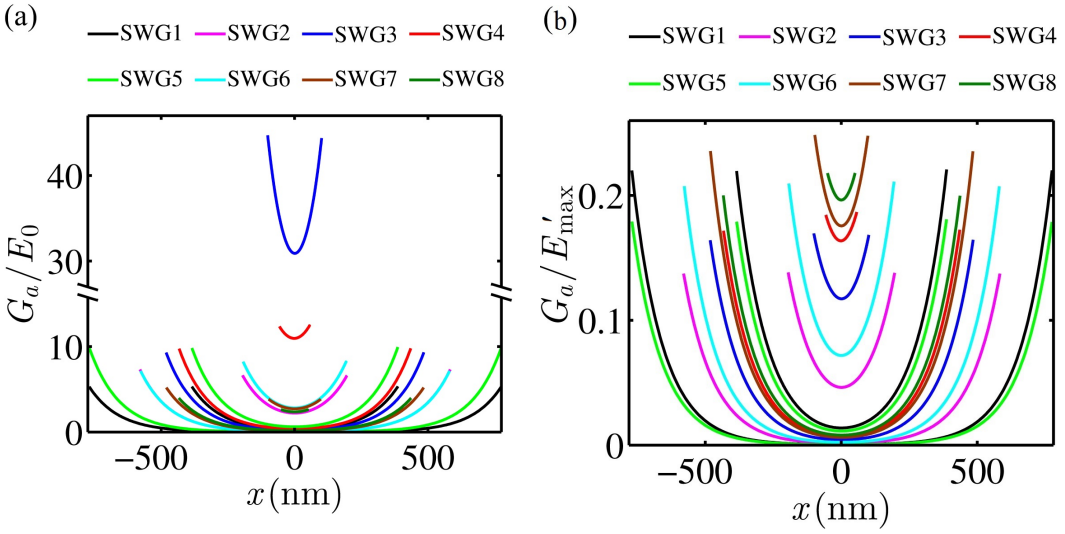

FIGURE 3.12: Accelerating gradients in the double-grating resonators. (a) The ratio of the accelerating gradient G_a to the peak incident field E_0 as a function of position in the channel. (b) The ratio of the accelerating gradient G_a to the maximum field in the dielectric $E'_{\max}$ as a function of position in the channel. The parameters of the SWGs and SWG-SWG resonators are shown in Table 3.1 and Table 3.2, respectively; $\Lambda = 640$ nm, $\lambda = 1550$ nm.

With these simulation results in hand, we can estimate the performance of those resonators, which is presented in the next section.

3.3 Performance of a resonant double grating

As an example, we will calculate the sustainable accelerating gradient and optical-to-beam efficiency of the SWG8-SWG8 resonator ($\phi = 2\pi$), which has a channel width $d = 102$ nm, enhancement factor $A_c = 11.5$, filling time $t_{fill} = 0.04$ ps, and field ratio $G_{\rm a}/E'_{\rm max} = 0.196$ at the channel center.

3.3.1 Accelerating gradient and energy gain

To calculate the sustainable accelerating gradient, we consider a damage threshold fluence of 0.2 J/cm^2 in the material. Assuming a Gaussian pulse in the material, the peak field E_0 is related to the fluence $F_{\rm in}$ by

$$E_0 = \sqrt{0.94\frac{2F_{\rm in}}{c\varepsilon_0 n_{\rm b}\tau_{\rm p}}}. \tag{3.32}$$

With a full width at half maximum laser pulse length $\tau_p = 0.18$ ps, the maximum electric field in the material without damage is calculated to be 1.5 GV/m. The corresponding highest gradient at the channel center is 0.30 GV/m. Due to the enhancement factor, the input laser power is reduced to 0.76% of that needed in a non-resonant structure.

By using the particle tracking method presented in Section. 2.3.1, we can estimate the energy gain of electrons launched at different start phase and x position in the channel. In the simulation, we assume a Gaussian laser pulse with a beam waist of 5 μm, and a grating structure with a total length $W = 10$ μm, corresponding to $\sim$ 16 periods

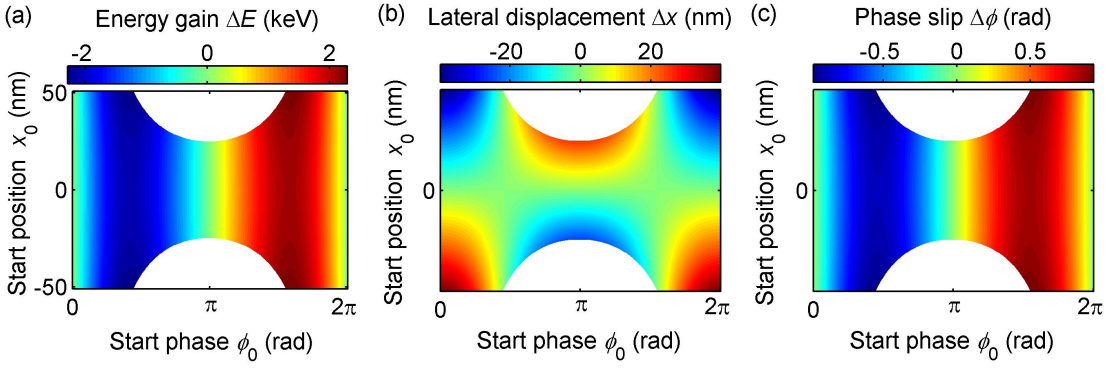

FIGURE 3.13: Particle tracking results for an SWG8-SWG8 double-grating structure. The electrons with an initial energy of 50 keV are launched at different start phases and initial distances from the grating surface. The colored maps show the energy gain ΔE (a), the deflected x displacement Δd (b), and the phase slip of the electrons in the accelerating mode $\Delta\phi$ (c). The white areas represent those electrons crashed into the grating structures. The structure with a grating period $\Lambda = 640$ nm and total width $W = 10$ μm is illuminated by a laser with wavelength $\lambda = 1550$ nm, laser beam waist radius $w_0 = 5$ μm, in-material fluence $F_{\rm th} = 0.2$ J/cm^2 and pulse duration $\tau_{\rm p} = 0.18$ ps.

of grating. Figure 3.13 shows the particle tracking results for 50 keV electrons in the channel as a function of the start phase ϕ_0 and initial x position, including the energy gain(a), the x displacement (b) and the phase slip (c). The white areas represent those electrons crashed into the grating structures. The characteristics of cosh accelerating field profile lead to a rather uniform energy gain around channel center, which is desirable for our purpose. There is a phase-dependent focusing or defocusing force towards the channel center. It can also be seen that with such an accelerating mode, operation with a longitudinal focusing leads to a transverse defocusing, which is in agreement with Earnshaw's theorem [67]. To stably accelerate an electron beam, external focusing component is needed. The maximum energy gain at the channel center is ~ 2.1 keV.

In Fig. 3.14 we show the instantaneous parameters of one electron launched at the channel center at an initial phase of 4.89 rad as a function of z position, including the kinetic energy E_k, the acceleration gradient G_a and the phase of electron in the optical cycle ϕ. The lateral displacement of the electron is zero due to the vanishing deflection at channel center. It is shown that the dephasing effect could be so severe that the electron is decelerated after initial acceleration, i.e., the electron moves from the acceleration phase to the deceleration phase. By adjusting the grating period according to electron energy variations, the dephasing problem could be alleviated, and a higher energy gain could be obtained.

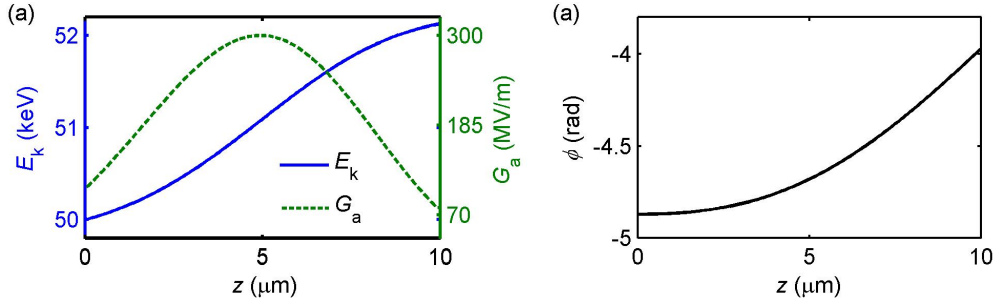

FIGURE 3.14: Instantaneous electron parameters as a function of z position. We show the instantaneous kinetic energy E_k [blue curves in (a)], the acceleration gradient G_a [green curves in (a)], and the phase of electron in the optical cycle (b). The structure with a grating period $\Lambda = 640$ nm and total width $W = 10$ μm is illuminated by a laser with wavelength $\lambda = 1550$ nm, laser beam waist radius $w_0 = 5$ μm, in-material fluence $F_\mathrm{th} = 0.2$ J/cm^2 and pulse duration $\tau_\mathrm{p} = 0.18$ ps. A 50 keV electron is launched at the channel center ($x_0 = 0$), at a start phase of 1.55 rad.

To further study the performance, we assume a Gaussian electron beam profile in the x direction, with a beam waist of 20 nm and the beam center being $x_0 = 0$ nm. The density in electron bunch is set to be temporally constant, and the pulse duration is one optical cycle. The electron beam energy spread and beam divergence are neglected.

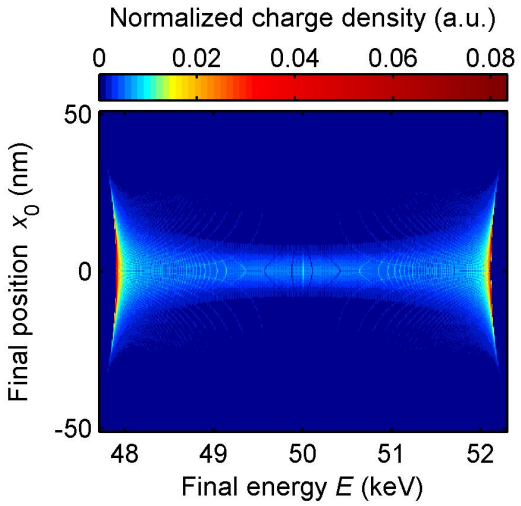

FIGURE 3.15: Charge density as a function of x position and energy E after interaction in a double grating.

In Fig. 3.15, the charge density as a function of x position and energy E after interaction in the double grating is shown. The survived electrons exist close to the beam axis. The double grating leads to much smaller energy spread than single grating.

In Figure. 2.15(a), the normalized charge densities as a function of x position before and after the interaction are shown. Over 98% of the electrons can survive after the interaction. The acceleration around the channel center is rather uniform. In addition, the proportion of the electrons around the channel center becomes higher after interaction, which is the result of sinh focusing field. In Figure. 2.15(b), the charge density as a function of energy is shown. There are two distinct charge peaks after the interaction, with energies of 57.9 keV and 52.1 keV, respectively.

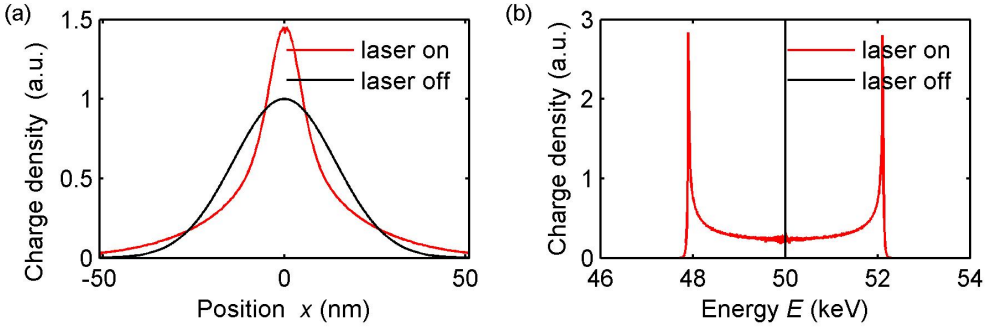

FIGURE 3.16: Charge density as a function of x position (a) and energy (b) before and after the interaction in a double grating.

3.3.2 Laser-to-electron efficiency

The laser-to-electron efficiency is another figure of merit for high energy physics. Here we will use a simple analytical treatment based on energy balance considerations proposed by Plettner and co-workers[68] to calculate the efficiency.

Assuming a flat-top laser beam profile with a dimension of D in the y direction, the laser power P_l over one grating period is

$$P_\mathrm{l} = \frac{E_0^2 \Lambda D}{2Z_0} \tag{3.33}$$

where $Z_0 = \sqrt{\mu_0/\epsilon_0}$ is the vacuum impedance.

The unloaded gradient G_a is related to the laser power P_l by the structure impedance defined as

$$Z_\mathrm{S} = \frac{|G_\mathrm{a}\Lambda|^2}{P_\mathrm{l}} = \left|\frac{G_\mathrm{a}}{E_0}\right|^2 \frac{2\Lambda Z_0}{D} \tag{3.34}$$

The effective field experienced by the electron can be expressed as the superposition of the unloaded accelerating field produced by laser E_L, the wakefield that overlaps with the laser field E_W and the nonoverlapping component of the wakefield E_CH, i.e., $E = E_\mathrm{L} + E_\mathrm{W} + E_\mathrm{CH}$. Neglecting the nonoverlapping component of the wakefield which is small in comparison to the accelerating gradient, the electron's energy gain over one grating period Λ and transit time $\tau_\mathrm{c} = \Lambda/(\beta_\mathrm{e} c)$ can be estimated by

$$eV_1 = -\frac{A}{Z_0}(E_\mathrm{W}^2 + E_\mathrm{L}E_\mathrm{W})\tau_c \tag{3.35}$$

where A is the effective area. Assuming $E_\mathrm{W} = -\alpha E_\mathrm{L}$ and $\alpha \ll 1$, the energy gain for a single electron is

$$eV_1 = -\frac{A}{Z_0}(\alpha^2 E_\mathrm{L}^2 - \alpha E_\mathrm{L}^2)\tau_c \approx \alpha \frac{A\tau_c}{Z_0} E_\mathrm{L}^2 \tag{3.36}$$

By defining the shunt impedance $Z_\mathrm{S} = V^2/P_\mathrm{l}$, we have

$$\alpha = \frac{eZ_\mathrm{S}}{2V_1\tau_c} \tag{3.37}$$

For an electron bunch with an electron number N, the electron's energy gain can rewritten as

$$NeV_\mathrm{N} = -\frac{A}{Z_0}(N^2 E_\mathrm{W}^2 + NE_\mathrm{L}E_\mathrm{W})\tau_c \tag{3.38}$$

where V_N is the new voltage change under beam loading conditions. The energy gain for one electron in the bunch can be given by

$$eV_N = -\frac{A}{Z_0}(N\alpha^2 E_{\mathrm{L}}^2 - \alpha E_{\mathrm{L}}^2)\tau_c = eV_1(1 - N\alpha) \tag{3.39}$$

Therefore, the loaded gradient can be given by

$$G_{\mathrm{L}} = \frac{V_N}{\Lambda} = \frac{V_1(1 - N\alpha)}{\Lambda} = G_{\mathrm{a}} - N\frac{eZ_{\mathrm{S}}}{2\tau_c} = G_{\mathrm{a}} - \frac{NeZ_{\mathrm{S}}\beta_{\mathrm{e}}c}{2\Lambda^2} \tag{3.40}$$

The acceleration efficiency is the ratio of the electrons' energy gain NeV_N to the electromagnetic energy from the laser of power P_{l} and FWHM pulse duration τ_{p}:

$$\eta(N) = \frac{Ne\Lambda G_L(N)}{P_{\mathrm{l}}\tau_{\mathrm{p}}} = \frac{Ne\Lambda}{P_{\mathrm{l}}\tau_{\mathrm{p}}}\left[G_{\mathrm{a}} - \frac{NeZ_{\mathrm{S}}\beta_{\mathrm{e}}c}{2\Lambda^2}\right] \tag{3.41}$$

Using Eq. 3.41,the maximum optical-to-beam efficiency and the corresponding optimum bunch charge are calculated to be 1.4% and 2.9 fC, respectively. The efficiency for single-bunch operation can be improved by optimizing the reflectivity of SWGs in the design[69]. With a laser pulse duration of a few hundreds of femtoseconds, multiple-bunch operation, i.e., using multiple electron bunches per laser pulse, can be introduced to further enhance the efficiency[70].

3.4 Parameter study of a 1 MeV electron source

In this section, we will show that, by using a number of grating stages with different grating periods (Λ) from stage to stage, the electrons can be accelerated from 50 keV to 1 MeV within several millimeters. Another design using an identical grating period (Λ) for a group of stages to reduce the fabrication cost will also be presented.

As is shown in Section. 3.3.1, accelerated with a single grating stage that contains tens of grating periods driven by a single Gaussian laser pulse, the electron energy gain is limited by the damage threshold of dielectric materials and the dephasing effect. Using pulse-front tilted laser and changing the grating period as the electron gains energy would increase the interaction length while keeping high accelerating gradient, so that the single-stage energy gain can be higher. However, in an electron source for radiobiology research which has an output electron energy of $\sim$ 1 MeV, multi-stage acceleration is required. Ideally, laser power delivery would be integrated on-chip. Here, in order to develop a 1 MeV electron source as a tool for radiobiology research, we discuss the required accelerator parameters and laser parameters.

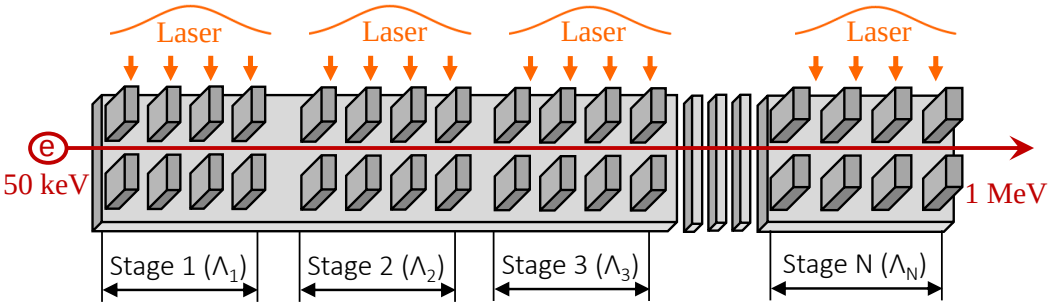

FIGURE 3.17: Schematic of a multi-stage DLA-based electron source. Each accelerator stage that contains tens of unit cell is pumped by a Gaussian laser pulse. The electron is accelerated from 50 keV to 1 MeV.

As shown in Fig. 3.17, the proposed DLA-based electron source contains multiple stages of grating structures; each stage has a number of unit cells. For simplicity, here the pulse-front tilt method is not implemented. A low enhancement factor less than 10 and a channel width of $\sim$ 300 nm will be designed for each stage. As such, a required filling time that is shorter than 0.1 ps allows using a Gaussian laser duration of 0.1 ps, corresponding to a damage threshold field of 2 GV/m (i.e., $E'_{\max} \leq 2$ GV/m) when considering a damage threshold fluence of 0.2 J/cm^2 for silicon.

As is shown in Section. 3.3.1, within a single grating stage which has a limited length, the energy gain is not greatly affected by the dephasing effect. Therefore, the grating periods for all the unit cells in a singe stage are set to be identical; the value of the grating period (Λ) is set to satisfy the synchronicity condition for the electron energy after the previous stage.

To accelerate electrons from 50 keV to 1 MeV, it is ideal to design grating stage for discrete electron energies, which would be rather time-consuming. Therefore, as a rough parameter study, in the following, we will design double grating structures for about 10 discrete electron energies by following the procedure as shown in Sec. 3.2 and use the lowest value of the sustainable accelerating gradients of those structures as the accelerating gradient of the whole accelerator.

For 60 keV electrons, the grating period is required by the synchronicity condition to be $\Lambda = 691$ nm. The designed structure and the simulation result of the longitudinal electric field distribution are shown in Fig. 3.18. Figures. 3.19(a) and 3.19(b) shows the field ratios of G_a/E_0 and $G_a/E'_{\max}$ across the channel, respectively. The structure has a channel width $d = 302$ nm and an enhancement factor $A_c = 6.5$. The ratio of the accelerating gradient to the maximum field in the dielectric at the channel center is 0.163, corresponding to a sustainable on-axis accelerating gradient $G_a = 326$ MV/m. The ratio of the accelerating gradient to the peak incident field is 2.1, so the incident field is $E_0 = 155$ MV/m.

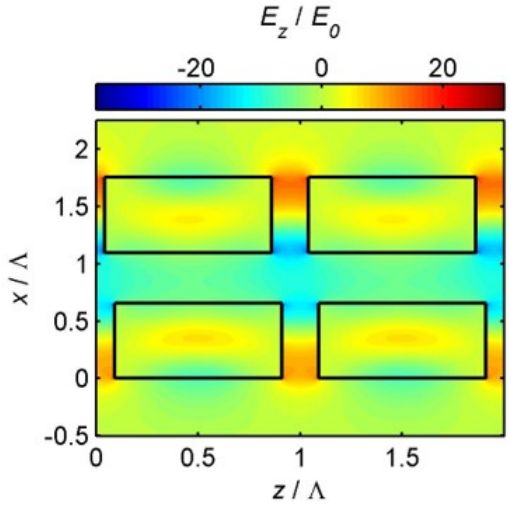

FIGURE 3.18: The ratio of the longitudinal electric field E_z to the peak incident field E_0 of a double grating for the acceleration of 60 keV electrons. $\Lambda = 692$ nm, $d = 302$ nm, $b/\Lambda = 0.819$, $s/\Lambda = 0.658$, $\Delta/\Lambda = 0.048$.

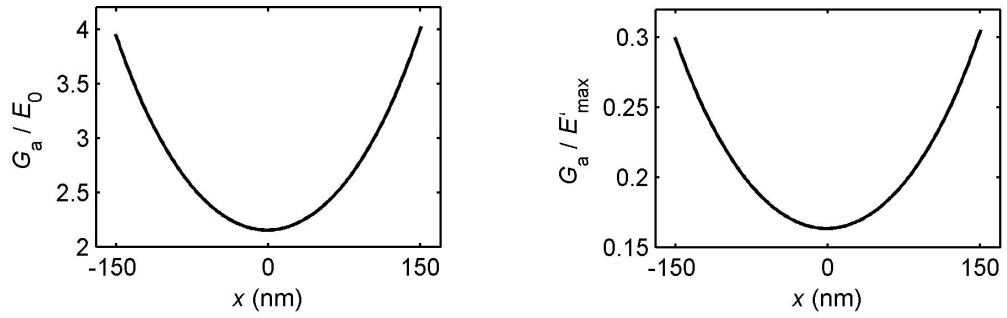

FIGURE 3.19: Accelerating gradients in the double-grating resonator for 60 keV electrons. (a) The ratio of the accelerating gradient G_a to the peak incident field E_0 as a function of position in the channel. (b) The ratio of the accelerating gradient G_a to the maximum field in the dielectric E'_max as a function of position in the channel. $\Lambda = 692$ nm, $d = 302$ nm, $b/\Lambda = 0.819$, $s/\Lambda = 0.658$, $\Delta/\Lambda = 0.048$.

For 500 keV electrons, the grating period is required by the synchronicity condition to be $\Lambda = 1337$ nm. The designed structure and the simulation results of the longitudinal electric field distribution are shown in Fig. 3.20. Figures. 3.21(a) and 3.21(b) shows the field ratio G_a/E_0 and $G_\mathrm{a}/E'_\mathrm{max}$ across the channel, respectively. The structure has a channel width $d = 309$ nm and an enhancement factor $A_\mathrm{c} = 4.5$. The ratio of the accelerating gradient to the maximum field in the dielectric at the channel center is 0.100, corresponding to a sustainable on-axis accelerating gradient $G_\mathrm{a} = 200$ MV/m. The ratio of the on-axis accelerating gradient to the peak incident field is 1.44, so the incident field is required to be $E_0 = 139$ MV/m.

In Table. 3.3, we summarize the parameters of double-grating resonators designed for different electron energies. The corresponding ratios of G_a/E_0 and $G_\mathrm{a}/E'_\mathrm{max}$ across the channel are shown in Figs. 3.22(a) and 3.22(b), respectively. The accelerating fields

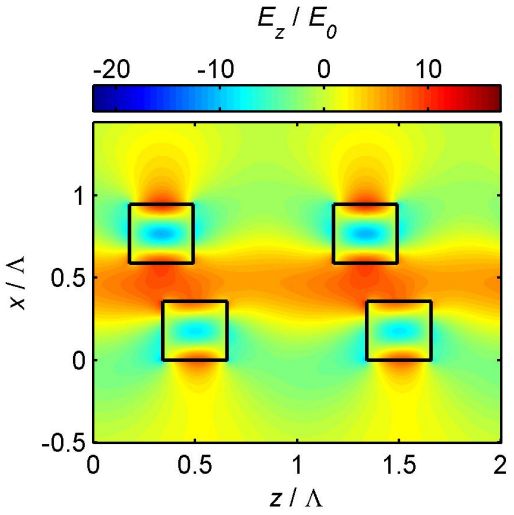

FIGURE 3.20: The ratio of the longitudinal electric field E_z to the peak incident field E_0 of a double grating for the acceleration of 500 keV electrons. $\Lambda = 1337$ nm, $d = 309$ nm, $b/\Lambda = 0.313$, $s/\Lambda = 0.357$, $\Delta/\Lambda = 0.165$.

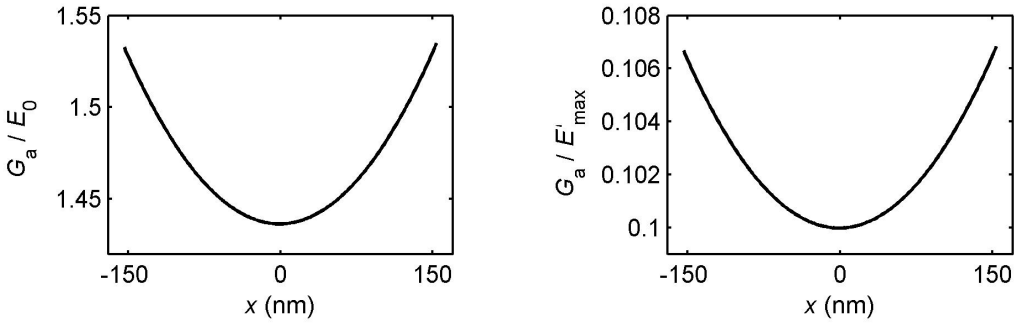

FIGURE 3.21: Accelerating gradients in the double-grating resonator for 500 keV electrons. (a) The ratio of the accelerating gradient G_a to the peak incident field E_0 as a function of position in the channel. (b) The ratio of the accelerating gradient G_a to the maximum field in the dielectric E'_max as a function of position in the channel. $\Lambda = 1337$ nm, $d = 309$ nm, $b/\Lambda = 0.313$, $s/\Lambda = 0.357$, $\Delta/\Lambda = 0.165$.

become more uniform across the channel for higher energies due to the increasing decay constant $\Gamma = \beta_\mathrm{e}\gamma_\mathrm{e}\lambda/(2\pi)$. For different electron energies, an on-axis gradient of $G_\mathrm{a} \geq 0.1E'_\mathrm{max}$ is achievable.

In the parameter study of a 1 MeV electron source, we assume for each single grating stage a peak on-axis gradient of 200 MV/m, which corresponds to $G_\mathrm{a} = 0.1E'_\mathrm{max}$. Figure 3.23 shows the electron energy as a function of position z. The grating period remains the same in a single stage but varies form stage to stage. With a total acceleration length of 7.3 mm, which corresponds to 609 stages of gratings, electrons can be accelerated from 50 keV to 1 MeV. The average accelerating gradient is 130 MV/m.

It is clear that in Fig. 3.23 the grating period changes less from stage to stage as the electron energy increases. Considering that multiple stages using an identical grating

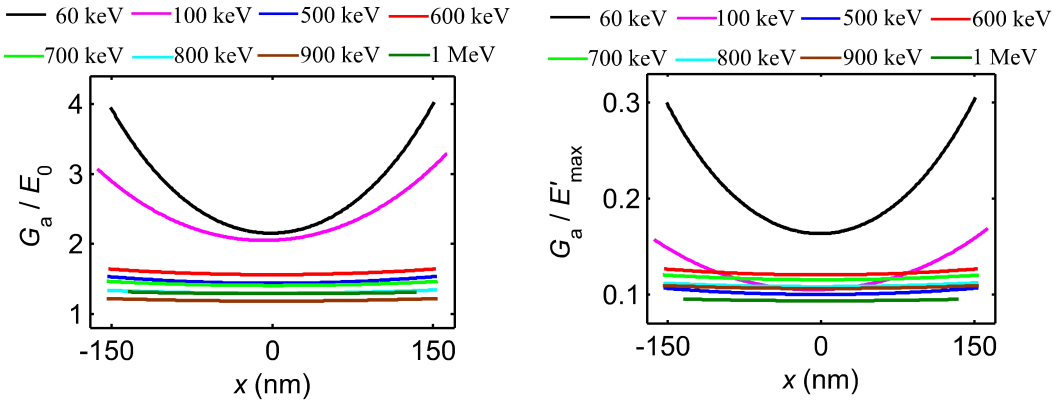

FIGURE 3.22: Accelerating gradients of double-grating resonators for different electron energies. (a) The ratio of the accelerating gradient G_a to the peak incident field E_0 as a function of position in the channel. (b) The ratio of the accelerating gradient G_a to the maximum field in the dielectric E'_{max} as a function of position in the channel. The structural parameters are shown in Table. 3.3.

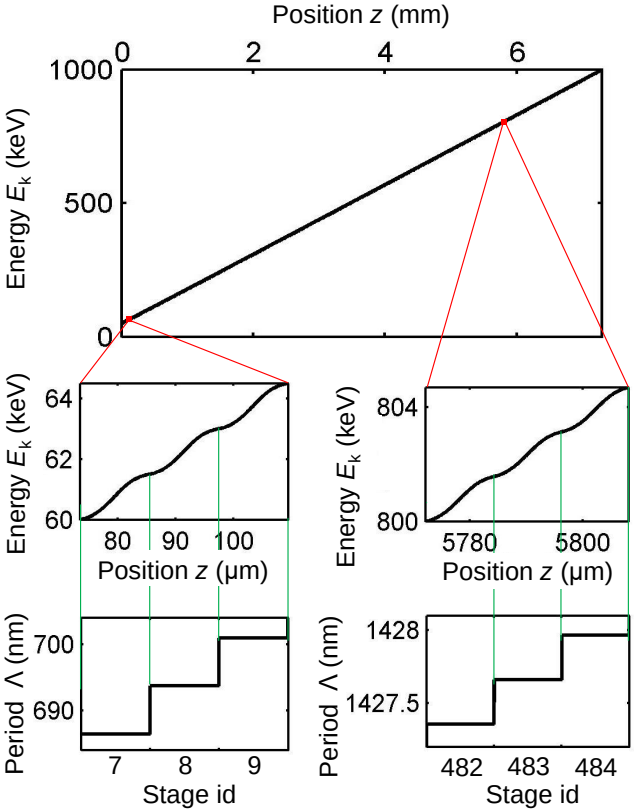

FIGURE 3.23: Multi-stage acceleration of electrons from 50 keV to 1 MeV: the electron energy versus position z. The insets show the energy E_k as a function of position z (above) and the grating period Λ as a function of stage id (below) for 3 stages when the energy is around 60 keV (left) and 800 keV (right). The peak accelerating gradient for each single stage is 200 MV/m.

TABLE 3.3: Parameters of double-grating resonators for different electron energies.

Energy (keV)	Λ (nm)	b/Λ	s/Λ	Δ/Λ	d (nm)	A_c
60	692	0.819	0.658	0.048	302	6.5
100	850	0.682	0.525	-0.058	326	9.5
500	1337	0.313	0.357	0.165	309	4.5
600	1376	0.281	0.983	0.210	307	3.9
700	1405	0.279	0.912	0.170	310	3.6
800	1427	0.280	0.891	0.170	309	3.7
900	1445	0.281	0.874	0.150	311	3.4
1000	1459	0.280	0.327	0.215	270	4.3

period may allow reducing the fabrication cost, we design a stage-graded DLA, i.e., the stages are graded into many groups, as shown in Fig. 3.24. Figure 3.24(a) shows the energy as a function of position z. The total acceleration length is around 7.6 mm, corresponding to an average accelerating gradient of 125 MV/m. Figure 3.24(b) shows the grating period as a function of the stage id. Figure 3.24(c) shows how we divided those grating stages into groups. In the design, the average gradient for each stage in one group is required to be no less than 85% of the average gradient for the group. For a low electron energy, e.g., 50 keV, if two stages use the same grating period, the energy gain for the second stage becomes rather small, or even negative, due to the dephasing effect. As a result, one group for low electron energies contains only one stage, while one group for high electron energies may contain a number of stages, e.g., group 51 contains 99 stages, group 52 contains 135 stages. In the accelerator, there are 633 grating stages in total, which are divided into 52 groups.

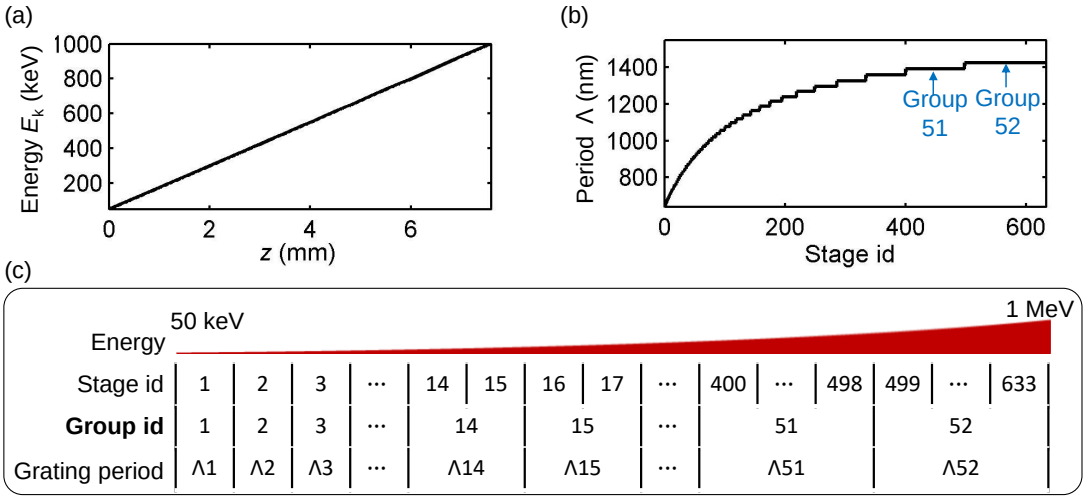

FIGURE 3.24: Stage-graded acceleration of electrons from 50 keV to 1 MeV. (a) The electron energy versus position z. (b) The grating period as a function of the stage id. (c) The division of stages into groups. The peak accelerating gradient for the first single stage in each group is 200 MV/m.

Chapter 4

Waveguides with subwavelength gratings

In this chapter, we describe a compact one-dimensional planar waveguide where the traveling accelerating wave propagates between two subwavelength gratings (SWGs). We show that by designing a matching layer, a symmetric accelerating mode with a specified field distribution can be confined in the core. We also show that the dependence of SWG reflection on its dimensions and materials can enable substantial tuning of the waveguide performance, including efficiency and sustainable gradient.

4.1 Theory for a planar waveguide

To accelerate electrons in a DLA, an accelerating mode with a longitudinal electric component and a phase velocity equals the speed of electron must be provided. To this end, hollow-core waveguides have emerged as a promising candidate for a future DLA in the past two decades. Photonic crystals (PhCs), which are regular arrays or lattices of dielectric elements, are widely used to confine the accelerating wave to the core due to the photonic band gap (PBG) arising from constructive interference of distributed reflections from each periodic layer. In PhC waveguide, the fields decay exponentially transversely away from the core; thus, good confinement of an accelerating mode requires a large number of lattice layers. Therefore, structures that can improve confinement and reduce the transverse size of waveguide structures are desirable[71, 72].

As is discussed in Chapter 3, SWGs can be used as an alternative solution for the reflectors with many desirable characteristics such as the high reflectivity, smaller volume, and polarization selection. In this section, we use an SWG as the accelerating waveguide

cladding, leading to a reduced transverse size. It may enable a compact monolithically-integrated DLA, which is useful for many applications.

A schematic of the proposed SWG-SWG waveguide structure is shown in Fig. 4.1. It consists of two gratings followed by matching layers on either side of a hollow core. Waveguide parameters include: Λ, grating period; $2d$, hollow core width; $h-d$, matching layer thickness; t, grating thickness; b, grating bar width; a, grating gap width. We will use a high-contrast reflector, so the surrounding materials should have lower refractive indices than the bar. The gratings here can also be arranged similarly as shown in Fig. 3.3.

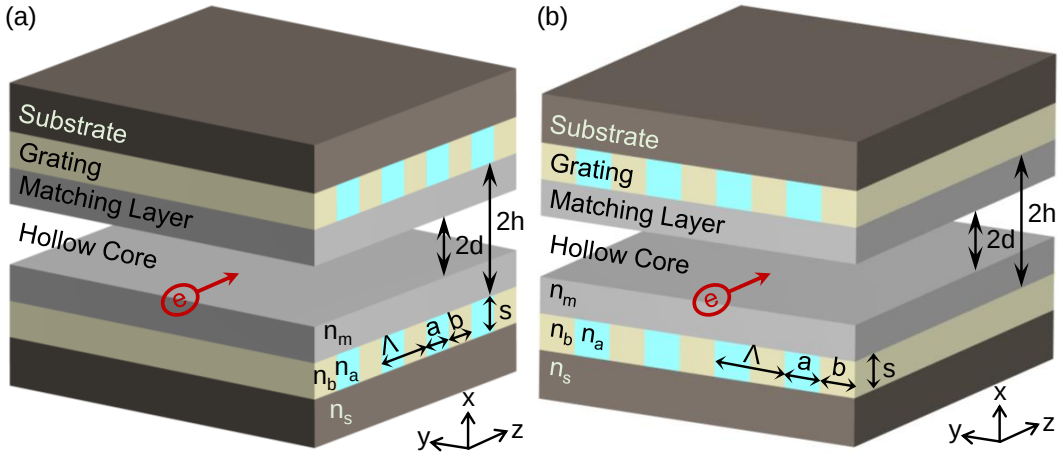

FIGURE 4.1: Schematic of an accelerating waveguide consisting of two gratings followed by matching layers on either side of a hollow core. Waveguide parameters include: Λ, grating period; $2d$, hollow core width; $h-d$, matching layer thickness; s, grating pillar height; b, grating pillar width; a, grating gap width. n_{a}, n_{b}, n_{m}, n_{s} are the refractive indices of the grating gap, grating pillar, matching layer, and substrate.

To accelerate electrons traveling in the hollow core, a special symmetric mode should be supported, as shown in Table 4.1. In Table 4.1, E_0 is the accelerating field at the channel center, k_z is the longitudinal wavenumber, $k_x = (k_0^2 - k_z^2)^{1/2}$ is the x wavenumber, $\eta_0 = \sqrt{\mu_0/\varepsilon_0}$ is the free-space impedance. This accelerating mode is the same as the cosh accelerating mode in a dual-grating structure. The phase velocity of the mode, $v_{\mathrm{ph}} = \omega/k_z$, with ω being the angular frequency. The mode for a speed-of-light (SOL) electrons is specialized, which has a zero x wavenumber and thus a uniform profile across the core.

TABLE 4.1: Accelerating mode in a planar waveguide structure.

General case, $v_{\mathrm{ph}} < c$	Speed-of-light case, $v_{\mathrm{ph}} = c$
$E_z = E_0 \cos(k_x x)\mathrm{e}^{\mathrm{i}k_z z}$	$E_z = E_0 \mathrm{e}^{\mathrm{i}k_0 z}$
$E_x = -\mathrm{i}(k_z/k_x)E_0 \sin(k_x x)\mathrm{e}^{\mathrm{i}k_z z}$	$E_x = -\mathrm{i}(k_0 x)E_0 \mathrm{e}^{\mathrm{i}k_0 z}$
$H_y = -\mathrm{i}[k_0/(\eta_0 k_x)]E_0 \sin(k_x x)\mathrm{e}^{ik_z z}$	$H_y = -\mathrm{i}(k_0 x/\eta_0)E_0 \mathrm{e}^{\mathrm{i}k_0 z}$

The field components in the matching layer, which has a dielectric coefficient ε_{m}, can be written as a superposition of modes propagating up and down.

$$E_z = \left(C^+ \mathrm{e}^{\mathrm{i}k_{\mathrm{m},x}x} + C^- \mathrm{e}^{-\mathrm{i}k_{\mathrm{m},x}x}\right) \mathrm{e}^{\mathrm{i}k_z z}, \tag{4.1}$$

$$E_x = \frac{k_z}{k_{\mathrm{m},x}} \left(-C^+ \mathrm{e}^{\mathrm{i}k_{\mathrm{m},x}x} + C^- \mathrm{e}^{-\mathrm{i}k_{\mathrm{m},x}x}\right) \mathrm{e}^{\mathrm{i}k_z z}, \tag{4.2}$$

$$H_y = \frac{k_0 \varepsilon_{\mathrm{m}}}{\eta_0 k_{\mathrm{m},x}} \left(-C^+ \mathrm{e}^{\mathrm{i}k_{\mathrm{m},x}x} + C^- \mathrm{e}^{-\mathrm{i}k_{\mathrm{m},x}x}\right) \mathrm{e}^{\mathrm{i}k_z z}, \tag{4.3}$$

where $k_{\mathrm{m},x} = \sqrt{\varepsilon_{\mathrm{m}} k_0^2 - k_z^2}$ is the x wavenumber in the matching layer.

Imposing the boundary conditions at $x = d$ yields

$$C^+ = (C^-)^* = \frac{1}{2} \mathrm{e}^{-\mathrm{i}k_{\mathrm{m},x}d} E_0 \left[\cos(k_x d) + \mathrm{i} \frac{k_{\mathrm{m},x}}{\varepsilon_{\mathrm{m}} k_x} \sin(k_x d)\right], \ v_{\mathrm{ph}} < c \tag{4.4}$$

$$C^+ = (C^-)^* = \frac{1}{2} \mathrm{e}^{-\mathrm{i}k_{\mathrm{m},x}d} E_0 \left(1 + \mathrm{i} \frac{k_{\mathrm{m},x} d}{\varepsilon_{\mathrm{m}}}\right), \ v_{\mathrm{ph}} = c. \tag{4.5}$$

The boundary conditions at the interface between the matching layer and the grating layer is determined by reflection coefficient $|r_0|$ and reflection phase $\psi_{R,0}$.

$$E_z^-(h) = |r_0| e^{\mathrm{i}\psi_{R,0}} E_z^+(h). \tag{4.6}$$

When a near-unity reflectivity provided by the grating, i.e., $|r_0| \approx 1$, Eq. 4.6 can be rewritten as

$$C^- \mathrm{e}^{-\mathrm{i}k_{\mathrm{m},x}h} = e^{\mathrm{i}\psi_{R,0}} C^+ \mathrm{e}^{\mathrm{i}k_{\mathrm{m},x}h}. \tag{4.7}$$

Based on Eq. 4.4, 4.5 and 4.7, a transcendental relation which determines the thickness of the matching layer can be written as

$$\tan\left[k_{\mathrm{m},x}(h-d) + \frac{\psi_{R,0}}{2}\right] = -\frac{k_{\mathrm{m},x}}{\varepsilon_{\mathrm{m}} k_x} \tan(k_x d), \ v_{\mathrm{ph}} < c, \tag{4.8}$$

$$\tan\left[k_{\mathrm{m},x}(h-d) + \frac{\psi_{R,0}}{2}\right] = -\frac{k_{\mathrm{m},x} d}{\varepsilon_{\mathrm{m}}}, \ v_{\mathrm{ph}} = c. \tag{4.9}$$

When the reflection phase $\psi_{R,0} = \pi$, the grating works as if a metallic wall is placed at $x = h$. In this case, Eq. 4.8 and 4.9 can be rewritten as

$$\tan\left[k_{\mathrm{m},x}(h-d)\right] = \frac{\varepsilon_{\mathrm{m}} k_x}{k_{\mathrm{m},x}} \cot(k_x d), \tag{4.10}$$

$$\tan\left[k_{\mathrm{m},x}(h-d)\right] = \frac{\varepsilon_{\mathrm{m}}}{k_{\mathrm{m},x} d}. \tag{4.11}$$

When the reflection phase $\psi_{R,0} = 0$, the grating works as if a magnetic wall is placed at $x = h$. In this case, Eq. 4.8 and 4.9 can be rewritten as

$$\tan\left[k_{\mathrm{m},x}(h-d)\right] = -\frac{k_{\mathrm{m},x}}{\varepsilon_{\mathrm{m}} k_x}\tan(k_x d), \tag{4.12}$$

$$\tan\left[k_{\mathrm{m},x}(h-d)\right] = -\frac{k_{\mathrm{m},x} d}{\varepsilon_{\mathrm{m}}}. \tag{4.13}$$

Equations. 4.10-4.13 are in agreement with the relationships for planar optical Bragg accelerator described in [32, 33].

4.2 High-reflectivity gratings for waveguides

In Chapter 3, we have shown that SWGs can provide high reflectivity for a surface-normal plane wave. In this section, we will show that SWGs can also be used as a reflector in a waveguide, where they serve as high-reflectivity mirrors at oblique incidence.

At the interface between the matching layer and grating, the incidence angle of the wave can be understood with a simple ray-optics model, as shown in Fig. 4.2. The relationship between the incidence angle and the electron velocity $v_{\mathrm{e}} = \beta_{\mathrm{e}} c$ can be given by

$$\theta = \arcsin\frac{1}{\beta_{\mathrm{e}} n_{\mathrm{m}}} \tag{4.14}$$

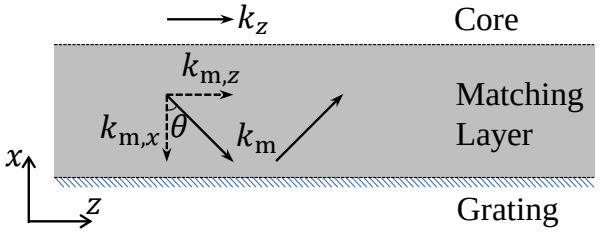

FIGURE 4.2: Ray-optics model for the field in the matching layer.

From the perspective of the waveguide, the accelerating mode described in Table 4.1 is always a TM mode. However, from the perspective of the grating, when the wave propagates along the y direction, the light polarization is TM; when the wave propagates along the z direction, the light polarization is TE. We will show that, for both TE and TM polarizations, the grating can provide high reflectivity. For simplicity, here we only consider the acceleration of SOL electrons, $v_{\mathrm{e}} = c$, corresponding to an incidence angle $\theta = \arcsin(1/n_{\mathrm{m}})$.

4.2.1 High-reflectivity gratings for TM polarization

For a SWG reflector in the waveguide, in order to obtain a high reflectivity, the requirement that the grating period should be designed to make sure all the diffraction modes except the zeroth are evanescent yields

$$\Lambda < \frac{\lambda}{n_{\mathrm{m}} + 1/\beta_{\mathrm{e}}}. \tag{4.15}$$

In the design, high-index contrast between the grating pillar and the gap is required. We use silicon as the pillar material and silicon dioxide as the material for the matching layer and substrate, i.e., $n_{\mathrm{b}} = 3.48$, $n_{\mathrm{m}} = n_{\mathrm{s}} = 1.53$. As the material should be transparent, we choose 1550 nm as the drive laser wavelength.

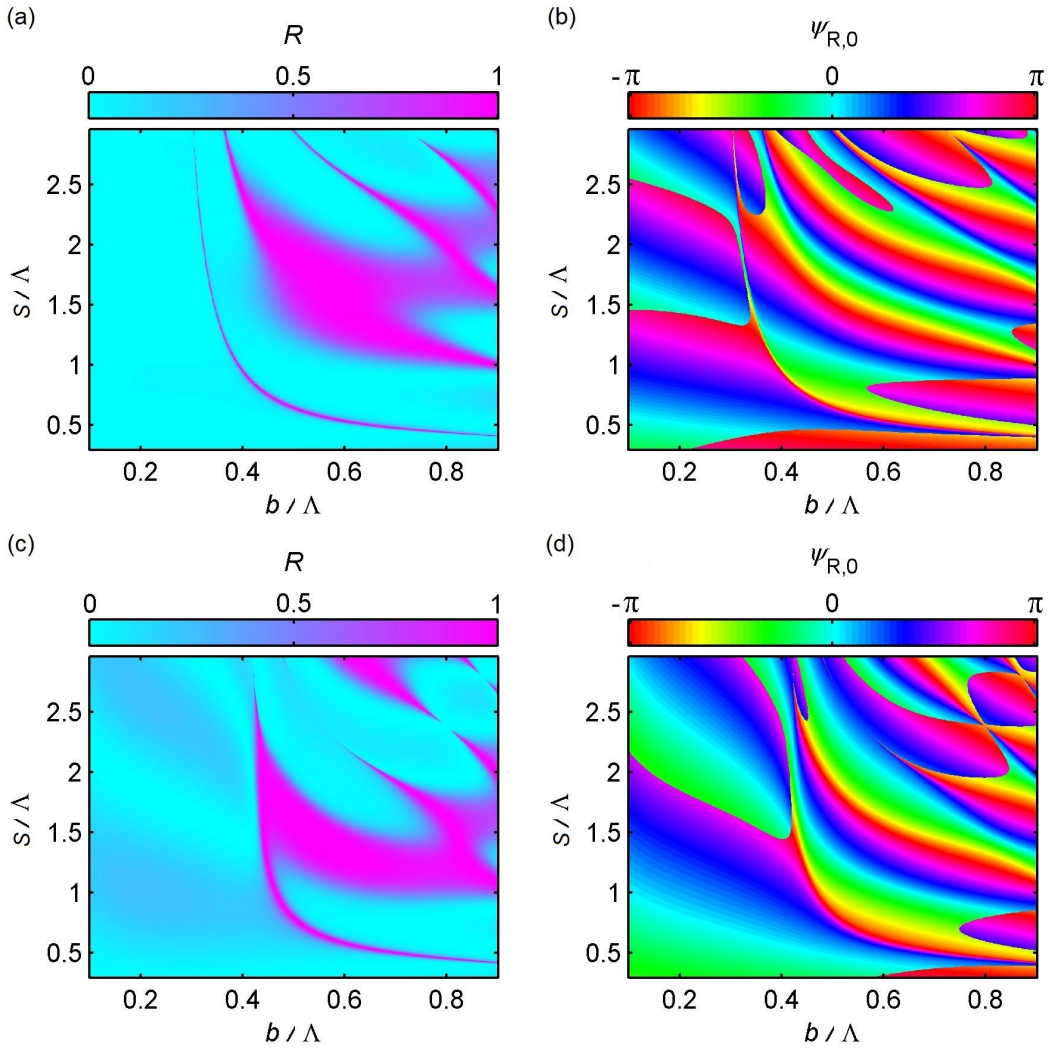

FIGURE 4.3: $s - b$ maps of the reflectivity [(a) and (c)] and reflection phase [(b) and (d)] of a grating with silicon dioxide gaps [(a) and (b), $n_{\mathrm{a}} = 1.53$, $\Lambda = 0.338\lambda$] and vacuum gaps [(c) and (d), $n_{\mathrm{a}} = 1$, $\Lambda = 0.36\lambda$] for TM polarization. $\lambda = 1550$ nm, $n_{\mathrm{b}} = 3.48$, $n_{\mathrm{m}} = n_{\mathrm{s}} = 1.53$.

Using the RCWA code, the reflectivity and reflection phase of a single grating can be calculated. First, we use silicon dioxide as the grating gap material, i.e., $n_{\mathrm{a}} = 1.53$. In Fig. 4.3[(a) and (b)], the $s - b$ maps of the reflectivity and reflection phase are shown, with a grating period $\Lambda/\lambda = 0.338$. It can be seen that a high reflectivity can be obtained by designing the pillar width (b) and height (s).

Besides the grating dimensions, the materials of the grating also affect the reflectivity pattern. Using vacuum instead of silicon dioxide as the material of the grating gap, i.e., $n_{\mathrm{a}} = 1$, the $s-b$ maps of the reflectivity and reflection phase are shown in Fig. 4.3[(c) and (d)], respectively, with a grating period $\Lambda/\lambda = 0.36$. Comparison between Fig. 4.3(a) and Fig. 4.3(c) shows that the vacuum grating gap enables a larger area of high reflectivity in the pattern, allowing more freedom of structure design.

4.2.2 High-reflectivity gratings for TE polarization

For TE-polarization, the incident light comes in xz plane, but the diffraction occurs in y direction. To make sure the diffracted modes except the zeroth are evanescent, the grating period needs to be smaller than the laser wavelength,

$$\Lambda < \lambda/\sqrt{n_{\mathrm{m}}^2 - 1}. \tag{4.16}$$

Compared with the required grating period for TM-polarization, the required grating period for TE-polarization can be larger, leading to a reduced fabrication difficulty.

As an example, we use silicon as the pillar material and silicon dioxide as the material for the grating gap, matching layer, and substrate, i.e., $n_{\mathrm{b}} = 3.48$, $n_{\mathrm{a}} = n_{\mathrm{m}} = n_{\mathrm{s}} = 1.53$. The $s-b$ maps of the reflectivity and reflection phase of a grating are show in Fig. 4.4(a) and Fig. 4.4(b), respectively, with $\Lambda/\lambda = 0.7$. It is shown that, for TE-polarized light at an oblique angle, the subwavelength gratings can also provide a high reflectivity. When the grating period is changed from $\Lambda = 0.7\lambda$ to $\Lambda = 0.6\lambda$, the results are shown in Fig. 4.4[(c) and (d)], where the highly-ordered checkerboard pattern shifts towards a larger dutycycle (b/Λ).

4.3 Field simulation of waveguides with gratings

By using the method introduced in Sec. 4.1, given the reflection phase of a grating with near-unity reflectivity, we can design a waveguide structure with different core widths. In this section, the MIT Photonic-Bands (MPB) software, an open-source package for

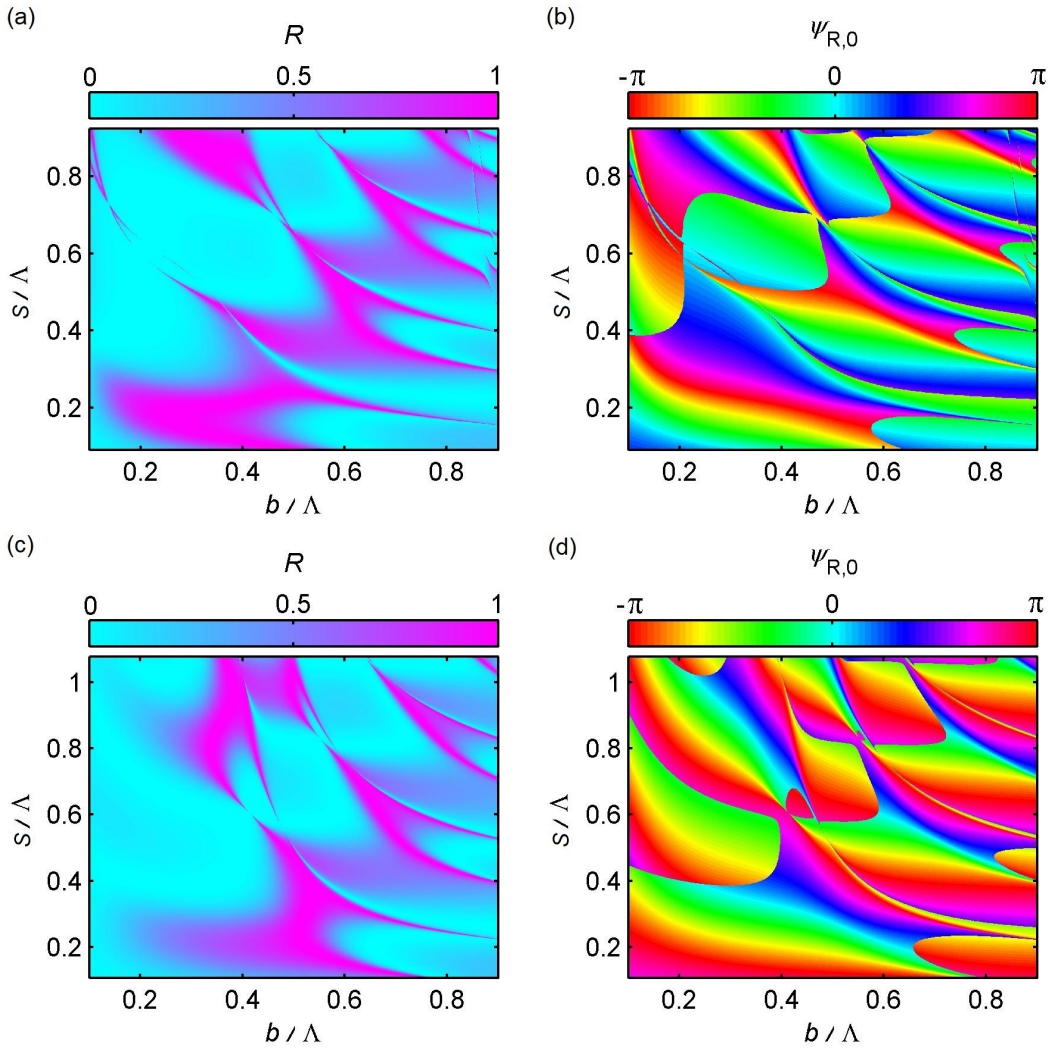

FIGURE 4.4: $s - b$ maps of the reflectivity [(a) and (c)] and reflection phase [(b) and (d)] of a grating with $\Lambda/\lambda = 0.7$ [(a) and (b)] and $\Lambda/\lambda = 0.6$ [(c) and (d)] for TE polarization. $\lambda = 1550$ nm, $n_{\mathrm{b}} = 3.48$, $n_{\mathrm{a}} = n_{\mathrm{m}} = n_{\mathrm{s}} = 1.53$.

computing electromagnetic modes of periodic dielectric structures[73], is used for simulation. We will show that high-reflectivity subwavelength gratings, for either TE or TM polarization, can efficiently confine the accelerating mode in the structure.

In the simulation, all the gratings used as reflectors are designed to have a near-unity reflectivity. All the radiation loss is assumed to be low enough to be neglected. Silicon is used as the material of the grating pillar, and silicon dioxide is used as the material for the matching layer and substrate, i.e., $n_{\mathrm{b}} = 3.48$, and $n_{\mathrm{m}} = n_{\mathrm{s}} = 1.53$. The material of the grating gap is determined in the simulation.

4.3.1 Fields in the waveguides for TM polarization

For gratings with TM polarization, the accelerating mode in the waveguide propagates perpendicularly to the pillar direction. In this case, the structure has no variation in z direction, neither do the fields. Therefore, in the following discussion, we will treat the waveguide as a 2D structure in the xy plane.

To begin with, we study the effect of the reflection phase on the field profile in the structure. Assuming a core width of 0.6λ, two subwavelength gratings, referred as SWG11 and SWG12, which have different reflection phases, are applied as reflectors for waveguides. The gratings have vacuum gaps, and the other parameters are shown in Table 4.2. In Fig. 4.5, we compare the longitudinal electric fields of the accelerating modes. In both structures, a uniform accelerating mode across the core is provided, which is as indicated by Table 4.1. With a reflection phase of $\sim \pi$, the boundary

TABLE 4.2: Waveguide parameters in Fig. 4.5.

	Polarization	Λ (nm)	b (nm)	t (nm)	ψ_R (rad)	$2d/\lambda$	$h-d$ (nm)
SWG11	TM	465	288	446	3.02	0.6	187
SWG12	TM	465	307	614	0.09	0.6	501

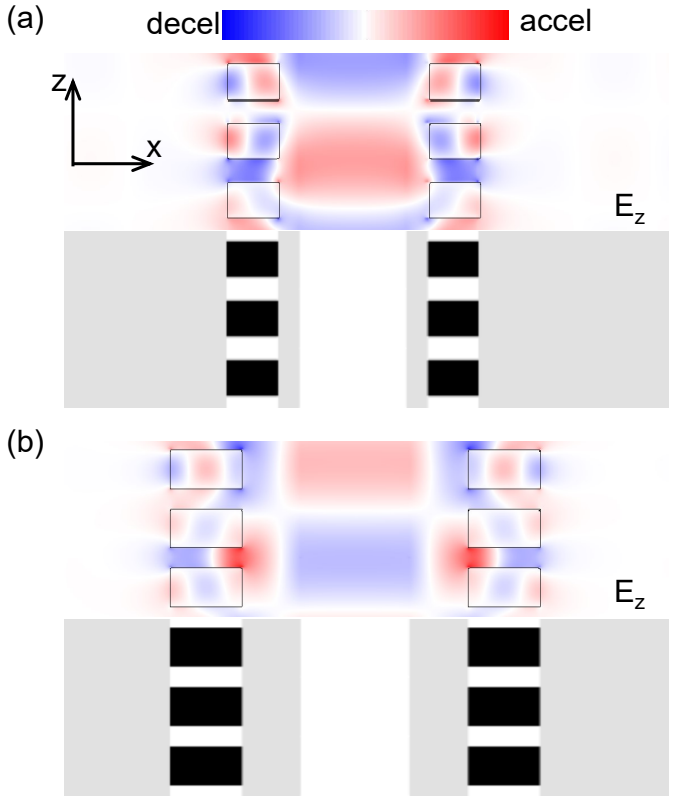

FIGURE 4.5: Longitudinal electric fields in the waveguides using SWG11 (a) and SWG12 (b). Waveguide parameters are listed in Table 4.2.

condition Eq. 4.6 indicates that in the x direction the field should vanish around the interface between the grating layer and the matching layer. This case is illustrated by Fig. 4.5(a). However, it is also shown that the effect of the evanescent modes in the vicinity of the grating, which have non-zero y wavenumbers, leads to a field modulation in the y direction close to the grating. With a reflection phase of ~ 0, the boundary condition Eq. 4.6 indicates that the fields should reach its maximum at the interface between the grating layer and the matching layer. This case is illustrated in Fig. 4.5(b), where the electric field close to the grating surface is rather intense.

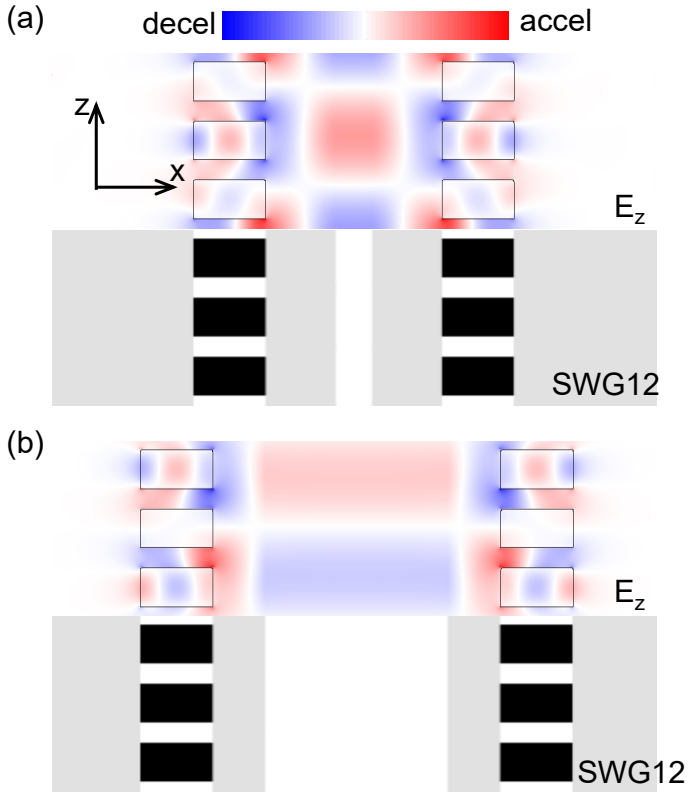

FIGURE 4.6: Longitudinal electric fields in the waveguides using SWG12 with channel widths $2d/\lambda = 0.2$ (a) and $2d/\lambda = 1$ (b). Waveguide parameters are listed in Table 4.3.

TABLE 4.3: Waveguide parameters in Fig. 4.6.

	Polarization	Λ (nm)	b (nm)	t (nm)	ψ_R (rad)	$2d/\lambda$	$h-d$ (nm)
SWG12	TM	465	307	614	0.09	0.2	597
SWG12	TM	465	307	614	0.09	1.0	448

In planar waveguide design, different core widths ($2d$) may be chosen for different purposes. As indicated by Eq. 4.8, the thickness of the matching layer depends on the core width. By designing the matching layer thickness with SWG12 as reflectors, an accelerating mode with a speed-of-light phase velocity is supported for different core widths. Figure 4.6 shows the longitudinal fields of the accelerating modes for a core with of 0.2λ

(a) and λ (b). The parameters used in the simulation are shown in Table 4.3. In MPB, the electric fields are normalized so that their energy densities have unit integral. For this reason, a comparison between Fig. 4.6(a) and Fig. 4.6(b) shows that a waveguide with a smaller core width has a more intense accelerating field in the channel, for a given laser power. This effect will be discussed later in the form of interaction impedance.

4.3.2 Fields in the waveguides for TE polarization

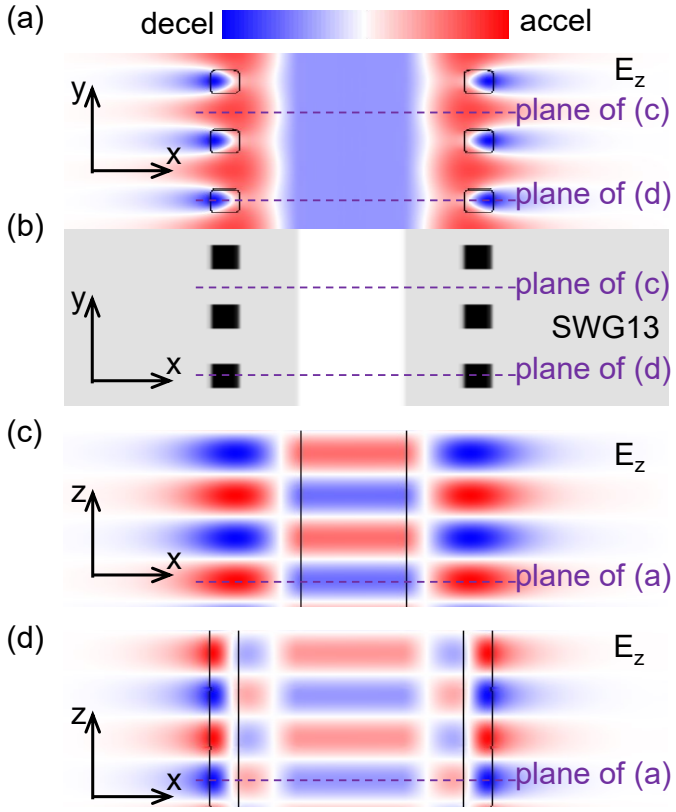

FIGURE 4.7: Longitudinal electric fields in the waveguides using SWG13. (a) E_z field in the xy plane. (b) Cross section in the xy plane. (c) E_z field in the xz plane at the grating gap center. (d) E_z field in the xz plane at the grating pillar center. Waveguide parameters are listed in Table 4.4.

TABLE 4.4: Waveguide parameters in Fig. 4.7.

	Polarization	Λ (nm)	b (nm)	t (nm)	ψ_R (rad)	$2d/\lambda$	$h-d$ (nm)
SWG13	TE	1085	416	231	0.00	0.6	512

Using gratings for TE polarization, the accelerating mode propagates parallel to the pillar direction (z direction). To begin with, a three-dimensional model is used to study the field profile of the accelerating mode in the structure. A subwavelength grating, referred as SWG13, which has a reflection phase of 0.0 rad, is applied as the reflectors. Table 4.4 shows the parameters of this waveguide, which has a core width of 0.6λ.

Figure 4.7(a) and Fig. 4.7(b) show the longitudinal electric field E_z and the cross-section of the waveguide in the xy plane, while Fig. 4.7(c) and Fig. 4.7(d) show the longitudinal electric field E_z in the xz plane at the centers of grating gap and pillar, respectively. Across the core, the longitudinal electric field is uniform, which is consistent with the field profile described in Table 4.1. Figure 4.7(a) shows that, in the structure, the diffraction effect generates a series of spatial harmonics with real y wavenumbers close to the grating, leading to a modulated pattern in the matching layer. When the matching layer is thin, the uniformity of the field in the channel may be affected. In the xz plane, the accelerating mode has a well-behaved pattern. In the region outside grating, because of the long grating period which leads to a large decay constant, the fields vanish slowly. Figure 4.7 shows that the xy distribution of the electric field can be used to characterize the longitudinal electric field in the waveguide with gratings for TE polarization.

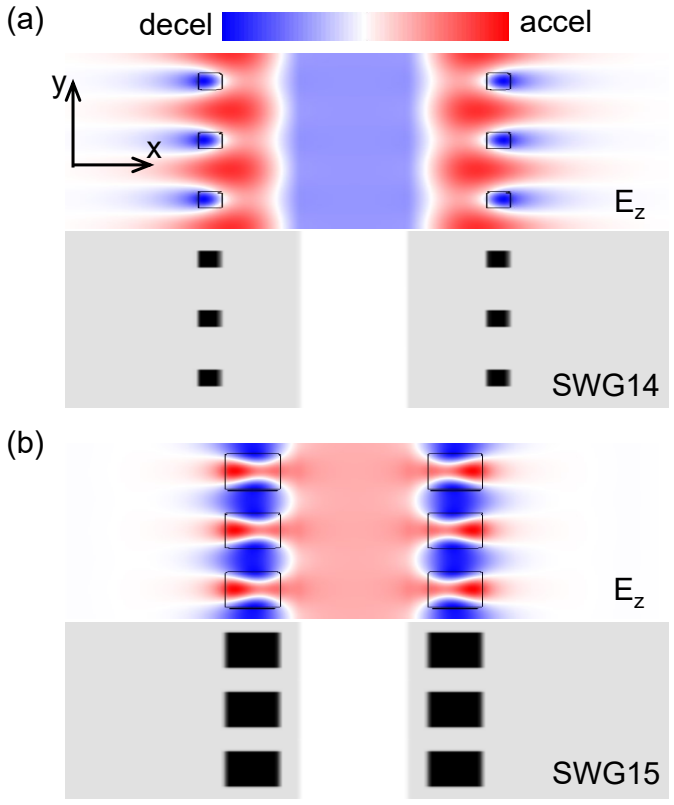

FIGURE 4.8: Longitudinal electric fields in the waveguides using SWG14 (a) and SWG15 (b). Waveguide parameters are listed in Table 4.5.

TABLE 4.5: Waveguide parameters in Fig. 4.8.

	Polarization	Λ (nm)	b (nm)	t (nm)	ψ_R (rad)	$2d/\lambda$	$h-d$ (nm)
SWG14	TE	1085	298	184	-1.60	0.6	682
SWG15	TE	775	465	463	-3.13	0.6	174

Figure 4.8 shows the longitudinal electric fields of the waveguides consisting of gratings with different reflection phases. These two subwavelength gratings, referred as SWG14 and SWG15, have a reflection phase of -1.6 rad and -3.1 rad, respectively. Table 4.5 shows the parameters of the waveguides, with a core width of 0.6λ. As discussed previously, the fields close to the grating are modulated due to the evanescent fields. In particular, in the case of Fig. 4.5(b), the thickness of the matching layer is so thin that there is a slight modulation of the fields in the core because of the unvanished evanescent fields.

Figure 4.9 shows the longitudinal fields of the accelerating mode for a core with of 0.2λ and λ, using SWG14 as reflectors. As discussed previously, a larger core width leads in a less intense accelerating field in the core with a given total energy.

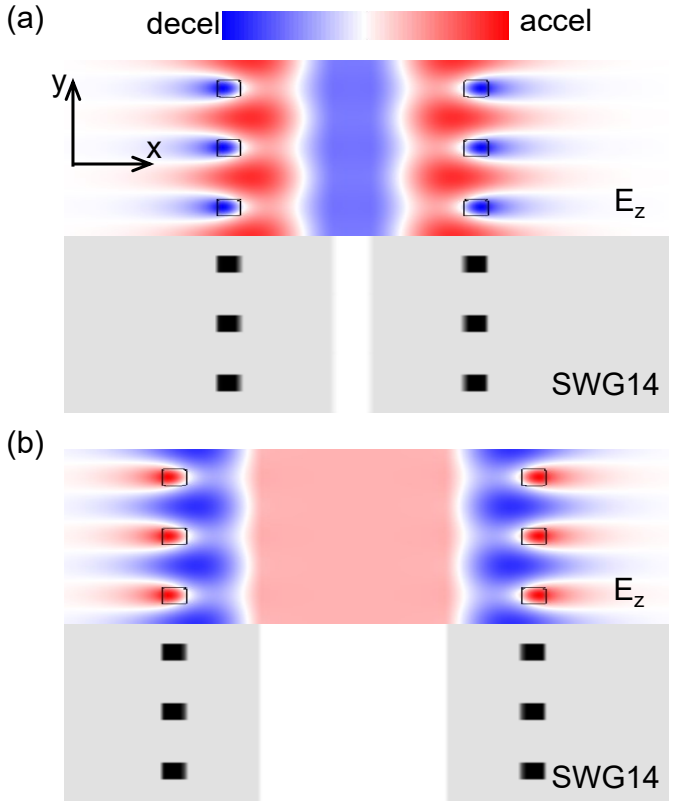

FIGURE 4.9: Longitudinal electric fields in the waveguides using SWG14 with channel widths $2d/\lambda = 0.2$ (a) and $2d/\lambda = 1$ (b). Waveguide parameters are listed in Table 4.6.

TABLE 4.6: Waveguide parameters in Fig. 4.9.

	Polarization	Λ (nm)	b (nm)	t (nm)	ψ_R (rad)	$2d/\lambda$	$h-d$ (nm)
SWG14	TE	1085	298	184	-1.60	0.2	778
SWG14	TE	1085	298	184	-1.60	1.0	629

4.3.3 Performance of waveguides with subwavelength gratings

As an accelerating structure, there are several figures of merit that characterize the structure's performance, including the group velocity ($v_\mathrm{g} = \beta_\mathrm{g} c$), the interaction impedance (Z_int), the sustainable gradient ($G_\mathrm{a,max}$), and the maximum acceleration efficiency (η_max).

In order to study the waveguide performance, five examples of high-reflectivity SWGs, with their parameters listed in Table 4.7, are applied as mirrors. Among these SWGs, the SWG14 for TE polarization has been introduced in Sec. 4.3.2 to study the field profile of the accelerating mode.

TABLE 4.7: Parameters of SWGs used in the performance estimation.

	Polarization	ε_a	Λ (nm)	b (nm)	t (nm)	ψ_R (rad)
SWG14	TE	2.38	1085	298	184	-1.60
SWG16	TE	2.38	930	481	214	-0.80
SWG17	TE	1	775	512	420	2.60
SWG18	TM	1	558	374	625	1.66
SWG19	TM	1	558	288	737	1.57

The group velocity is the velocity with which the envelope of a laser pulse propagates through the waveguide. For a specified waveguide length (L), the group velocity determines the minimum pulse length (τ_p), which is the time lag of a laser pulse with respect to an electron bunch, $\tau_\mathrm{p} = L(1 - \beta_\mathrm{g})/(\beta_\mathrm{g} c)$. To make use of the desired scaling of damage thresholds for ultrashort pulses, a high group velocity which requires a shorter laser pulse is desirable. Figure 4.10 shows the group velocity of the accelerating mode in the waveguides with using gratings as shown in Table 4.7 as mirrors. It shows that the waveguide dimensions and materials can enable substantial tuning of the group velocity. For waveguides with a given high-reflectivity grating as mirrors, a larger core width enables a higher group velocity.

The interaction impedance (Z_int) is a measure of the relation between the accelerating gradient G_a and the power (P_l) flowing in the accelerating mode, assuming a thickness of one wavelength in the y direction. It can be given by

$$Z_\mathrm{int} = \frac{G_\mathrm{a}^2 \lambda^2}{P_\mathrm{l}}. \tag{4.17}$$

A higher impedance corresponds to providing a higher accelerating gradient with given laser power, allowing more laser-efficient acceleration, which is desired in the accelerator design. Figure 4.11 shows the interaction impedance as a function of channel width for the waveguides with gratings as shown in Table 4.7. The comparison shows that, among

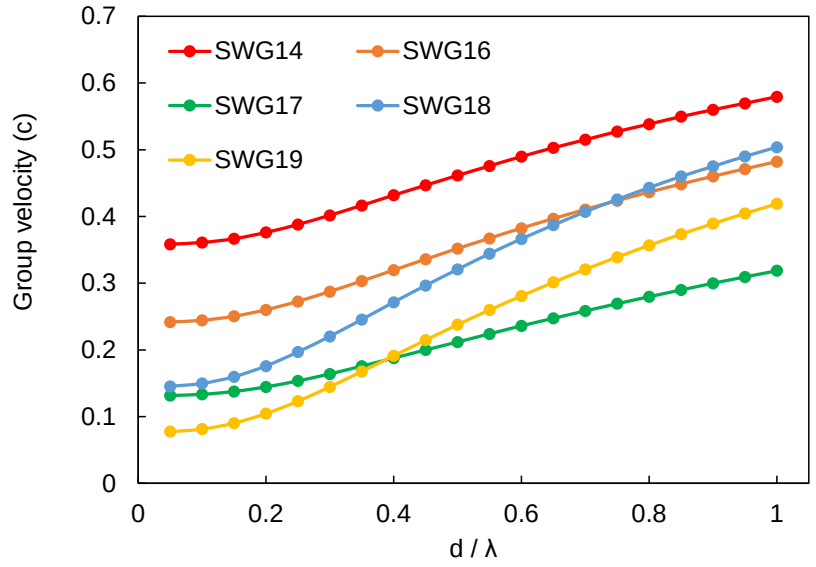

FIGURE 4.10: Group velocity of the accelerating mode in the waveguides with different gratings as mirrors. The matching layer thickness is determined by Eq. 4.9. Grating parameters are listed in Table 4.7.

these gratings, SWG18 and SWG19 that have TM polarization form waveguides with higher impedances than these gratings for TE polarization. For each waveguide, the interaction impedance decreases with an increasing core width.

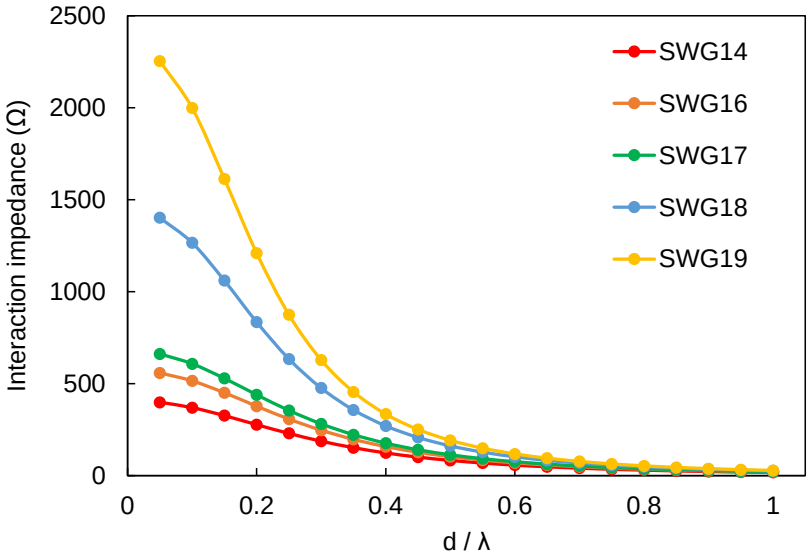

FIGURE 4.11: Interaction impedance of the accelerating mode in the waveguides with different gratings as mirrors. The matching layer thickness is determined by Eq. 4.9. Waveguide parameters are listed in Table 4.7.

The acceleration efficiency is an important parameter that characterize the laser-to-electron coupling. The maximum acceleration efficiency (η_{max}) is determined by both

the interaction impedance and the group velocity[74, 75],

$$\eta_{\max} = \frac{\beta_g}{1-\beta_g}\frac{Z_{\text{int}}}{\eta_0}\frac{d}{\lambda}. \tag{4.18}$$

Figure 4.11 shows the maximum acceleration efficiency as a function of channel width for the waveguides with gratings as shown in Table 4.7. The different trends between group velocity and interaction impedance for an increasing core width lead to an optimum value for the maximum efficiency. Among these examples of the waveguides, the waveguide with SWG19 has the highest efficiency of $\sim 10.8\%$.

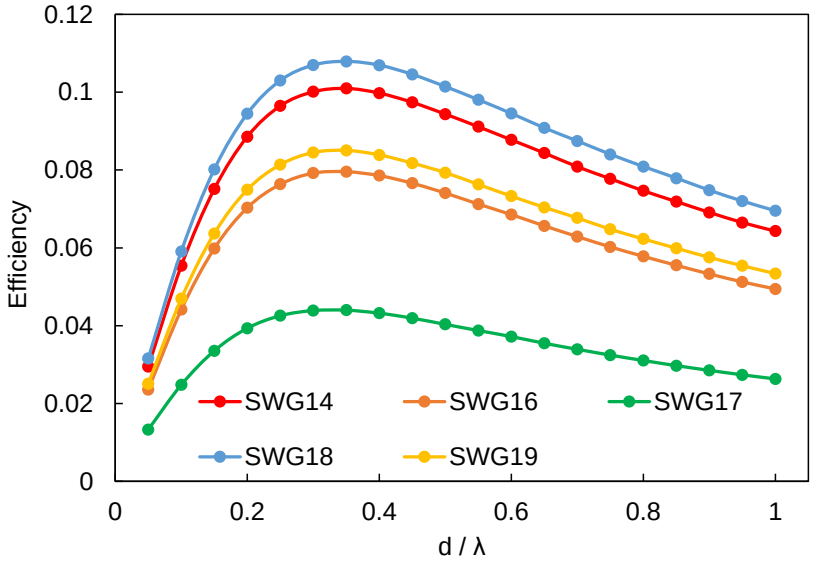

FIGURE 4.12: Efficiency of the accelerating mode in the waveguides with different gratings as mirrors. The matching layer thickness is determined by Eq. 4.9. Waveguide parameters are listed in Table 4.7.

As introduced in Chapter 3 for grating structure, the highest accelerating gradient in double-grating structures is limited by the damage threshold of the dielectric material. The field ratio $G_a/E'_{\max}$, referred as damage factor, can be used to estimate the maximum sustainable accelerating gradient. Figure 4.13 illustrates the damage factor as a function of channel width for the waveguides with gratings as shown in Table 4.7. It shows that, among these examples of waveguides, SWG18 and SWG19 for TM polarization have a higher damage factor. The results are in agreement with the field distribution as shown in Sec. 4.3, i.e., the waveguides using gratings for TM polarization have a less intense field in the dielectrics compared with the waveguides with gratings for TE polarization.

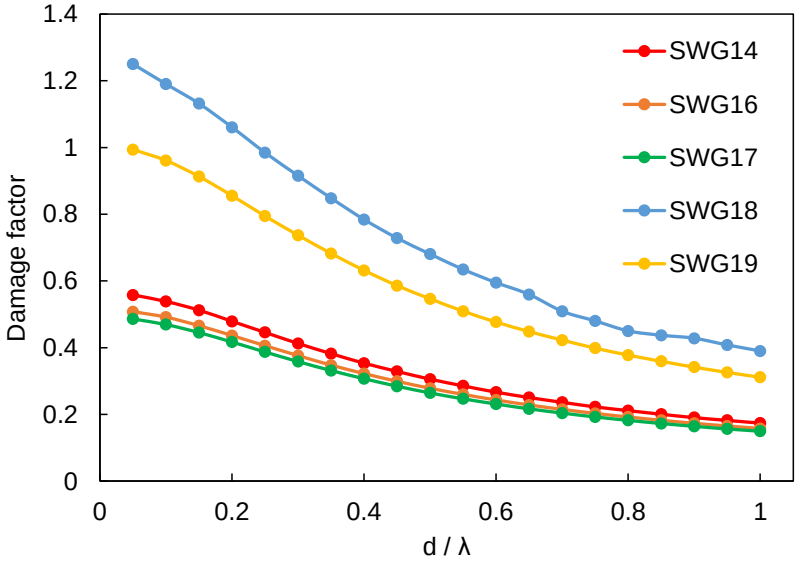

FIGURE 4.13: Damage factor of the accelerating mode in the waveguides with different gratings as mirrors. The matching layer thickness is determined by Eq. 4.9. Waveguide parameters are listed in Table 4.7.

Chapter 5

A test station for DLA structures in development

In this chapter, we present the progress in developing a test station for DLA structures, based on a laser system being developed at KEK. We describe our design of the experiment, particularly the magnets. All the components have been fabricated to date. We estimate the sustainable gradient of a fabricated single-grating structure.

5.1 System design

Considering the difficult coupling scheme for waveguide structures and the complex fabrication process for double grating structures, as a first step, a test station for measuring the acceleration and deflection of electrons at a single grating is designed. The schematic is shown in Fig. 5.1. A photocathode, driven by a laser with a wavelength of 515 nm, is used to produce a 50 keV electron beam. The beam is then focused by a magnetic quadrupole doublet onto a grating sample. Meanwhile, another laser beam with a wavelength of 1030 nm is focused onto the grating at surface-normal incidence. The accelerating mode generated upon the incidence interacts with the electrons, resulting in an energy modulation of the beam. After the interaction, the electron beam is deflected by a bending magnet spectrometer and detected by a micro-channel-plate (MCP) so that the energy gain and transverse displacement can be measured.

A vacuum chamber, as shown in Fig. 5.2, is designed to accommodate those components for the experiment. A ceramic insulator tube is used to support the high-voltage electron gun. A vent is placed close to the electron gun to ensure a high vacuum condition. The

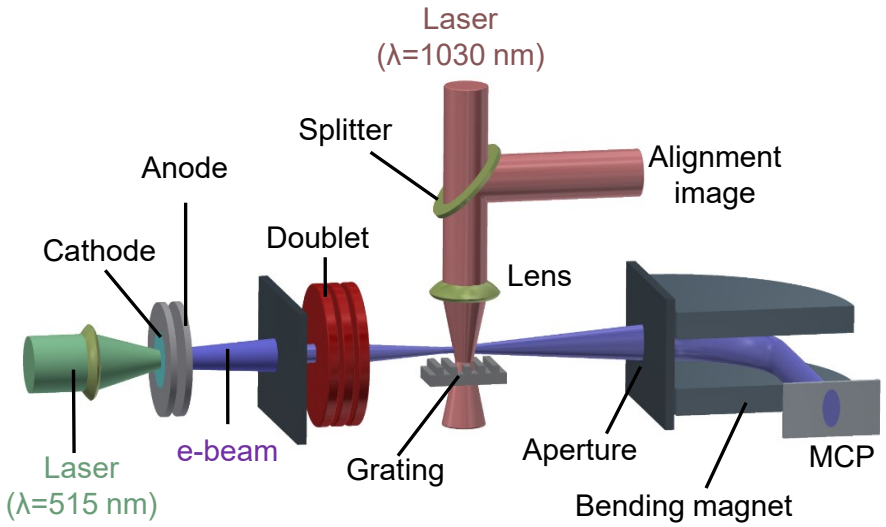

FIGURE 5.1: Schematic of the test station setup for DLA structures.

electron beam travels along the axis of the chamber. Several vacuum windows are used for the incident laser beams and the camera.

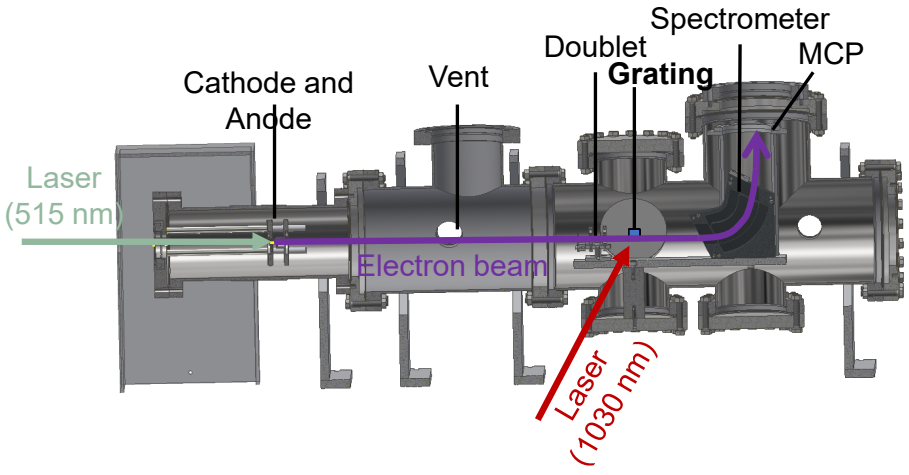

FIGURE 5.2: Technical drawing of the chamber for the test station.

As the diffraction gratings can only accelerate electrons close to their surface, a translation stage as shown in Fig. 5.3 is used to precisely align the grating to the electron beam traveling along the chamber axis. In addition, temporal alignment is to be realized by using a translation stage outside the chamber to adjust the optical path length of the incident laser.

In the following, several components for the experiment are introduced, including the grating, the electron gun, and the magnets.

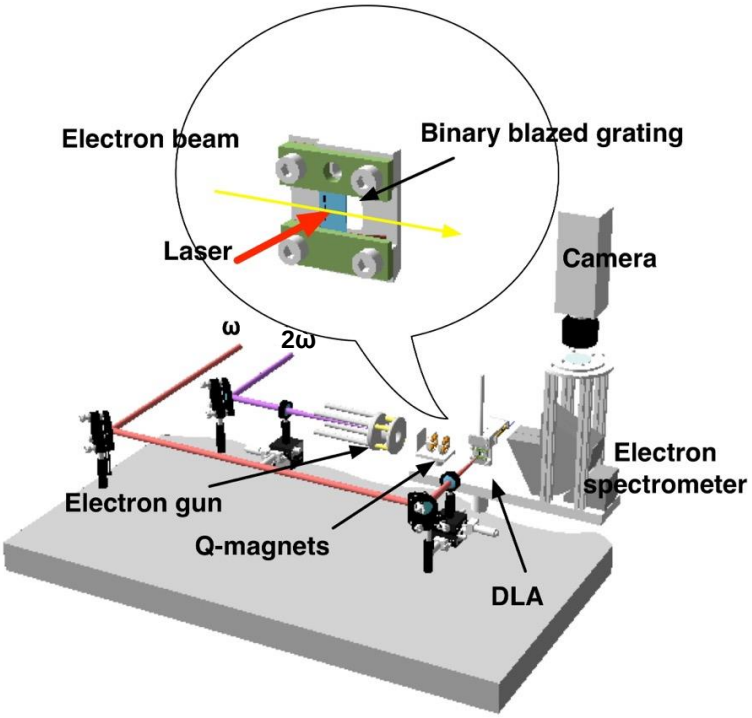

FIGURE 5.3: Schematic of the translation stage for the test station. The inset shows the sample holder. Courtesy of K. Koyama at KEK.

5.2 Fabricated single gratings

Based on the optimization of fused-silica single grating in Sec. 2, dozens of single-grating samples have been fabricated with electron-beam lithography and dry-etching technologies at NIMS[76], as shown in Fig. 5.4. The slab is with dimensions 0.36 mm × 10 mm × 5 mm ($x \times y \times z$). The mesas sitting above the slab from northwest to southeast are with dimensions 0.02 mm × 1 mm × l mm ($x \times y \times z$), where $L_{\mathrm{m}} = 0.15$ mm, 0.12 mm, 0.09 mm are the widths of the mesas. The mesas are designed to elevate the grating surface above

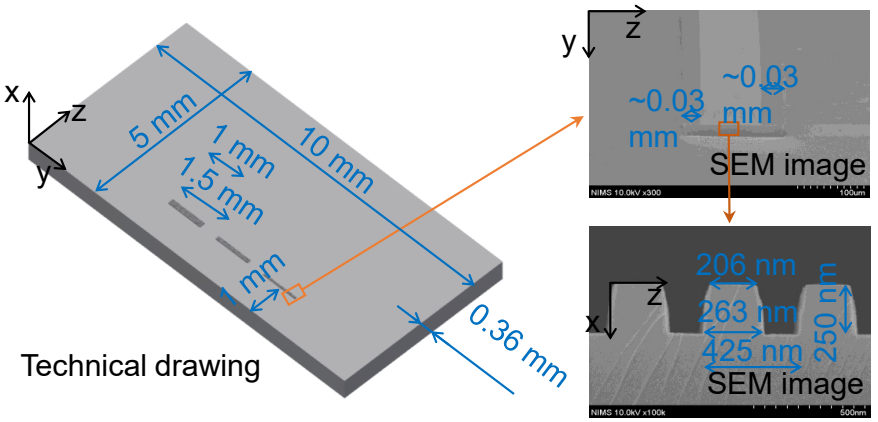

FIGURE 5.4: Fabricated sample and its dimensions.

the slab so that more electrons can pass the slab without beam loss. The distance from those mesas to the slab edge is 1 mm. The interval between adjacent mesas is 0.5 mm. Grating structures with a period of 425 nm are located on the top of three mesas, with 210, 140 and 90 periods (from northwest to southeast), corresponding to a total width of $W = 0.09$ mm, 0.06 mm, 0.03 mm, respectively. The pillar deviates from the optimized rectilinear geometry, with a pillar height of 250 nm, a pillar width 263 nm at the bottom and 206 nm at the top.

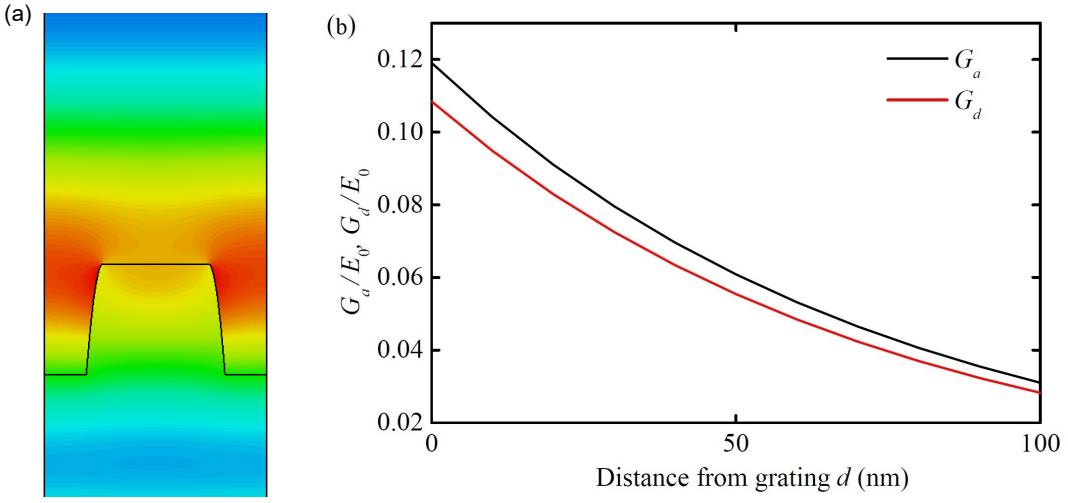

FIGURE 5.5: Field distribution (a) and gradients (b) of the fabricated sample obtained by CST.

To evaluate the effects of the deviation of the fabricated structure from the optimized design, we incorporated the grating profile extracted from the cross-section SEM image into the CST model. Figure 5.5 shows the electric field in the structure and the accelerating gradient and deflecting gradient as a function of electron-grating distance. The maximum ratio of the accelerating gradient to the maximum in-vacuum field at the grating surface is $G_{\mathrm{a}}/E_{\max} = 0.043$, corresponding to a ratio of the accelerating gradient to the incident field $G_{\mathrm{a}}/E_0 = 0.061$ at a distance of 50 nm from the pillar's upper surface. The field enhancement factor $\eta_{\max} = E_{\max}/E_0 = 1.41$. In comparison with the optimized rectangular grating whose parameters are listed in Table 2.2, the fabricated sample has a performance close to the optimized structure. Hence, the corresponding energy gain based on the laser system being developed at KEK, whose parameters are shown in Table 2.1, can be roughly estimated with the simulation results in Sec. 2.3.2. The maximum energy gain is expected to be ~ 1 keV in the experiment.

5.3 Magnets design

Figure 5.6 illustrates the focusing of electrons in the bending plane of the experiment system. The grating sample is located at the focus of quadrupole doublet and also the focus of the bending magnet. The magnets are designed with the capability of a symmetric double focusing, i.e., the focal lengths in the bending plane and transverse plane are identical. In the following, we will describe the working principle, transfer matrix calculation, CST simulation, and dissipated power estimation for the magnets.

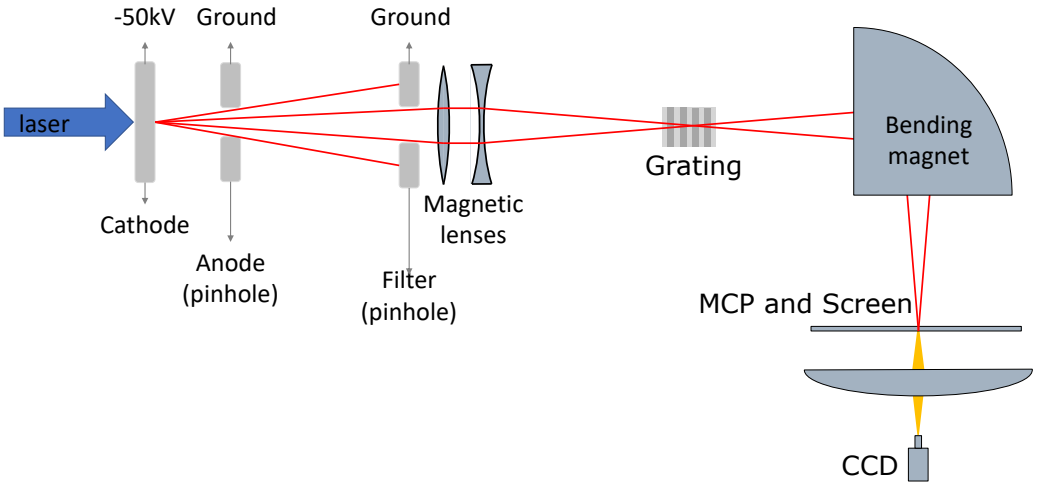

FIGURE 5.6: Focusing of electrons in the experiment.

5.3.1 Qradrupole Design

Given a single grating structure, only those electrons close to it can efficiently interact with the accelerating mode. However, the electron beam from the injector has a diameter, which is determined by the laser spot, much larger than the decay constant of the accelerating mode. Without focusing, only a tiny fraction of the electrons can interact with the accelerating mode efficiently, making the detection rather difficult. In order to focus the beam or compress it to the smallest possible radius at the grating, a quadrupole doublet is designed.

The magnetic quadrupole is illustrated in Fig. 5.7. The pole surfaces of hyperbolic profile have the same magnetic potential. Coils are winded in such a way that every other pole has a magnetic flux into the beam and every other out of the beam. The magnetic field in such a system is given by[77]

$$\mathbf{B} = \frac{B_0}{a} y\mathbf{i} + \frac{B_0}{a} x\mathbf{j} \tag{5.1}$$

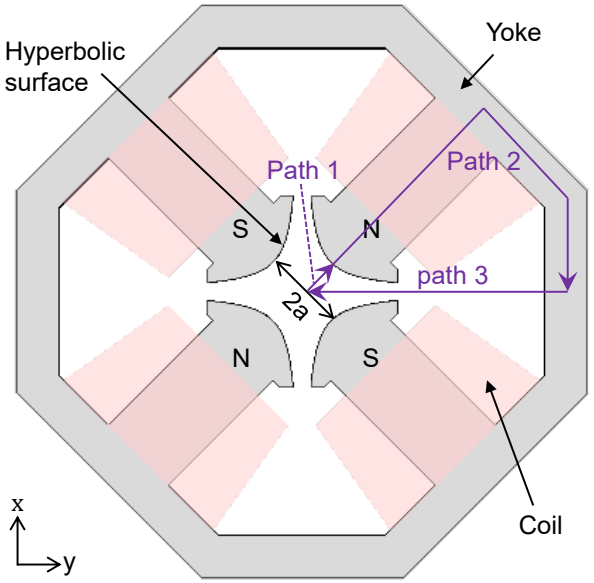

FIGURE 5.7: Schematic of a quadrupole magnet.

where $x = 0$ and $y = 0$ are located at the magnet center, B_0 is the magnetic field density at the pole surface, a is the distance from the axis to the pole tip. Charged particles with velocity $\mathbf{v} = v_z\mathbf{k}$ experience a force $F = qB_0v_z(x\mathbf{i} + y\mathbf{j})/a$, which focuses in the x direction and defocuses in the y direction. Since the transverse magnetic forces are perpendicular to the field components, motions in the transverse directions (x and y) are independent and can be analyzed separately. The particle orbit equations in the magnetic field are

$$d^2x/dz^2 = -(eB_0/\gamma m_0 a v_z)x \tag{5.2}$$

$$d^2y/dz^2 = (eB_0/\gamma m_0 a v_z)y \tag{5.3}$$

The solutions in the x direction can be written by matrix notation as

$$\mathbf{u_f} = \mathbf{A_F}\mathbf{u_i} \tag{5.4}$$

where the subscript F represents the focusing effect, the orbit vector $\mathbf{u_i} = [x_\mathrm{i}, x'_\mathrm{i}]$ is converted by the magnet to the vector $\mathbf{u_f} = [x_\mathrm{f}, x'_\mathrm{f}]$. $\mathbf{A_F}$ is the transfer matrix which contains all the parameters of lens properties,

$$\mathbf{A_F} = \begin{bmatrix} \cos(\sqrt{k}l) & \sin(\sqrt{k}l)/\sqrt{k} \\ -\sqrt{k}\sin(\sqrt{k}l) & \cos(\sqrt{k}l) \end{bmatrix}. \tag{5.5}$$

with $k = eB_0/\gamma m_0 a v_z$, and $l = \int Bdz/B_\mathrm{center}$ being the effective lens length.

In the other transverse direction (y direction), the beam is defocused. The transfer matrix can be given by

$$\mathbf{A_D} = \begin{bmatrix} \cosh(\sqrt{k}l) & \sinh(\sqrt{k}l)/\sqrt{k} \\ \sqrt{k}\sinh(\sqrt{k}l) & \cosh(\sqrt{k}l) \end{bmatrix}. \tag{5.6}$$

With one quadrupole lens, the beam cannot be focused in both transverse directions (x and y). In order to realize two-dimensional focusing, two (doublet) or three (triplet) quadrupole lenses should be used.

Here, for the sake of simplicity, we use a doublet for focusing. A magnetic doublet consists of a quadrupole, a drift space of length d, and another quadrupole. In the x direction, which is called FD channel, the first quadrupole focuses and the second defocuses. In the y direction, which is called DF channel, the first quadrupole defocuses and the second focuses. For the drift space between the quadrupoles, the transfer matrix along the z direction can be written as

$$\mathbf{A} = \begin{bmatrix} 1 & d \\ 0 & 1 \end{bmatrix}. \tag{5.7}$$

To focus equally in both transverse directions so that the minimum electron beam diameters in both transverse directions appear at the same point, two quadrupoles are of the same dimensions but with different magnetic fields at the pole tip. Based on Eq. 5.5, 5.6, and 5.7, the transfer matrices for the doublet can be written as

$$\mathbf{C_{FD}} = \mathbf{A_D}(k_1, l)\mathbf{A}(d)\mathbf{A_F}(k_2, l), \tag{5.8}$$

$$\mathbf{C_{DF}} = \mathbf{A_F}(k_1, l)\mathbf{A}(d)\mathbf{A_D}(k_2, l), \tag{5.9}$$

where $k_1 = eB_1/\gamma m_0 a v_z$ and $k_2 = eB_2/\gamma m_0 a v_z$ depend on the magnetic fields of the first and second quadrupoles, respectively.

The total current required for the coils can be calculated by

$$\oint \mathbf{H} \cdot d\mathbf{l} = \int_{\text{path1}} \frac{\mathbf{B}}{\mu_0} \cdot d\mathbf{l} + \int_{\text{path2}} \frac{\mathbf{B}}{\mu_r \mu_0} \cdot d\mathbf{l} + \int_{\text{path3}} \frac{\mathbf{B}}{\mu_0} \cdot d\mathbf{l} = \int_S J dS = NI, \tag{5.10}$$

where the integration paths are illustrated in Fig. 5.7.

In the design, first, we design a quadrupole with CST. Since the doublet is far away from the electron gun, the incident electron beam can be treated as an initially parallel beam. Considering the small beam radius in the experiment, the distance between the optical axis to the pole tip is chosen to be $a = 1.95$ mm. The longitudinal length of each

quadrupole structure is 5 mm. In Fig. 5.8(a) we show the amplitude of the magnetic field $|\mathbf{H}|$ in the quadrupole magnet. The effective length is $l = 7.5$ mm. Second, since the matrix method takes much less time, it is used to roughly determine the magnetic fields of two quadrupoles. Placing the first quadrupole at $z = 0$ and the second at $z = 20$ mm, we expect to focus the beam at $z = 80$ mm. With the transfer matrix method, the estimation requires the first quadrupole to have a magnetic field of 0.0054 T at the pole tip, and the second quadrupole 0.0074 T. Ultimately, the precise parameters of the doublet are determined with CST software. To equally focus the beam $z = 80$ mm, 20 turns of wires in total are used for each quadrupole, including 4 coils with 5 turns of wires. The coil current for the first quadrupole is $I_1 = 0.87$ A, and for the second $I_2 = 1.15$ A. The first quadrupole has a magnetic field of 0.0051 T at the pole tip and the second quadrupole 0.0068 T. The simulated magnetic field in the transverse plane (xy) of the first quadrupole and xz plane of the doublet are shown in Fig. 5.8. The differences between the required magnetic fields obtained with the transfer matrix method and CST are small, which result from the approximations used in the transfer matrix method.

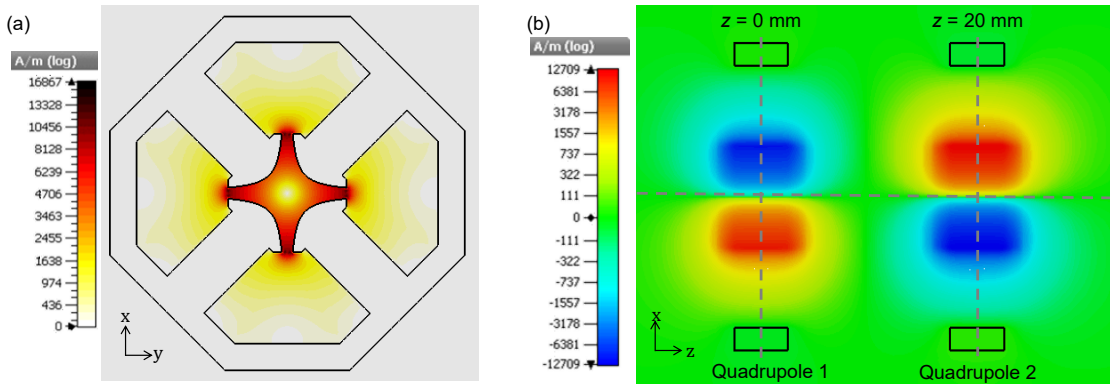

FIGURE 5.8: The magnetic field $|\mathbf{H}|$ of the first quadrupole (a) and the magnetic field H_y of the doublet (b).

The resulting particle orbits of the electrons are shown in Fig. 5.9. It shows that the orbits calculated with matrix method are in agreement with that calculated with CST. In the xz plane, the electrons are focused by the first quadrupole but defocused by the second. In the yz plane, the electrons are defocused by the first quadrupole but focused by the second. In both xz and yz planes, the total effect of the doublet focuses the beam at $z = 80$ mm.

In the following, we will estimate the dissipated power of the doublet. The wire used for the coil has a diameter of 2 mm, with a corresponding cross-sectional area of $a_{\text{wire}} = 3.1$ mm^2. For each quadrupole, the total length of the wire can be estimated to be

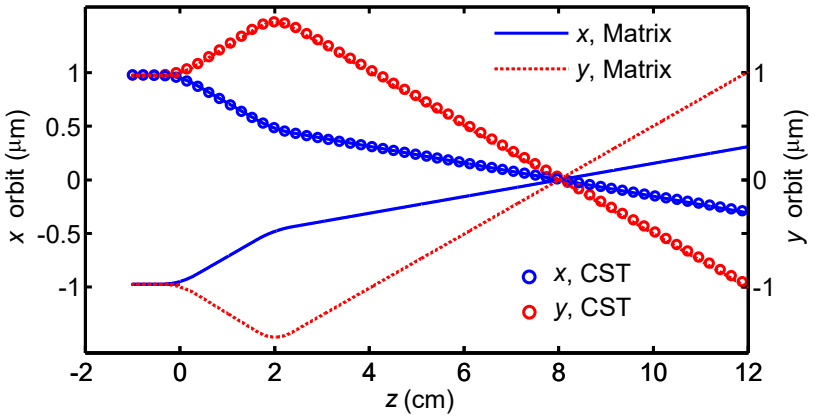

FIGURE 5.9: The focusing of electrons calculated with matrix method and CST.

$L_{\text{wire}} = 608$ mm. The resistance of wire in each quadrupole is

$$R_{\text{coil}} = \frac{\rho L_{\text{wire}}}{a_{\text{wire}}} = 3.3 \times 10^{-5}\ \Omega. \tag{5.11}$$

where ρ is the resistivity (for copper, $\rho \approx 1.68 \times 10^{-8}$ Ωm at 40 °C). Thus, the power dissipated by the first quadrupole is given by

$$P_1 = I_1^2 R_{\text{coil}} = 0.021\ \text{mW}, \tag{5.12}$$

and the power dissipated by the second quadrupole is given by

$$P_2 = I_2^2 R_{\text{coil}} = 0.037\ \text{mW}. \tag{5.13}$$

Therefore, the overall dissipated power can be calculated by

$$P = P_1 + P_2 = 0.058\ \text{mW}. \tag{5.14}$$

5.3.2 Spectrometer design

A sector bending magnet spectrometer is designed to analyze the electrons after the interaction. As shown in Fig. 5.2, the spectrometer is put in the vacuum. Considering the low repetition rate ($\sim$ 20 Hz) in our experiment, the thermal issue can be neglected.

As the name suggests, the heart of the bending magnet spectrometer is a magnetic sector, which provides a nearly constant magnetic field in the magnetic gap. It serves to produce an energy dispersion and a direction focusing for the electrons traveling through the field[78]. The electrons entering the field with different kinetic energy follow different circular trajectories through the field, known as energy dispersion. A spectrometer is designed in such a way that particles with a kinetic energy of $E_{\text{k},0}$ travel along the

optical axis. These particles are called the reference particles. The radius of the optical axis can be given by

$$R = \frac{\gamma_e \beta_e m_0 c}{Be}. \tag{5.15}$$

The dipole elements have focusing/defocusing properties in the bending plane because the path lengths of the outer trajectories are longer than the path lengths of the inner trajectories for electrons with the same energy[79]. It is less obvious, but also true that the fringing fields at the entrance and emergence boundaries of the sector provide an axial focusing action. In Fig. 5.10, we illustrate the trajectories of electrons with different energies in a magnetic sector, where $E_{k,0} = 50$ keV. The deflection radius of the reference particles is denoted by R, the object distance by L_1, the image distance by L_2, the incidence angle by α_{in}, the emergence angle by α_{out}, the deflection angle α_0 and the angle of the focal plane with a plane normal to the reference trajectory by φ. The energy separation and direction focusing in the bending plane of a magnetic sector is shown.

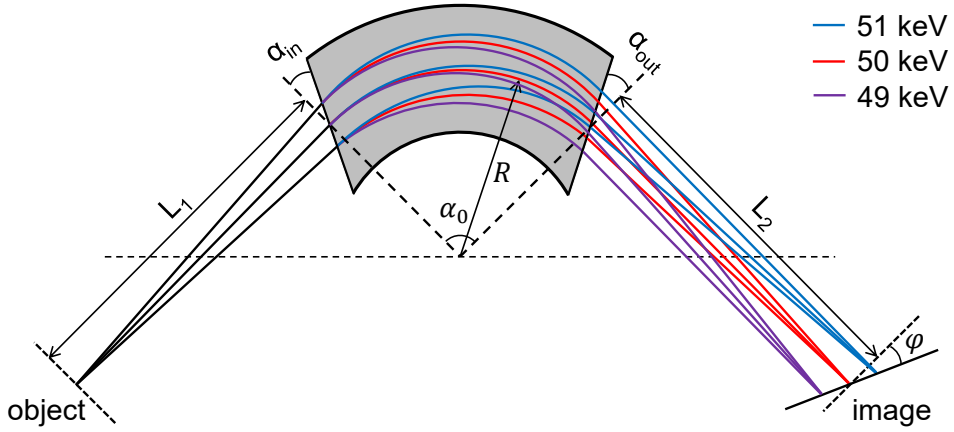

FIGURE 5.10: Illustration of the trajectories of electrons with different energies.

In a magnetic sector, the focusing in the bending plane can be traded for focusing in the other transverse plane, if the incidence angle α_{in} and the emergence angle α_{out} as shown in Fig. 5.10 deviate from 0°. The dependence of the focal lengths from the magnet edge on the incidence angle and emergence angle are given by

$$f_x = \frac{R}{\tan(\alpha_0/2) - \tan\alpha_{in,out}} \tag{5.16}$$

$$f_y = \frac{R}{\tan\alpha_{in,out}} \tag{5.17}$$

In a symmetric double-focusing dipole, the edge angles can be calculated by $2\tan\alpha_{in,out} = \tan(\alpha_0/2)$, and the focus distances by $L_1 = L_2 = 2R/\tan(\alpha_0/2)$.

In practice, the electron beam in question contains particles with kinetic energy deviating from E_0. The emergence angles at the exit for those electrons deviate from α_{out}, so those electrons are not focused at the same distance as the reference particles. The slope of the focal plane $\tan\varphi$, with φ being the angle between the focal plane and a plane normal to the reference trajectory, can be calculated by[80, 81]

$$\begin{aligned}\tan\varphi = &\frac{b}{2D_0}\left\{1+\frac{\sin\alpha_0}{b}+2\sin\alpha_0\tan\alpha_{\text{out}}+2\tan^2\alpha_{\text{out}}(1-\cos\alpha_0)\right.\\ &\left.+\frac{b[1+(b^{-1}+\tan\alpha_{\text{out}})^2]}{a[1+(a^{-1}+\tan\alpha_{\text{in}})^2]}\right\}\end{aligned} \tag{5.18}$$

with $D_0 = \{1-\cos\phi+b[\sin\alpha_0+(1-\cos\alpha_0)\tan\alpha_{\text{out}}]\}/2$, $a = L_1/R$, $b = L_2/R$.

The total current of the coil for exciting the required magnetic field can be estimated by using

$$\oint \mathbf{H}\cdot d\mathbf{l} = \int_{\text{path1}} \frac{\mathbf{B}}{\mu_0}\cdot d\mathbf{l} + \int_{\text{path2}} \frac{\mathbf{B}}{\mu_r\mu_0}\cdot d\mathbf{l} + \int_{\text{path3}} \frac{\mathbf{B}}{\mu_0}\cdot d\mathbf{l} = NI, \tag{5.19}$$

where the paths are described in Fig. 5.11.

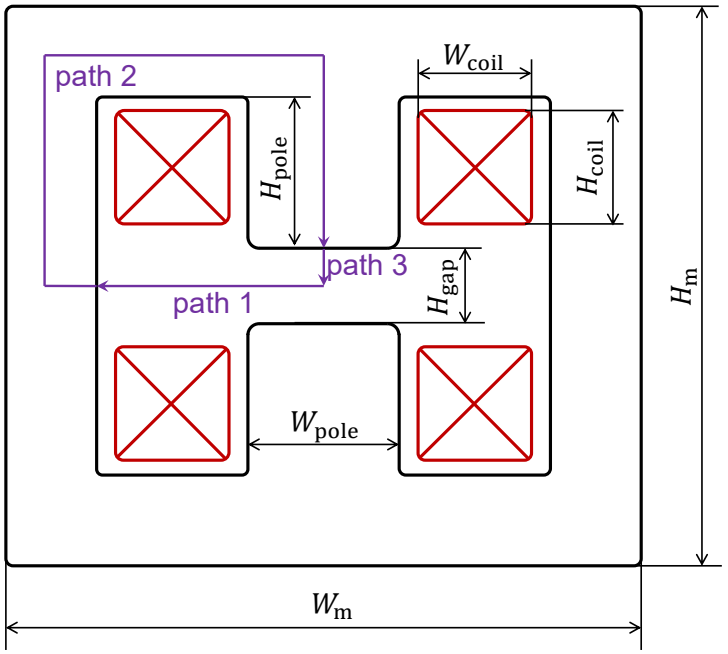

FIGURE 5.11: Cross-section showing the H-frame of the yoke.

In our case, the bending magnet is designed as a symmetric double-focusing dipole. We use an H-Frame coil magnet made of two solid pieces of SUS304 steel. The internal field gap is $H_{\text{gap}} = 5$ mm, with a bend radius $R = 50$ mm. The deflection angle is $\alpha_0 = 90°$, with edge angles being $\alpha_{\text{in}} = \alpha_{\text{out}} = 26.6°$ and the focal distances $L_1 = L_2 = 2R$. Field clamps with a thickness of 4 mm made by the same steel are used to terminate

the fringing fields of the spectrometer, and also serve to accommodate the spectrometer entrance aperture with a size of 30 mm × 5 mm. The corresponding magnetic field in the gap is $B = 0.0154$ T.

We design a good field region of width $W_{\text{tube}} = 6$ mm between the poles, which can be ensured by adding excess pole overhang[82]. The width of the pole is estimated to be 30 mm, by using

$$W_{\text{pole}} = W_{\text{tube}} + H_{\text{gap}} * (0.75 - 0.36 \ln 100 \frac{\Delta B}{B}) = 30 \text{ mm}, \text{with} \Delta B/B = 0.01\%, \quad (5.20)$$

where $\Delta B/B$ is a measure of the field uniformity.

In the simulation, the total current of the coil is precisely calculated to be 52.6 ampere-turns. For each coil, we use $N = 25$ turns of wires, consisting of 5 layers with 5 turns in each. The current of the wire is $I = 1.05$ A. Figure 5.12(a) shows the magnetic field in the bending magnet calculated with CST. A rather uniform magnetic field is generated at the center of the gap. Figure 5.12(b) shows the particle tracking result in the magnetic field. The electrons of different energies are focused to different positions, enabling the energy measurement. The energy dispersion is evaluated to be 2 mm/keV.

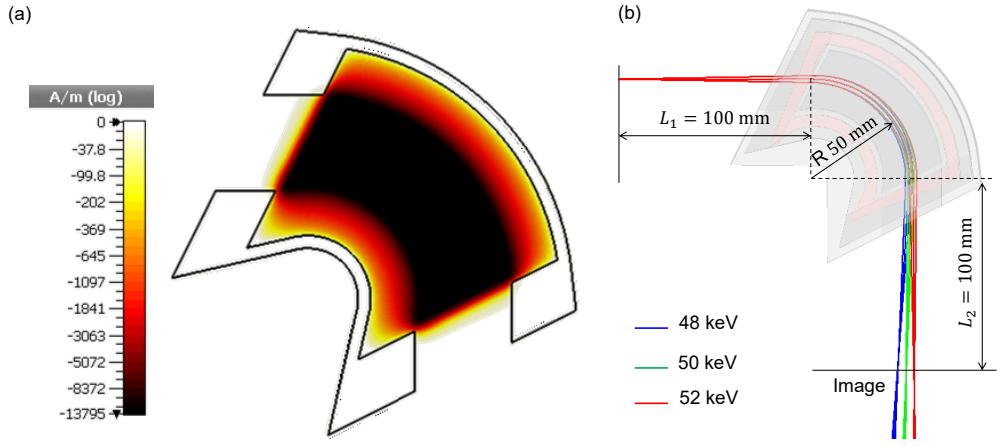

FIGURE 5.12: Magnetic field (a) and particle tracking result (b) in the bending magnet.

In the future experiment, the screen will be put at the focal point of the spectrometer, imaged by an ALLIED prosilica GC650 CCD monochrome camera with a 1/3" 659(H) × 493(V) resolution sensor and 7.4 μm(H) × 7.4 μm(V) pixel size. To roughly measure the electron energy, the screen is put normal to the reference trajectory at the focus.

In the following, we will estimate the dissipated power. The wire for the coil has a diameter of 2 mm, with a corresponding cross-sectional area of $a_{\text{wire}} = 3.1$ mm^2. The cross-sectional width and height of each coil are $W_{\text{coil}} = H_{\text{coil}} = 10$ mm. The average

circumference of the coil is estimated to be

$$C_{\text{coil}} = \pi(R + W_{\text{coil}}) + 2(W_{\text{pole}} + W_{\text{coil}}) = 268.5 \text{ mm}. \tag{5.21}$$

The power dissipated by two coils is given by

$$P = 2I^2 R_{\text{coil}} = 0.79 \text{ mW}, \qquad \text{with } R_{\text{coil}} = \frac{\rho N C_{\text{coil}}}{a_{\text{wire}}} = 3.6 \times 10^{-4} \ \Omega. \tag{5.22}$$

To summarize the magnet design, in Fig. 5.13, we show the focusing of particles with $E_k = 50$ keV by using the doublet and bending magnet. It can be seen that a parallel electron beam with an initial diameter of 2 μm can be focused along the optical axis, which is the trajectory of the reference particles.

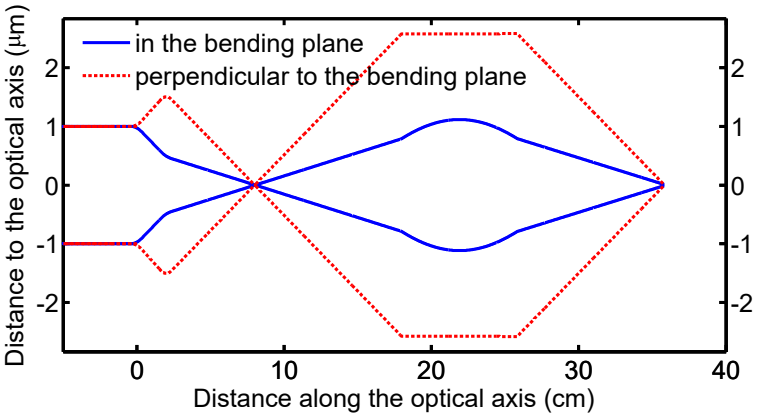

FIGURE 5.13: Focusing of particles with the doublet and bending magnet.

5.4 Current status

All the components for the experiment have been fabricated. Figure 5.14 shows several photos of the fabricated components, including a high-voltage insulator, vacuum chamber, anodes for the electron gun, doublet and magnetic sector on a base plate.

A Yb laser system which provides laser pulses for the experiment is almost done. It will drive both the photocathode and DLA structure. The system mainly consists of a Yb-doped fiber oscillator, three Yb-doped fiber pre-amplifiers, and three Yb:YAG thin-disk amplifiers. Figure 5.15(a) shows the flow diagram of the laser system. Figure 5.15(b) shows a photograph of the Yb fiber laser. The output beam of the last Yb:YAG thin-disk amplifier is shown in Fig. 5.15(c), with a pulse duration of ~ 50 ps, a pulse energy of 15 mJ, and a repetition rate of 20 Hz. A grating compressor is being developed to realize a shorter pulse duration, which is necessary for high-gradient acceleration. The

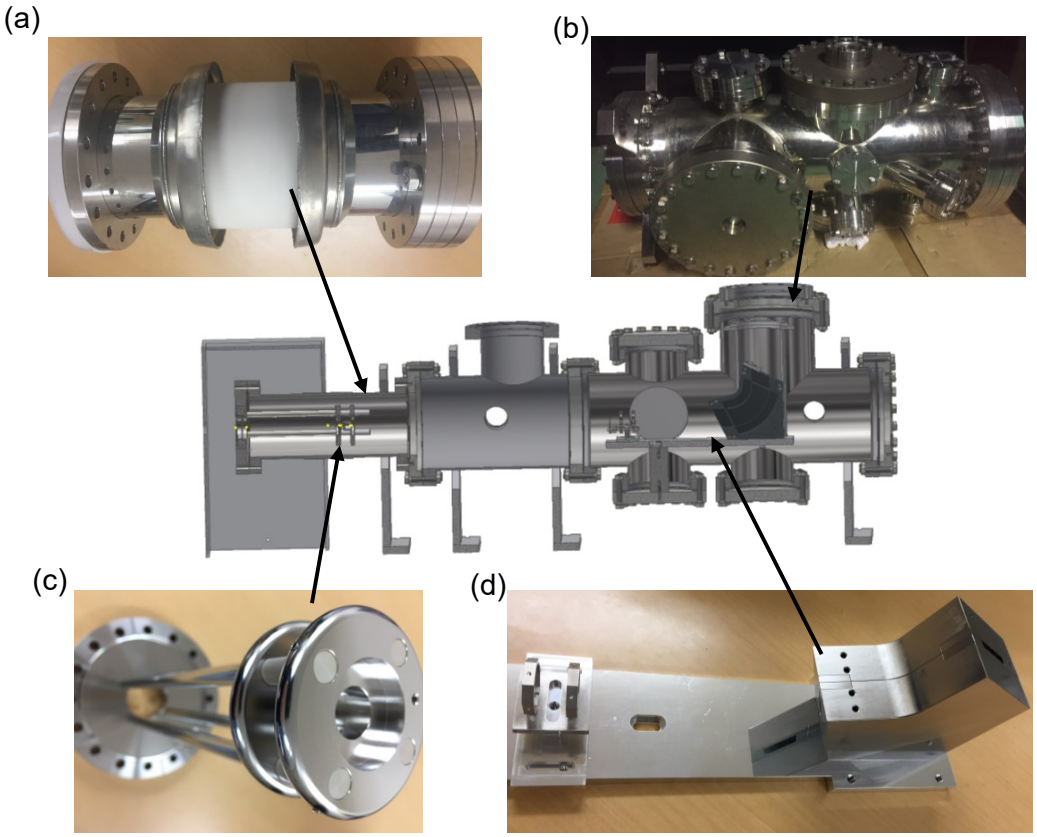

FIGURE 5.14: Fabricated components for the experiment. (a) High-voltage insulator. (b) Vacuum chamber. (c) Anodes. (d) Quadrupole doublet and magnetic sector on a base plate.

compressed beam will be split into two; one is used to drive the DLA structure, the other is used to drive the photocathode after frequency doubling. A translation stage is used to adjust the optical path length to the DLA structure to ensure the temporal alignment of the electron beam and the laser for DLA structure.

In order to produce an electron beam of high quality, a one-dimensional nano-scale photocathode with back-illumination was provided by KEK. It consists of a gold thin film, as the emitter, on a glass substrate with a titanium adhesion layer. Figure 5.16(a) shows a photograph of the photocathode. Figure 5.16(b) shows the current density as a function of laser intensity measured by T. Shibuya.

To summarize, a test station for DLA structures has been designed and fabricated. The expected experiment parameters based on the design are listed in Table 5.1. A Yb laser system is being developed to provide laser pulses. Once the laser is ready, experiments, including the damage test of the dielectric material, electron beam production, dielectric laser acceleration, will be conducted.

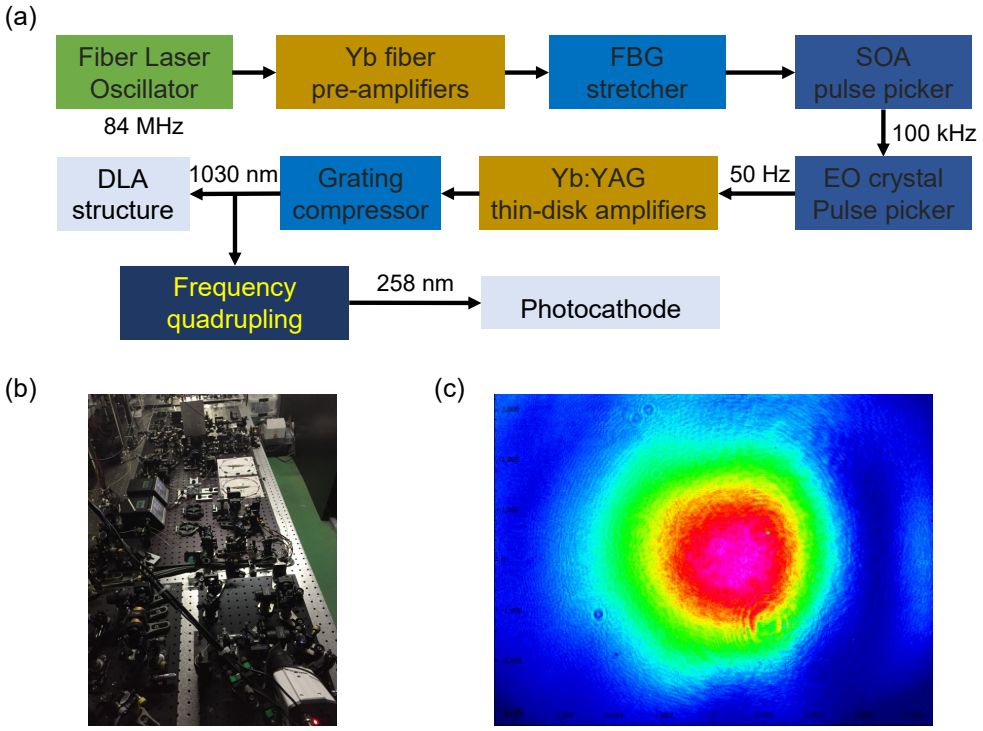

FIGURE 5.15: Flow diagram (a), photograph(b), and output beam profile (c) of the Yb laser system. The profile is measured after the last Yb:YAG thin-disk amplifier by a CCD camera beam profiler (Thorlabs BC106N-VIS).

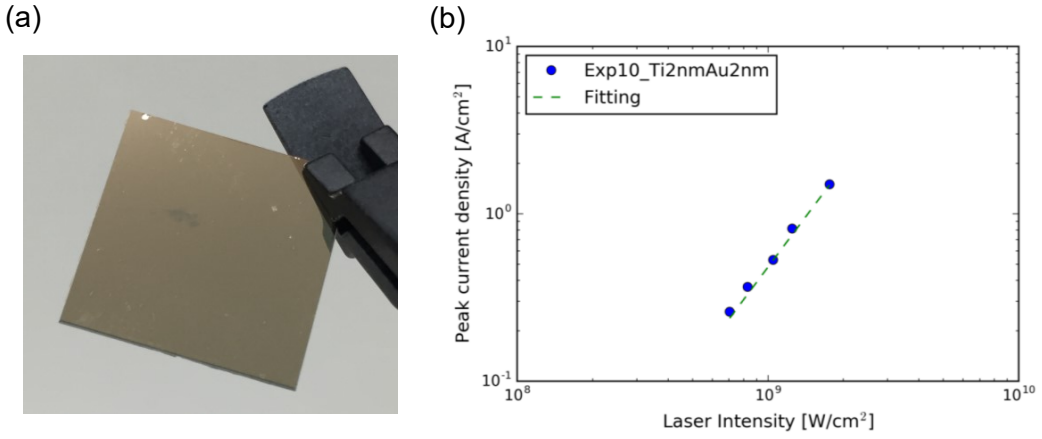

FIGURE 5.16: Photograph of the photocathode (a) and the measured current density as a function of the laser intensity (b). The cathode is measured with a ultraviolet laser with a beam diameter of 13 μm. Figure (b) is taken from [83].

Table 5.1: Expected experiment parameters.

Electron beam	
Electron energy $E_{\mathrm{k},0}$	50 keV
Energy spread δ_{E}	$< 0.1\%$
Emittance ϵ_x/ϵ_y	$< 10 \times 10^{-3}$ mm $\cdot$ mrad
Laser pulse	
Wavelength λ	1030 nm
Pulse energy E_{l}	5.7 μJ
Pulse duration τ_{p}	30 ps
Spot size σ_x/σ_y	10 μm
Peak intensity E_0	1.2×10^{11} W/cm^2
Peak field I_0	0.92 GV/m
Acceleration	
Max acc. gradient G_{a}	$\sim$ 60 MV/m
Max energy gain δ_{E}	$\sim$ 1 keV/m

Chapter 6

Conclusion and outlook

Dielectric laser accelerator has a great potential to make particle accelerators more compact and more affordable by utilizing the high damage threshold of dielectrics at optical frequencies. Its capability of delivering a nanometer-sized beam with attosecond pulse duration makes it a perfect platform for radiobiology research. After the recent success of DLA experiments in Stanford University and Max Planck Institute of Quantum Optics/Friedrich Alexander University Erlangen-Nuremberg using diffraction gratings, the question remains of how to optimize the DLA structures to more efficiently accelerate a particle beam.

In this dissertation, we have presented a general method to design a double-grating resonator for subrelativistic electron acceleration. The underlying idea is to merge diffraction gratings with resonating Fabry-Perot cavities. We described how to generate a hyperbolic cosine accelerating mode by exciting the first diffraction order on either side of a double-grating structure. We introduced how to produce an enhanced accelerating mode with a single-sided illumination by designing highly-reflective gratings to form a Fabry-Perot cavity for the zeroth diffraction order. Thus, a laser-power efficient way of electron acceleration may be enabled. Using this method, a mm-scale DLA can accelerate electrons from 50 keV to 1 MeV. This method considers the optimization of double-grating structures in a more rigorous analytical and computational form than prior works. Additionally, it helps to bridge a gap between the theory and experiments by considering a single-sided illumination of a double grating, in contrast with prior analytical treatments that assumed symmetric dual-sided illumination of the gratings.

We have also described a general procedure to design a planar accelerating waveguide using highly-reflective gratings as mirrors. We found the solution to support an accelerating mode with a given phase velocity by designing a matching layer. Compared with the waveguides using photonic crystals, using a single-layer grating to confine the mode

could drastically reduce the transverse size. It could also enable more straightforward fabrication and easier integration.

We have also shown the progress in developing a test station for DLA structures. We described our design of the experiment, particularly the magnets. We estimated the sustainable gradient of the fabricated single-grating structure. All the components have been fabricated to date.

To realize a DLA-based electron source for radiobiology research, there are many bridges to cross. One important step is to develop a DLA-compatible emitter, which could produce an electron beam with small spot size. The realization of optical microbunching represents another important next step, in which multi-stage subrelativistic electron acceleration could be a challenge. Following that, net acceleration of bunched electrons should be realized, where focusing elements will be needed to control the beam size. All these steps could lead to a millimeter-scale DLA electron source that can accelerate electrons to the target MeV energy.

Appendix A

Appendix Rigorous coupled-wave analysis for simulation

Rigorous coupled wave analysis (RCWA) is a widely used differential method to calculate scattering from gratings[84]. This approach is to obtain an exact solution of Maxwell's equations by implementing the Fourier expansions of the fields and grating permittivity along the directions of the periodicities; thus, it allows one to treat a wide class of gratings (planar gratings[84–87], surface-relief gratings[88, 89], crossed-grating structures[90]) in a unified way. The accuracy of the solution depends solely on the number of spatial harmonics retained in the expansion after truncation. In the following, we will implement the RCWA method for DLA double-grating structure as shown in Fig. A.1.

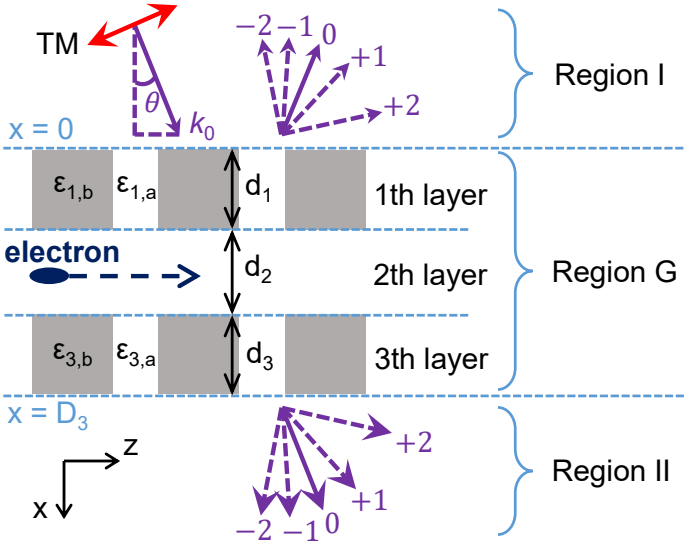

FIGURE A.1: Schematic of a dual-grating structure for dielectric laser acceleration.

A.0.1 Fourier expansion of the fields

To begin with, we describe the fields outside the grating as the superposition of a series of diffraction orders. The fields in region I can be written as

$$H_y^{\mathrm{I}} = \mathrm{e}^{\mathrm{i}k_{\mathrm{I}}(x\cos\theta+z\sin\theta)} + \sum_{n=-\infty}^{\infty} r_n \mathrm{e}^{\mathrm{i}\left(-k_{\mathrm{I},x,n}x+k_{z,n}z\right)}, \tag{A.1}$$

$$E_z^{\mathrm{I}} = -\frac{\cos\theta}{n_{\mathrm{I}}}\sqrt{\frac{\mu_0}{\varepsilon_0}}\mathrm{e}^{\mathrm{i}k_{\mathrm{I}}(x\cos\theta+z\sin\theta)} + \sum_{n=-\infty}^{\infty} \frac{k_{\mathrm{I},x,n}r_n}{k_0\varepsilon_{\mathrm{I},r}}\sqrt{\frac{\mu_0}{\varepsilon_0}}\mathrm{e}^{\mathrm{i}\left(-k_{\mathrm{I},x,n}x+k_{z,n}z\right)}, \tag{A.2}$$

$$E_x^{\mathrm{I}} = \frac{\sin\theta}{n_{\mathrm{I}}}\sqrt{\frac{\mu_0}{\varepsilon_0}}\mathrm{e}^{\mathrm{i}k_{\mathrm{I}}(x\cos\theta+z\sin\theta)} + \sum_{n=-\infty}^{\infty} \frac{k_{z,n}r_n}{k_0\varepsilon_{\mathrm{I},r}}\sqrt{\frac{\mu_0}{\varepsilon_0}}\mathrm{e}^{\mathrm{i}\left(-k_{\mathrm{I},x,n}x+k_{z,n}z\right)}. \tag{A.3}$$

The fields in region II can be written as

$$H_y^{\mathrm{II}} = \sum_{n=-\infty}^{\infty} t_n \mathrm{e}^{\mathrm{i}\left(k_{\mathrm{II},x,n}(x-D_L)+k_{z,n}z\right)}, \quad D_L = \sum_{p=1}^{L} d_p \tag{A.4}$$

$$E_z^{\mathrm{II}} = -\sum_{n=-\infty}^{\infty} \frac{k_{\mathrm{II},x,n}t_n}{k_0\varepsilon_{\mathrm{II},r}}\sqrt{\frac{\mu_0}{\varepsilon_0}}\mathrm{e}^{\mathrm{i}\left(k_{\mathrm{II},x,n}(x-D_l)+k_{z,n}z\right)}, \tag{A.5}$$

$$E_x^{\mathrm{II}} = \sum_{n=-\infty}^{\infty} \frac{k_{z,n}t_n}{k_0\varepsilon_{\mathrm{II},r}}\sqrt{\frac{\mu_0}{\varepsilon_0}}\mathrm{e}^{\mathrm{i}\left(k_{\mathrm{II},x,n}(x-D_l)+k_{z,n}z\right)}, \tag{A.6}$$

where d_l represents the thickness of the lth layer as shown in Fig. A.1, L represents the number of the last layer, or the total number of the layers.

The grating is treated as a stack of layers which consists of alternating regions of relative permittivity $\varepsilon_{l,\mathrm{p}}$ (pillar) and $\varepsilon_{l,\mathrm{g}}$ (groove). By using the Fourier expansion method which is introduced in Sec. 2.1, the magnetic field in the lth layer ($D_l - d_l < x < D_l = \sum_{p=1}^{l} d_p$) can be written as

$$H_{y,l}^{\mathrm{G}}(x,z) = \sum_{n=-\infty}^{+\infty} f_{l,n}^{\mathrm{G}}(x)\mathrm{e}^{\mathrm{i}k_{z,n}z}. \tag{A.7}$$

Based on the relation described in Eq. 2.7, the electric fields can be given by Eq. A.8 and A.9.

$$\begin{aligned} E_{z,l}^{\mathrm{G}}(x,z) &= \mathrm{i}\frac{1}{k_0}\sqrt{\frac{\mu_0}{\varepsilon_0}}\frac{1}{\varepsilon_l(z)}\frac{\partial H_{y,l}^{\mathrm{G}}(x,z)}{\partial x} \\ &= \mathrm{i}\frac{1}{k_0}\sqrt{\frac{\mu_0}{\varepsilon_0}}\sum_{h=-\infty}^{+\infty}\alpha_{l,h}\mathrm{e}^{\mathrm{i}h\frac{2\pi}{\Lambda}z}\sum_{n=-\infty}^{+\infty}\frac{\partial f_{l,n}^{\mathrm{G}}(x)}{\partial x}\mathrm{e}^{\mathrm{i}k_{z,n}z} \\ &= \mathrm{i}\frac{1}{k_0}\sqrt{\frac{\mu_0}{\varepsilon_0}}\sum_{h=-\infty}^{+\infty}\left[\sum_{n=-\infty}^{+\infty}\alpha_{l,h-n}\frac{\partial f_{l,n}^{\mathrm{G}}(x)}{\partial x}\right]\mathrm{e}^{\mathrm{i}k_{z,h}z}, \end{aligned} \tag{A.8}$$

$$\begin{aligned} E_{x,l}^{\mathrm{G}}(x,z) &= -\mathrm{i}\frac{1}{k_0}\sqrt{\frac{\mu_0}{\varepsilon_0}}\frac{1}{\varepsilon_l(z)}\frac{\partial H_{y,l}^{\mathrm{G}}(x,z)}{\partial z} \\ &= \frac{1}{k_0}\sqrt{\frac{\mu_0}{\varepsilon_0}}\sum_{h=-\infty}^{+\infty}\alpha_{l,h}\mathrm{e}^{\mathrm{i}h\frac{2\pi}{\Lambda}z}\sum_{n=-\infty}^{+\infty}k_{z,n}f_{l,n}^{\mathrm{G}}(x)\mathrm{e}^{\mathrm{i}k_{z,n}z} \\ &= \frac{1}{k_0}\sqrt{\frac{\mu_0}{\varepsilon_0}}\sum_{h=-\infty}^{+\infty}\left[\sum_{n=-\infty}^{+\infty}\alpha_{l,h-n}k_{z,n}f_{l,n}^{\mathrm{G}}(x)\right]\mathrm{e}^{\mathrm{i}k_{z,h}z}. \end{aligned} \tag{A.9}$$

In this case, the permittivity in each layer depends only on the position z, i.e., the relative permittivity $\varepsilon_r \equiv \varepsilon_l(z)$. In the lth layer of thicknes d_l, the periodic $\varepsilon_l(z)$ is expandable in a Fourier series as

$$\varepsilon_l(z) = \sum_{h=-\infty}^{+\infty}\widehat{\epsilon}_{l,h}\mathrm{e}^{\mathrm{i}h\frac{2\pi}{\Lambda}(z-z_{l,0})}, \qquad D_l - d_l < x < D_l = \sum_{p=1}^{l} d_p, \tag{A.10}$$

where $\widehat{\epsilon}_{l,h}$ is the hth Fourier component of the relative permittivity in the lth layer,

$$\widehat{\epsilon}_{l,h}(h=0) = \varepsilon_{l,\mathrm{g}} + (\varepsilon_{l,\mathrm{p}} - \varepsilon_{l,\mathrm{g}})\eta_l, \qquad \widehat{\epsilon}_{l,h}(h\neq 0) = (\varepsilon_{l,\mathrm{p}} - \varepsilon_{l,\mathrm{g}})\frac{\sin(\pi h\eta_l)}{\pi h}. \tag{A.11}$$

Here, $z_{l,0}$ is used to shift the grating in the z-direction, e.g., $z_{l,0} = 0$ represents that the groove is located at the center, while $z_{l,0} = \Lambda/2$ represents that the pillar is located at the center. Throughout the report, we use $z_{l,0} = \Lambda/2$. η_l is the duty cycle, i.e., the fraction of the grating period occupied by the pillar of permittivity $\varepsilon_{l,\mathrm{p}}$. For simplicity, we consider the following scaling

$$\varepsilon_l(z) = \sum_{h=-\infty}^{+\infty}\epsilon_{l,h}\mathrm{e}^{\mathrm{i}h\frac{2\pi}{\Lambda}z}, \qquad D_l - d_l < x < D_l = \sum_{p=1}^{l} d_p, \tag{A.12}$$

where

$$\epsilon_{l,h}(h=0) = \widehat{\epsilon}_{l,h}\mathrm{e}^{-\mathrm{i}h\frac{2\pi}{\Lambda}z_{l,0}} = \varepsilon_{l,\mathrm{g}} + (\varepsilon_{l,\mathrm{p}} - \varepsilon_{l,\mathrm{g}})\eta_l, \tag{A.13}$$

$$\epsilon_{l,h}(h\neq 0) = \widehat{\epsilon}_{l,h}\mathrm{e}^{-\mathrm{i}h\frac{2\pi}{\Lambda}z_{l,0}} = (\varepsilon_{l,\mathrm{p}} - \varepsilon_{l,\mathrm{g}})\frac{\sin(\pi h\eta_l)}{\pi h}\mathrm{e}^{-\mathrm{i}h\frac{2\pi}{\Lambda}z_{l,0}}. \tag{A.14}$$

Similarly, $1/\varepsilon_l(z)$ can also be expressed in a Fourier series as

$$\frac{1}{\varepsilon_l(z)} = \sum_{h=-\infty}^{+\infty}\alpha_{l,h}\mathrm{e}^{\mathrm{i}h\frac{2\pi}{\Lambda}z}, \qquad D_l - d_l < x < D_l = \sum_{p=1}^{l} d_p, \tag{A.15}$$

where $\alpha_{l,h}$ is the hth Fourier component of $1/\varepsilon_l(z)$ in the lth layer,

$$\alpha_{l,h}(h=0)=\frac{1}{\varepsilon_{l,\mathrm{g}}}+(\frac{1}{\varepsilon_{l,\mathrm{p}}}-\frac{1}{\varepsilon_{l,\mathrm{g}}})\eta_l,\qquad \alpha_{l,h}(h\neq 0)=(\frac{1}{\varepsilon_{l,\mathrm{p}}}-\frac{1}{\varepsilon_{l,\mathrm{g}}})\frac{\sin(\pi h\eta_l)}{\pi h}\mathrm{e}^{-\mathrm{i}h\frac{2\pi}{\Lambda}z_{l,0}}. \tag{A.16}$$

Based on Eq. A.12 and Eq. A.15, Eq. 2.6 can be rewritten as

$$\begin{aligned}&\frac{\mathrm{d}^2}{\mathrm{d}x^2}\sum_{m=-\infty}^{+\infty}f_{l,m}^{\mathrm{G}}(x)\mathrm{e}^{\mathrm{i}k_{z,m}z}\\&=\sum_{m=-\infty}^{+\infty}\left[\sum_{j=-\infty}^{+\infty}\epsilon_{l,m-j}k_{z,j}\left(\sum_{n=-\infty}^{+\infty}\alpha_{l,j-n}k_{z,n}f_{l,n}^{\mathrm{G}}(x)\right)\right]\mathrm{e}^{\mathrm{i}k_{z,m}z}\\&\quad-k_0^2\sum_{m=-\infty}^{+\infty}\left(\sum_{n=-\infty}^{+\infty}\epsilon_{l,m-n}f_{l,n}^{\mathrm{G}}(x)\right)\mathrm{e}^{\mathrm{i}k_{z,m}z}.\end{aligned} \tag{A.17}$$

Equating for the mth component yields

$$\frac{\mathrm{d}^2f_{l,m}^{\mathrm{G}}(x)}{\mathrm{d}x^2}=\sum_{j=-\infty}^{+\infty}\epsilon_{l,m-j}k_{z,j}\left(\sum_{n=-\infty}^{+\infty}\alpha_{l,j-n}k_{z,n}f_{l,n}^{\mathrm{G}}(x)\right)-k_0^2\left(\sum_{n=-\infty}^{+\infty}\epsilon_{l,m-n}f_{l,n}^{\mathrm{G}}(x)\right) \tag{A.18}$$

With the scaling $x'=k_0x$, Eq. A.18 can be rewritten as

$$\frac{\mathrm{d}^2f_{l,m}^{\mathrm{G}}(x')}{\mathrm{d}(x')^2}=\sum_{j=-\infty}^{+\infty}\epsilon_{l,m-j}\frac{k_{z,j}}{k_0}\left(\sum_{n=-\infty}^{+\infty}\alpha_{l,j-n}\frac{k_{z,n}}{k_0}f_{l,n}^{\mathrm{G}}(x')\right)-\sum_{n=-\infty}^{+\infty}\epsilon_{l,m-n}f_{l,n}^{\mathrm{G}}(x') \tag{A.19}$$

A.0.2 Truncation of the Fourier expansion

In numerical analysis, the infinite Fourier expansion needs to be truncated. In the rest of the text, we will calculate the fields with a truncation order of N.

After truncation, the truncated Fourier expansions of the fields in region I are given by

$$H_y^{\mathrm{I}}=\mathrm{e}^{\mathrm{i}k_{\mathrm{I}}(x\cos\theta+z\sin\theta)}+\sum_{n=-N}^{N}r_n\mathrm{e}^{\mathrm{i}\left(-k_{\mathrm{I},x,n}x+k_{z,n}z\right)}, \tag{A.20}$$

$$E_z^{\mathrm{I}}=-\frac{\cos\theta}{n_{\mathrm{I}}}\sqrt{\frac{\mu_0}{\varepsilon_0}}\mathrm{e}^{\mathrm{i}k_{\mathrm{I}}(x\cos\theta+z\sin\theta)}+\sum_{n=-N}^{N}\frac{k_{\mathrm{I},x,n}r_n}{k_0\varepsilon_{\mathrm{I},r}}\sqrt{\frac{\mu_0}{\varepsilon_0}}\mathrm{e}^{\mathrm{i}\left(-k_{\mathrm{I},x,n}x+k_{z,n}z\right)}, \tag{A.21}$$

$$E_x^{\mathrm{I}}=\frac{\sin\theta}{n_{\mathrm{I}}}\sqrt{\frac{\mu_0}{\varepsilon_0}}\mathrm{e}^{\mathrm{i}k_{\mathrm{I}}(x\cos\theta+z\sin\theta)}+\sum_{n=-N}^{N}\frac{k_{z,n}r_n}{k_0\varepsilon_{\mathrm{I},r}}\sqrt{\frac{\mu_0}{\varepsilon_0}}\mathrm{e}^{\mathrm{i}\left(-k_{\mathrm{I},x,n}x+k_{z,n}z\right)}, \tag{A.22}$$

or, in matrix form,

$$H_y^{\mathrm{I}} = \mathrm{e}^{\mathrm{i}\mathbf{k}_z z}\left\{\mathrm{diag}\left[\mathrm{diag}\left(\mathrm{e}^{\mathrm{i}\mathbf{K}_{\mathrm{I},x}x'}\right)\right]\boldsymbol{\Gamma}_0 + \mathrm{diag}\left[\mathrm{diag}\left(\mathrm{e}^{-\mathrm{i}\mathbf{K}_{\mathrm{I},x}x'}\right)\right]\mathbf{R}\right\}, \tag{A.23}$$

$$\begin{aligned} E_z^{\mathrm{I}} &= \sqrt{\frac{\mu_0}{\varepsilon_0}}\mathrm{e}^{\mathrm{i}\mathbf{k}_z z}\left\{-\frac{\cos\theta}{n_{\mathrm{I}}}\mathrm{diag}\left[\mathrm{diag}\left(\mathrm{e}^{\mathrm{i}\mathbf{K}_{\mathrm{I},x}x'}\right)\right]\boldsymbol{\Gamma}_0 + \frac{1}{\varepsilon_{\mathrm{I},r}}\mathbf{K}_{\mathrm{I},x}\mathrm{diag}\left[\mathrm{diag}\left(\mathrm{e}^{-\mathrm{i}\mathbf{K}_{\mathrm{I},x}x'}\right)\right]\mathbf{R}\right\} \\ &= \frac{1}{\varepsilon_{\mathrm{I},r}}\sqrt{\frac{\mu_0}{\varepsilon_0}}\mathrm{e}^{\mathrm{i}\mathbf{k}_z z}\left\{-\mathbf{K}_{\mathrm{I},x}\mathrm{diag}\left[\mathrm{diag}\left(\mathrm{e}^{\mathrm{i}\mathbf{K}_{\mathrm{I},x}x'}\right)\right]\boldsymbol{\Gamma}_0 + \mathbf{K}_{\mathrm{I},x}\mathrm{diag}\left[\mathrm{diag}\left(\mathrm{e}^{-\mathrm{i}\mathbf{K}_{\mathrm{I},x}x'}\right)\right]\mathbf{R}\right\}, \end{aligned} \tag{A.24}$$

$$\begin{aligned} E_x^{\mathrm{I}} &= \sqrt{\frac{\mu_0}{\varepsilon_0}}\mathrm{e}^{\mathrm{i}\mathbf{k}_z z}\left\{\frac{\sin\theta}{n_{\mathrm{I}}}\mathrm{diag}\left[\mathrm{diag}\left(\mathrm{e}^{\mathrm{i}\mathbf{K}_{\mathrm{I},x}x'}\right)\right]\boldsymbol{\Gamma}_0 + \frac{1}{\varepsilon_{\mathrm{I},r}}\mathbf{K}_z\mathrm{diag}\left[\mathrm{diag}\left(\mathrm{e}^{-\mathrm{i}\mathbf{K}_{\mathrm{I},x}x'}\right)\right)\mathbf{R}\right\} \\ &= \frac{1}{\varepsilon_{\mathrm{I},r}}\sqrt{\frac{\mu_0}{\varepsilon_0}}\mathrm{e}^{\mathrm{i}\mathbf{k}_z z}\left(\mathbf{K}_z\mathrm{diag}\left[\mathrm{diag}\left(\mathrm{e}^{\mathrm{i}\mathbf{K}_{\mathrm{I},x}x'}\right)\right]\boldsymbol{\Gamma}_0 + \mathbf{K}_z\mathrm{diag}\left[\mathrm{diag}\left(\mathrm{e}^{-\mathrm{i}\mathbf{K}_{\mathrm{I},x}x'}\right)\right]\mathbf{R}\right). \end{aligned} \tag{A.25}$$

where

$$\mathbf{k}_z = [k_{z,-N}, \cdots, k_{z,-N}] \in \mathbb{C}^{1\times(2N+1)}, \tag{A.26}$$

$$\mathbf{K}_z = \mathrm{diag}(k_{z,n}/k_0) \in \mathbb{C}^{(2N+1)\times(2N+1)}, \tag{A.27}$$

$$\mathbf{K}_{\mathrm{I},x} = \mathrm{diag}(k_{\mathrm{I},x,n}/k_0) \in \mathbb{C}^{(2N+1)\times(2N+1)}, \tag{A.28}$$

$$\boldsymbol{\Gamma}_0 = [0, \cdots, 0, 1, 0, \cdots, 0]^{\mathrm{T}} \in \mathbb{C}^{(2N+1)\times 1}, \tag{A.29}$$

$$\mathbf{R} = [r_{-N}, \cdots, r_0, \cdots, r_N]^{\mathrm{T}} \in \mathbb{C}^{(2N+1)\times 1}. \tag{A.30}$$

The truncated Fourier expansions of the fields in region II are given by

$$H_y^{\mathrm{II}} = \sum_{n=-N}^{N} t_n \mathrm{e}^{\mathrm{i}\left(k_{\mathrm{II},x,n}(x-D_L)+k_{z,n}z\right)}, \tag{A.31}$$

$$E_z^{\mathrm{II}} = -\sum_{n=-N}^{N} \frac{k_{\mathrm{II},x,n}t_n}{k_0\varepsilon_{\mathrm{II},r}}\sqrt{\frac{\mu_0}{\varepsilon_0}}\mathrm{e}^{\mathrm{i}\left(k_{\mathrm{II},x,n}(x-D_L)+k_{z,n}z\right)}, \tag{A.32}$$

$$E_x^{\mathrm{II}} = \sum_{n=-N}^{N} \frac{k_{z,n}t_n}{k_0\varepsilon_{\mathrm{II},r}}\sqrt{\frac{\mu_0}{\varepsilon_0}}\mathrm{e}^{\mathrm{i}\left(k_{\mathrm{II},x,n}(x-D_L)+k_{z,n}z\right)}, \tag{A.33}$$

or, in the matrix form,

$$H_y^{\mathrm{II}} = \mathrm{e}^{\mathrm{i}\mathbf{k}_z z}\mathrm{diag}\left[\mathrm{diag}\left(\mathrm{e}^{\mathrm{i}\mathbf{K}_{\mathrm{II},x}(x'-k_0D_L)}\right)\right]\mathbf{T}, \tag{A.34}$$

$$E_z^{\mathrm{II}} = -\frac{1}{\varepsilon_{\mathrm{II},r}}\sqrt{\frac{\mu_0}{\varepsilon_0}}\mathrm{e}^{\mathrm{i}\mathbf{k}_z z}\mathbf{K}_{\mathrm{II},x}\mathrm{diag}\left[\mathrm{diag}\left(\mathrm{e}^{\mathrm{i}\mathbf{K}_{\mathrm{II},x}(x'-k_0D_L)}\right)\right]\mathbf{T}, \tag{A.35}$$

$$E_x^{\mathrm{II}} = \frac{1}{\varepsilon_{\mathrm{II},r}}\sqrt{\frac{\mu_0}{\varepsilon_0}}\mathrm{e}^{\mathrm{i}\mathbf{k}_z z}\mathbf{K}_z\mathrm{diag}\left[\mathrm{diag}\left(\mathrm{e}^{\mathrm{i}\mathbf{K}_{\mathrm{II},x}(x'-k_0D_L)}\right)\right]\mathbf{T}, \tag{A.36}$$

where

$$\mathbf{K}_{\mathrm{II},x} = \mathrm{diag}(k_{\mathrm{I},x,n}/k_0) \in \mathbb{C}^{(2N+1)\times(2N+1)}, \tag{A.37}$$

$$\mathbf{T} = [t_{-N}, \cdots, t_0, \cdots, t_N]^{\mathrm{T}} \in \mathbb{C}^{(2N+1)\times 1}. \tag{A.38}$$

Based on Eqs. A.7–A.9, the truncated Fourier expansions of the fields in the lth layer of region G can be given by

$$H_{y,l}^{\mathrm{G}}(x,z) = \sum_{n=-N}^{N} f_{l,n}^{\mathrm{G}}(x') \mathrm{e}^{\mathrm{i}k_{z,n}z}, \tag{A.39}$$

$$E_{z,l}^{\mathrm{G}}(x,z) = \mathrm{i}\sqrt{\frac{\mu_0}{\varepsilon_0}} \sum_{h=-N}^{N} \left[\sum_{n=-N}^{N} \alpha_{l,h-n} \frac{\partial f_{l,n}^{\mathrm{G}}(x')}{\partial(x')} \right] \mathrm{e}^{\mathrm{i}k_{z,h}z}, \tag{A.40}$$

$$E_{x,l}^{\mathrm{G}}(x,z) = \frac{1}{k_0}\sqrt{\frac{\mu_0}{\varepsilon_0}} \sum_{h=-N}^{N} \left[\sum_{n=-N}^{N} \alpha_{l,h-n} k_{z,n} f_{l,n}^{\mathrm{G}}(x) \right] \mathrm{e}^{\mathrm{i}k_{z,h}z}, \tag{A.41}$$

or, in the matrix form,

$$H_{y,l}^{\mathrm{G}}(x,z) = \mathrm{e}^{\mathrm{i}\mathbf{k}_z z}\mathbf{U}_l(x), \tag{A.42}$$

$$E_{z,l}^{\mathrm{G}}(x,z) = \mathrm{i}\sqrt{\frac{\mu_0}{\varepsilon_0}}\mathrm{e}^{\mathrm{i}\mathbf{k}_z z}\mathbf{S}_l(x), \tag{A.43}$$

$$E_{x,l}^{\mathrm{G}}(x,z) = \sqrt{\frac{\mu_0}{\varepsilon_0}}\mathrm{e}^{\mathrm{i}\mathbf{k}_z z}\boldsymbol{\Upsilon}_l\mathbf{K}_z\mathbf{U}_l(x), \tag{A.44}$$

where

$$\mathbf{U}_l(x) = \left[f_{l,-N}^{\mathrm{G}}(x), \cdots, f_{l,0}^{\mathrm{G}}(x), \cdots, f_{l,N}^{\mathrm{G}}(x)\right]^{\mathrm{T}} \in \mathbb{C}^{(2N+1)\times 1}, \tag{A.45}$$

$$\mathbf{S}_l(x) = \left[s_{l,-N}^{\mathrm{G}}(x), \cdots, s_{l,0}^{\mathrm{G}}(x), \cdots, s_{l,N}^{\mathrm{G}}(x)\right]^{\mathrm{T}} \in \mathbb{C}^{(2N+1)\times 1}. \tag{A.46}$$

$$\boldsymbol{\Upsilon}_l = \left[\!\left[\frac{1}{\varepsilon_l}\right]\!\right]^{(N)} \in \mathbb{C}^{(2N+1)\times(2N+1)}, \qquad \left[\!\left[\frac{1}{\varepsilon_l}\right]\!\right]_{mn}^{(N)} = \alpha_{l,m-n}. \tag{A.47}$$

Here, the relation between the tangential magnetic field and the tangential electric field can be given by

$$\mathbf{S}_l(x) = \Upsilon_l \frac{\partial \mathbf{U}_l(x)}{\partial(x')}. \tag{A.48}$$

The truncated form of Eq. A.19 is given by

$$\frac{\mathrm{d}^2 f_{l,m}^{\mathrm{G}}(x')}{\mathrm{d}(x')^2} = \sum_{j=-N}^{N} \epsilon_{l,m-j} \frac{k_{z,j}}{k_0} \left(\sum_{n=-N}^{N} \alpha_{l,j-n} \frac{k_{z,n}}{k_0} f_{l,n}^{\mathrm{G}}(x') \right) - \sum_{n=-N}^{N} \epsilon_{l,m-n} f_{l,n}^{\mathrm{G}}(x'), \tag{A.49}$$

or, in the matrix form,

$$\left[\mathrm{d}^2\mathbf{U}_l(x)/\mathrm{d}(x')^2\right] = \mathbf{E}\left[\mathbf{K}_z\boldsymbol{\Upsilon}\mathbf{K}_z - \mathbf{I}\right]\mathbf{U}_l(x) = \mathbf{E}\mathbf{G}\mathbf{U}_l(x), \tag{A.50}$$

where $\mathbf{I}$ is the unit matrix, $\mathbf{G} = \mathbf{K}_z\boldsymbol{\Upsilon}\mathbf{K}_z - \mathbf{I}$, and

$$\mathbf{E}_l = [\![\varepsilon_l]\!]^{(N)} \in \mathbb{C}^{(2N+1)\times(2N+1)}, \qquad [\![\varepsilon_l]\!]^{(N)}_{mn} = \epsilon_{l,m-n}. \tag{A.51}$$

A general solution of Eq. A.50 is given by

$$f^{\mathrm{G}}_{l,m} = \sum_{n=-N}^{N} w_{l,m,n}\left\{c^{+}_{l,n}\mathrm{e}^{k_0 q_{l,n}[x-D_l]} + c^{-}_{l,n}\mathrm{e}^{-k_0 q_{l,n}[x-(D_l-d_l)]}\right\}, \tag{A.52}$$

$$s^{\mathrm{G}}_{l,m} = \sum_{j=-N}^{N}\left\{\alpha_{l,m-j}\sum_{n=-N}^{N} w_{l,j,n}\left\{q_{l,n}c^{+}_{l,n}\mathrm{e}^{k_0 q_{l,n}[x-D_l]} - q_{l,n}c^{-}_{l,n}\mathrm{e}^{-k_0 q_{l,n}[x-(D_l-d_l)]}\right\}\right\}, \tag{A.53}$$

or, in the matrix form,

$$\mathbf{U}_l(x) = \mathbf{W}_l\left[\mathbf{Y}^{+}_l(x)\mathbf{C}^{+}_l + \mathbf{Y}^{-}_l(x)\mathbf{C}^{-}_l\right], \tag{A.54}$$

$$\mathbf{S}_l(x) = \boldsymbol{\Upsilon}_l\mathbf{W}_l\mathbf{Q}_l\left[\mathbf{Y}^{+}_l(x)\mathbf{C}^{+}_l - \mathbf{Y}_{\mathrm{I}}{}^{-}(x)\mathbf{C}^{-}_l\right] = \mathbf{V}_l\left[\mathbf{Y}^{+}_l(x)\mathbf{C}^{+}_l - \mathbf{Y}^{-}_l(x)\mathbf{C}^{-}_l\right], \tag{A.55}$$

where, $w_{l,m,n} = (\mathbf{W}_l)_{mn}$, with $\mathbf{W}_l \in \mathbb{C}^{(2N+1)\times(2N+1)}$ is the eigenvector matrix of the matrix $\mathbf{EG}$, $\mathbf{Q}_l = \mathrm{diag}(q_{l,m}) \in \mathbb{C}^{(2N+1)\times(2N+1)}$, with $q_{l,m}$ being the square root of the eigenvalues of the matrix $\mathbf{EG}$, $\mathbf{Y}^{+}_l(x) = \mathrm{diag}(\mathrm{e}^{k_0 q_{l,n}[x-D_l]}) \in \mathbb{C}^{(2N+1)\times(2N+1)}$, $\mathbf{Y}^{-}_l(x) = \mathrm{diag}(\mathrm{e}^{-k_0 q_{l,n}[x-(D_l-d_l)]}) \in \mathbb{C}^{(2N+1)\times(2N+1)}$, $\mathbf{C}^{+}_l = \left[c^{+}_{l,-N},\cdots,c^{+}_{l,0},\cdots,c^{+}_{l,N}\right]^{\mathrm{T}} \in \mathbb{C}^{(2N+1)\times 1}$, $\mathbf{C}^{-}_l = \left[c^{-}_{l,-N},\cdots,c^{-}_{l,0},\cdots,c^{-}_{l,N}\right]^{\mathrm{T}} \in \mathbb{C}^{(2N+1)\times 1}$, and $\mathbf{V}_l = \boldsymbol{\Upsilon}_l\mathbf{W}_l\mathbf{Q}_l$.

Here, $\mathbf{C}^{+}_l$ and $\mathbf{C}^{-}_l$ remain to be determined by matching the tangential electromagnetic fields at the boundaries of the layer, which is treated as a single layer. Denoting

$$\mathbf{Z}_{\mathrm{I},x} = \mathbf{K}_{\mathrm{I},x}/\varepsilon_{\mathrm{I},r} = \mathrm{diag}\left[k_{\mathrm{I},x,n}/(\varepsilon_{\mathrm{I},r}k_0)\right] \in \mathbb{C}^{(2N+1)\times(2N+1)}, \tag{A.56}$$

$$\mathbf{Z}_{\mathrm{II},x} = \mathbf{K}_{\mathrm{II},x}/\varepsilon_{\mathrm{II},r} = \mathrm{diag}\left[k_{\mathrm{II},x,n}/(\varepsilon_{\mathrm{II},r}k_0)\right] \in \mathbb{C}^{(2N+1)\times(2N+1)}, \tag{A.57}$$

$$\mathbf{X}_l = \mathrm{diag}(\mathrm{e}^{-k_0 q_{l,n} d_l}) \in \mathbb{C}^{(2N+1)\times(2N+1)}, \tag{A.58}$$

the boundary condition between the regions I and G, at $x = 0$, can be written as

$$\begin{bmatrix}\boldsymbol{\Gamma}_0 \\ \mathrm{i}\boldsymbol{\Gamma}_0\cos\theta/n_{\mathrm{I}}\end{bmatrix} + \begin{bmatrix}\mathbf{I} \\ -\mathrm{i}\mathbf{Z}_{\mathrm{I},x}\end{bmatrix}\mathbf{R} = \begin{bmatrix}\mathbf{W}_1\mathbf{X}_1 & \mathbf{W}_1 \\ \mathbf{V}_1\mathbf{X}_1 & -\mathbf{V}_1\end{bmatrix}\begin{bmatrix}\mathbf{C}^{+}_1 \\ \mathbf{C}^{-}_1\end{bmatrix}. \tag{A.59}$$

The boundary condition between the lth layer and the $(l+1)$th layer, at $x = D_l$, can be written as

$$\begin{bmatrix} \mathbf{W}_l & \mathbf{W}_l\mathbf{X}_l \\ \mathbf{V}_l & -\mathbf{V}_l\mathbf{X}_l \end{bmatrix} \begin{bmatrix} \mathbf{C}_l^+ \\ \mathbf{C}_l^- \end{bmatrix} = \begin{bmatrix} \mathbf{W}_{l+1}\mathbf{X}_{l+1} & \mathbf{W}_{l+1} \\ \mathbf{V}_{l+1}\mathbf{X}_{l+1} & -\mathbf{V}_{l+1} \end{bmatrix} \begin{bmatrix} \mathbf{C}_{l+1}^+ \\ \mathbf{C}_{l+1}^- \end{bmatrix}. \tag{A.60}$$

The boundary condition between the regions G and II, at $x = D_L$, can be written as

$$\begin{bmatrix} \mathbf{W}_L & \mathbf{W}_L\mathbf{X}_L \\ \mathbf{V}_L & -\mathbf{V}_L\mathbf{X}_L \end{bmatrix} \begin{bmatrix} \mathbf{C}_L^+ \\ \mathbf{C}_L^- \end{bmatrix} = \begin{bmatrix} \mathbf{I} \\ \mathrm{i}\mathbf{Z}_{\mathrm{II},x} \end{bmatrix} \mathbf{T}. \tag{A.61}$$

Combining Eqs. A.59, A.60 and A.61, we obtain

$$\begin{bmatrix} \mathbf{\Gamma}_0 \\ \mathrm{i}\mathbf{\Gamma}_0 \cos\theta / n_{\mathrm{I}} \end{bmatrix} + \begin{bmatrix} \mathbf{I} \\ -\mathrm{i}\mathbf{Z}_{\mathrm{I},x} \end{bmatrix} \mathbf{R} = \prod_{l=1}^{L} \begin{bmatrix} \mathbf{W}_l\mathbf{X}_l & \mathbf{W}_l \\ \mathbf{V}_l\mathbf{X}_l & -\mathbf{V}_l \end{bmatrix} \begin{bmatrix} \mathbf{W}_l & \mathbf{W}_l\mathbf{X}_l \\ \mathbf{V}_l & -\mathbf{V}_l\mathbf{X}_l \end{bmatrix}^{-1} \begin{bmatrix} \mathbf{I} \\ \mathrm{i}\mathbf{Z}_{\mathrm{II},x} \end{bmatrix} \mathbf{T}. \tag{A.62}$$

Denoting

$$\mathbf{g}_{L+1} = \mathbf{I}, \tag{A.63}$$

$$\mathbf{h}_{L+1} = \mathrm{i}\mathbf{Z}_{\mathrm{II},x}, \tag{A.64}$$

$$\mathbf{T}_{L+1} = \mathbf{T}, \tag{A.65}$$

then, Eq. A.62 can be rewritten as

$$\begin{bmatrix} \mathbf{\Gamma}_0 \\ \mathrm{i}\mathbf{\Gamma}_0 \cos\theta / n_{\mathrm{I}} \end{bmatrix} + \begin{bmatrix} \mathbf{I} \\ -\mathrm{i}\mathbf{Z}_{\mathrm{I},x} \end{bmatrix} \mathbf{R} = \prod_{l=1}^{L} \begin{bmatrix} \mathbf{W}_l\mathbf{X}_l & \mathbf{W}_l \\ \mathbf{V}_l\mathbf{X}_l & -\mathbf{V}_l \end{bmatrix} \begin{bmatrix} \mathbf{W}_l & \mathbf{W}_l\mathbf{X}_l \\ \mathbf{V}_l & -\mathbf{V}_l\mathbf{X}_l \end{bmatrix}^{-1} \begin{bmatrix} \mathbf{g}_{L+1} \\ \mathbf{h}_{L+1} \end{bmatrix} \mathbf{T}_{L+1}. \tag{A.66}$$

The Lth factor in the right-hand side of Eq. A.66 can be rewritten as

$$\begin{aligned} &\begin{bmatrix} \mathbf{W}_L\mathbf{X}_L & \mathbf{W}_L \\ \mathbf{V}_L\mathbf{X}_L & -\mathbf{V}_L \end{bmatrix} \begin{bmatrix} \mathbf{W}_L & \mathbf{W}_L\mathbf{X}_L \\ \mathbf{V}_L & -\mathbf{V}_L\mathbf{X}_L \end{bmatrix}^{-1} \begin{bmatrix} \mathbf{g}_{L+1} \\ \mathbf{h}_{L+1} \end{bmatrix} \mathbf{T}_{L+1} \\ &= \begin{bmatrix} \mathbf{W}_L\mathbf{X}_L & \mathbf{W}_L \\ \mathbf{V}_L\mathbf{X}_L & -\mathbf{V}_L \end{bmatrix} \begin{bmatrix} \mathbf{I} & 0 \\ 0 & \mathbf{X}_L \end{bmatrix}^{-1} \begin{bmatrix} \mathbf{W}_L & \mathbf{W}_L \\ \mathbf{V}_L & -\mathbf{V}_L \end{bmatrix}^{-1} \begin{bmatrix} \mathbf{g}_{L+1} \\ \mathbf{h}_{L+1} \end{bmatrix} \mathbf{T}_{L+1}. \end{aligned} \tag{A.67}$$

Introducing matrices

$$\begin{bmatrix} \mathbf{a}_L \\ \mathbf{b}_L \end{bmatrix} = \begin{bmatrix} \mathbf{W}_L & \mathbf{W}_L \\ \mathbf{V}_L & -\mathbf{V}_L \end{bmatrix}^{-1} \begin{bmatrix} \mathbf{g}_{L+1} \\ \mathbf{h}_{L+1} \end{bmatrix}, \tag{A.68}$$

and $\mathbf{T}_{L+1} = \mathbf{b}_L^{-1}\mathbf{X}_L\mathbf{T}_L$, the Lth factor in the right-hand side of Eq. A.66 reduces to

$$\begin{aligned}
&\begin{bmatrix} \mathbf{W}_L\mathbf{X}_L & \mathbf{W}_L \\ \mathbf{V}_L\mathbf{X}_L & -\mathbf{V}_L \end{bmatrix} \begin{bmatrix} \mathbf{I} & 0 \\ 0 & \mathbf{X}_L \end{bmatrix}^{-1} \begin{bmatrix} \mathbf{a}_L \\ \mathbf{b}_L \end{bmatrix} \mathbf{T}_{L+1} \\
&= \begin{bmatrix} \mathbf{W}_L \left(\mathbf{X}_L\mathbf{a}_L\mathbf{b}_L^{-1}\mathbf{X}_L + \mathbf{I}\right) \\ \mathbf{V}_L \left(\mathbf{X}_L\mathbf{a}_L\mathbf{b}_L^{-1}\mathbf{X}_L - \mathbf{I}\right) \end{bmatrix} \mathbf{T}_L \\
&= \begin{bmatrix} \mathbf{g}_L \\ \mathbf{h}_L \end{bmatrix} \mathbf{T}_L,
\end{aligned} \tag{A.69}$$

where

$$\begin{bmatrix} \mathbf{g}_L \\ \mathbf{h}_L \end{bmatrix} = \begin{bmatrix} \mathbf{W}_L \left(\mathbf{X}_L\mathbf{a}_L\mathbf{b}_L^{-1}\mathbf{X}_L + \mathbf{I}\right) \\ \mathbf{V}_L \left(\mathbf{X}_L\mathbf{a}_L\mathbf{b}_L^{-1}\mathbf{X}_L - \mathbf{I}\right) \end{bmatrix}. \tag{A.70}$$

We can then rewritten Eq. A.66 as

$$\begin{bmatrix} \mathbf{\Gamma}_0 \\ \mathrm{i}\mathbf{\Gamma}_0\cos\theta/n_\mathrm{I} \end{bmatrix} + \begin{bmatrix} \mathbf{I} \\ -\mathrm{i}\mathbf{Z}_{\mathrm{I},x} \end{bmatrix} \mathbf{R} = \prod_{l=1}^{L-1} \begin{bmatrix} \mathbf{W}_l\mathbf{X}_l & \mathbf{W}_l \\ \mathbf{V}_l\mathbf{X}_l & -\mathbf{V}_l \end{bmatrix} \begin{bmatrix} \mathbf{W}_l & \mathbf{W}_l\mathbf{X}_l \\ \mathbf{V}_l & -\mathbf{V}_l\mathbf{X}_l \end{bmatrix}^{-1} \begin{bmatrix} \mathbf{g}_L \\ \mathbf{h}_L \end{bmatrix} \mathbf{T}_L. \tag{A.71}$$

Repeating the process [Eqs. A.67–A.73] for the other layers ($l = L-1, \ldots, 1$), we obtain the metrics $\mathbf{T}_l$, $\mathbf{a}_l$, $\mathbf{b}_l$, $\mathbf{g}_l$, $\mathbf{h}_l$, equations

$$\begin{bmatrix} \mathbf{\Gamma}_0 \\ \mathrm{i}\mathbf{\Gamma}_0\cos\theta/n_\mathrm{I} \end{bmatrix} + \begin{bmatrix} \mathbf{I} \\ -\mathrm{i}\mathbf{Z}_{\mathrm{I},x} \end{bmatrix} \mathbf{R} = \begin{bmatrix} \mathbf{g}_1 \\ \mathbf{h}_1 \end{bmatrix} \mathbf{T}_1, \tag{A.72}$$

and

$$\begin{bmatrix} \mathbf{g}_l \\ \mathbf{h}_l \end{bmatrix} \mathbf{T}_l = \begin{bmatrix} \mathbf{W}_l\mathbf{X}_l & \mathbf{W}_l \\ \mathbf{V}_l\mathbf{X}_l & -\mathbf{V}_l \end{bmatrix} \begin{bmatrix} \mathbf{W}_l & \mathbf{W}_l\mathbf{X}_l \\ \mathbf{V}_l & -\mathbf{V}_l\mathbf{X}_l \end{bmatrix}^{-1} \begin{bmatrix} \mathbf{g}_{l+1} \\ \mathbf{h}_{l+1} \end{bmatrix} \mathbf{T}_{l+1} \tag{A.73}$$

$$= \prod_{d=l}^{L} \begin{bmatrix} \mathbf{W}_l\mathbf{X}_l & \mathbf{W}_l \\ \mathbf{V}_l\mathbf{X}_l & -\mathbf{V}_l \end{bmatrix} \begin{bmatrix} \mathbf{W}_l & \mathbf{W}_l\mathbf{X}_l \\ \mathbf{V}_l & -\mathbf{V}_l\mathbf{X}_l \end{bmatrix}^{-1} \begin{bmatrix} \mathbf{g}_{L+1} \\ \mathbf{h}_{L+1} \end{bmatrix} \mathbf{T}_{L+1}. \tag{A.74}$$

The solution for $\mathbf{R}$ and $\mathbf{T}_1$ can be given by

$$\mathbf{R} = \mathbf{g}_1 \left[\mathrm{i}\mathbf{Z}_{\mathrm{I},x}\mathbf{g}_1 + \mathbf{h}_1\right]^{-1} \left[\mathrm{i}\mathbf{Z}_{\mathrm{I},x} + \mathrm{i}\frac{\cos\theta}{n_\mathrm{I}}\right] \mathbf{\Gamma}_0 - \mathbf{\Gamma}_0, \tag{A.75}$$

$$\mathbf{T}_1 = \left[\mathrm{i}\mathbf{Z}_{\mathrm{I},x}\mathbf{g}_1 + \mathbf{h}_1\right]^{-1} \left[\mathrm{i}\mathbf{Z}_{\mathrm{I},x} + \mathrm{i}\frac{\cos\theta}{n_\mathrm{I}}\right] \mathbf{\Gamma}_0. \tag{A.76}$$

The matrix of transmission coefficients $\mathbf{T}$ can be given by

$$\mathbf{T} = \mathbf{T}_{L+1} = \mathbf{b}_L^{-1}\mathbf{X}_L \cdots \mathbf{b}_1^{-1}\mathbf{X}_1\mathbf{T}_1. \tag{A.77}$$

Based on Eq. A.60, and A.69, the matrices $\mathbf{C}_l^+$ and $\mathbf{C}_l^-$ can be expressed as

$$\begin{aligned}
\begin{bmatrix}\mathbf{C}_l^+\\ \mathbf{C}_l^-\end{bmatrix} &= \begin{bmatrix}\mathbf{W}_l & \mathbf{W}_l\mathbf{X}_l\\ \mathbf{V}_l & -\mathbf{V}_l\mathbf{X}_l\end{bmatrix}^{-1}\begin{bmatrix}\mathbf{g}_{l+1}\\ \mathbf{h}_{l+1}\end{bmatrix}\mathbf{T}_{l+1}\\
&= \begin{bmatrix}\mathbf{I} & 0\\ 0 & \mathbf{X}_l\end{bmatrix}^{-1}\begin{bmatrix}\mathbf{W}_l & \mathbf{W}_l\\ \mathbf{V}_l & -\mathbf{V}_l\end{bmatrix}^{-1}\begin{bmatrix}\mathbf{g}_{l+1}\\ \mathbf{h}_{l+1}\end{bmatrix}\mathbf{T}_{l+1}\\
&= \begin{bmatrix}\mathbf{I} & 0\\ 0 & \mathbf{X}_l\end{bmatrix}^{-1}\begin{bmatrix}\mathbf{a}_l\\ \mathbf{b}_l\end{bmatrix}\mathbf{T}_{l+1}\\
&= \begin{bmatrix}\mathbf{a}_l\mathbf{b}_l^{-1}\mathbf{X}_l\\ \mathbf{I}\end{bmatrix}\mathbf{T}_l.
\end{aligned} \tag{A.78}$$

As a result, all the fields can be calculated with Eqs. A.42– A.44, A.54–A.55.

In the simulation of single-grating structure, the electrons interact with the fields in the region I or II. In the region I, the amplitudes of the spatial harmonics can be given in matrix form

$$\mathbf{H}_y^{\mathrm{I}}(x) = \mathrm{diag}\left[\mathrm{diag}\left(\mathrm{e}^{-\mathrm{i}\mathbf{K}_{\mathrm{I},x}x'}\right)\right]\mathbf{R}, \tag{A.79}$$

$$\mathbf{E}_z^{\mathrm{I}}(x) = \frac{1}{\varepsilon_{\mathrm{I},r}}\sqrt{\frac{\mu_0}{\varepsilon_0}}\mathbf{K}_{\mathrm{I},x}\mathrm{diag}\left[\mathrm{diag}\left(\mathrm{e}^{-\mathrm{i}\mathbf{K}_{\mathrm{I},x}x'}\right)\right]\mathbf{R}, \tag{A.80}$$

$$\mathbf{E}_x^{\mathrm{I}}(x) = \frac{1}{\varepsilon_{\mathrm{I},r}}\sqrt{\frac{\mu_0}{\varepsilon_0}}\mathbf{K}_z\mathrm{diag}\left[\mathrm{diag}\left(\mathrm{e}^{-\mathrm{i}\mathbf{K}_{\mathrm{I},x}x'}\right)\right]\mathbf{R}. \tag{A.81}$$

In region II, the amplitudes of the spatial harmonics can be given in matrix form

$$\mathbf{H}_y^{\mathrm{II}}(x) = \mathrm{diag}\left[\mathrm{diag}\left(\mathrm{e}^{\mathrm{i}\mathbf{K}_{\mathrm{II},x}(x'-k_0D)}\right)\right]\mathbf{T}, \tag{A.82}$$

$$\mathbf{E}_z^{\mathrm{II}}(x) = -\frac{1}{\varepsilon_{\mathrm{II},r}}\sqrt{\frac{\mu_0}{\varepsilon_0}}\mathbf{K}_{\mathrm{II},x}\mathrm{diag}\left[\mathrm{diag}\left(\mathrm{e}^{\mathrm{i}\mathbf{K}_{\mathrm{II},x}(x'-k_0D)}\right)\right]\mathbf{T}, \tag{A.83}$$

$$\mathbf{E}_x^{\mathrm{II}}(x) = \frac{1}{\varepsilon_{\mathrm{II},r}}\sqrt{\frac{\mu_0}{\varepsilon_0}}\mathbf{K}_z\mathrm{diag}\left[\mathrm{diag}\left(\mathrm{e}^{\mathrm{i}\mathbf{K}_{\mathrm{II},x}(x'-k_0D)}\right)\right]\mathbf{T}. \tag{A.84}$$

In the simulation of dual-grating structure, the electrons interact with the fields in the vacuum channel. Assuming the vacuum channel is the sth layer, the electric amplitudes of the spatial harmonics in the vacuum channel can be given in the form

$$\mathbf{H}_{y,s}^{\mathrm{G}}(x) = \mathbf{U}_s(x) = \mathbf{W}_s\left[\mathbf{Y}_s^+(x)\mathbf{C}_s^+ + \mathbf{Y}_s^-(x)\mathbf{C}_s^-\right], \tag{A.85}$$

$$\mathbf{E}_{z,s}^{\mathrm{G}}(x) = \mathrm{i}\sqrt{\frac{\mu_0}{\varepsilon_0}}\frac{1}{\varepsilon_s(z)}\mathbf{W}_s\mathbf{Q}_s\left[\mathbf{Y}_s^+(x)\mathbf{C}_s^+ + \mathbf{Y}_s^-(x)\mathbf{C}_s^-\right], \tag{A.86}$$

$$\mathbf{E}_{x,s}^{\mathrm{G}}(x) = \sqrt{\frac{\mu_0}{\varepsilon_0}}\frac{1}{\varepsilon_s(z)}\mathbf{K}_z\mathbf{W}_s\left[\mathbf{Y}_s^+(x)\mathbf{C}_s^+ + \mathbf{Y}_s^-(x)\mathbf{C}_s^-\right]. \tag{A.87}$$

In Fig. A.2, we compare the accelerating gradient (the amplitude of the first diffraction order) at a distance of 50 nm, calculated by RCWA method and CST. It shows that the results obtained with RCWA method are in agreement with the results obtained with CST.

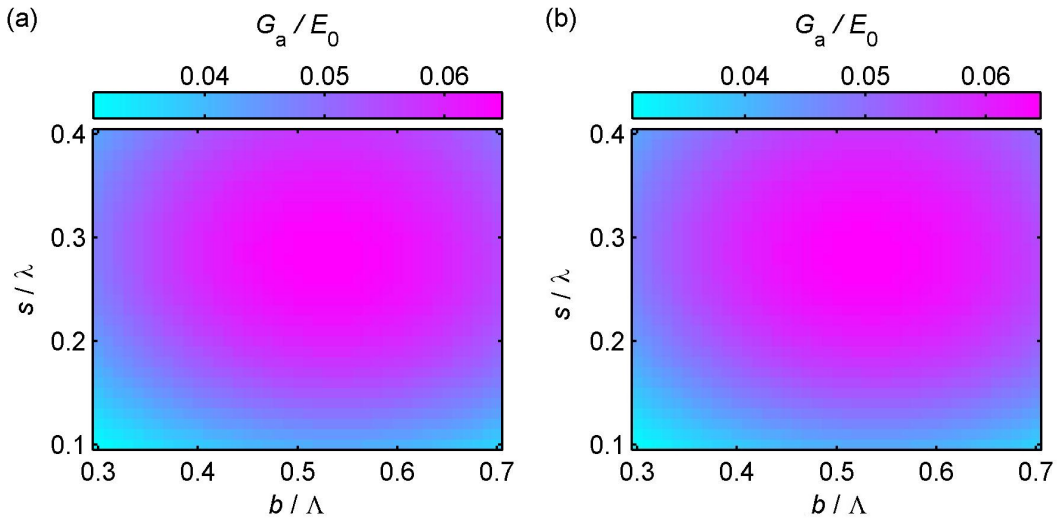

FIGURE A.2: $s - b$ maps of the accelerating gradient obtained from CST (a) and RCWA (b). s is the grating pillar height, b the pillar width, Λ the grating period, and λ the laser wavelength. Figure (a) is identical to Fig. 2.7.

Bibliography

[1] Gustaf Ising. Prinzip einer methode zur herstellung von kanalstrahlen hoher voltzahl. *Arkiv for Matematik, Astronomi och Fysik*, 18:1–4, 1924.

[2] Thomas P Wangler. *RF Linear accelerators*. John Wiley & Sons, 2008.

[3] Luis W Alvarez. The design of a proton linear accelerator. In *Physical Review*, volume 70, pages 799–800, 1946.

[4] Luis W Alvarez, Hugh Bradner, Jack V Franck, Hayden Gordon, J Donald Gow, Lauriston C Marshall, Frank Oppenheimer, Wolfgang KH Panofsky, Chaim Richman, and John R Woodyard. Berkeley proton linear accelerator. *Review of Scientific Instruments*, 26(2):111–133, 1955.

[5] Bruce Cork. Proton linear-accelerator injector for the bevatron. *Review of Scientific Instruments*, 26(2):210–219, 1955.

[6] Toshiyasu Higo, Riccardo Zennaro, Chris Adolphsen, Lisa Laurent, Steffen Dobert, Alexej Grudiev, Germana Riddone, Aaron Jensen, Juwen Wang, Sami Tantawi, et al. Advances in x-band tw accelerator structures operating in the 100 mv/m regime. In *Proceeding of IPAC 2010, Kyoto, Japan*, pages 3702–3704, 2010.

[7] Hasan Padamsee. 50 years of success for srf accelerators-a review. *Superconductor Science and Technology*, 30(5):053003, 2017.

[8] Hasan S Padamsee. Superconducting radio-frequency cavities. *Annual Review of Nuclear and Particle Science*, 64:175–196, 2014.

[9] Satomi Shiraishi. *Investigation of Staged Laser-Plasma Acceleration*. Springer, 2014.

[10] E Esarey, CB Schroeder, and WP Leemans. Physics of laser-driven plasma-based electron accelerators. *Reviews of Modern Physics*, 81(3):1229, 2009.

[11] Victor Malka, S Fritzler, E Lefebvre, M-M Aleonard, F Burgy, J-P Chambaret, J-F Chemin, K Krushelnick, G Malka, SPD Mangles, et al. Electron acceleration by a

wake field forced by an intense ultrashort laser pulse. *Science*, 298(5598):1596–1600, 2002.

[12] D Guénot, D Gustas, A Vernier, B Beaurepaire, F Böhle, M Bocoum, M Lozano, A Jullien, R Lopez-Martens, Agustin Lifschitz, et al. Relativistic electron beams driven by khz single-cycle light pulses. *Nature Photonics*, 11(5):293, 2017.

[13] Jérôme Faure, Yannick Glinec, A Pukhov, S Kiselev, S Gordienko, E Lefebvre, J-P Rousseau, F Burgy, and Victor Malka. A laser–plasma accelerator producing monoenergetic electron beams. *Nature*, 431(7008):541, 2004.

[14] CGR Geddes, Cs Toth, J Van Tilborg, E Esarey, CB Schroeder, D Bruhwiler, C Nieter, J Cary, and WP Leemans. High-quality electron beams from a laser wakefield accelerator using plasma-channel guiding. *Nature*, 431(7008):538, 2004.

[15] Stuart PD Mangles, CD Murphy, Zulfikar Najmudin, Alexander George Roy Thomas, JL Collier, Aboobaker E Dangor, EJ Divall, PS Foster, JG Gallacher, CJ Hooker, et al. Monoenergetic beams of relativistic electrons from intense laser–plasma interactions. *Nature*, 431(7008):535, 2004.

[16] WP Leemans, AJ Gonsalves, H-S Mao, K Nakamura, C Benedetti, CB Schroeder, Cs Tóth, J Daniels, DE Mittelberger, SS Bulanov, et al. Multi-gev electron beams from capillary-discharge-guided subpetawatt laser pulses in the self-trapping regime. *Physical review letters*, 113(24):245002, 2014.

[17] Sébastien Corde, E Adli, JM Allen, W An, CI Clarke, CE Clayton, JP Delahaye, J Frederico, S Gessner, SZ Green, et al. Multi-gigaelectronvolt acceleration of positrons in a self-loaded plasma wakefield. *Nature*, 524(7566):442, 2015.

[18] S Steinke, J Van Tilborg, C Benedetti, CGR Geddes, CB Schroeder, J Daniels, KK Swanson, AJ Gonsalves, K Nakamura, NH Matlis, et al. Multistage coupling of independent laser-plasma accelerators. *Nature*, 530(7589):190, 2016.

[19] R Joel England, Robert J Noble, Karl Bane, David H Dowell, Cho-Kuen Ng, James E Spencer, Sami Tantawi, Ziran Wu, Robert L Byer, Edgar Peralta, et al. Dielectric laser accelerators. *Reviews of Modern Physics*, 86(4):1337, 2014.

[20] John Breuer and Peter Hommelhoff. Laser-based acceleration of nonrelativistic electrons at a dielectric structure. *Physical Review Letters*, 111(13):134803, 2013.

[21] E A Peralta, K Soong, R Joel England, E R Colby, Z Wu, B Montazeri, C McGuinness, J McNeur, K J Leedle, D Walz, et al. Demonstration of electron acceleration in a laser-driven dielectric microstructure. *Nature*, 503(7474):91, 2013.

[22] BC Stuart, MD Feit, AM Rubenchik, BW Shore, and MD Perry. Laser-induced damage in dielectrics with nanosecond to subpicosecond pulses. *Physical review letters*, 74(12):2248, 1995.

[23] Y Takeda and I Matsui. Laser linac with grating. *Nuclear Instruments and Methods*, 62(3):306–310, 1968.

[24] K Mizuno, J Pae, T Nozokido, and K Furuya. Experimental evidence of the inverse smith–purcell effect. *Nature*, 328(6125):45, 1987.

[25] Joshua McNeur, Martin Kozak, Dominik Ehberger, Norbert Schönenberger, Alexander Tafel, Ang Li, and Peter Hommelhoff. A miniaturized electron source based on dielectric laser accelerator operation at higher spatial harmonics and a nanotip photoemitter. *Journal of Physics B: Atomic, Molecular and Optical Physics*, 49(3):034006, 2016.

[26] Kenneth J Leedle, R Fabian Pease, Robert L Byer, and James S Harris. Laser acceleration and deflection of 96.3 kev electrons with a silicon dielectric structure. *Optica*, 2(2):158–161, 2015.

[27] M Kozák, M Förster, J McNeur, N Schönenberger, K Leedle, H Deng, JS Harris, RL Byer, and P Hommelhoff. Dielectric laser acceleration of sub-relativistic electrons by few-cycle laser pulses. *Nuclear Instruments and Methods in Physics Research Section A: Accelerators, Spectrometers, Detectors and Associated Equipment*, 865:84–86, 2017.

[28] Joshua McNeur, Martin Kozák, Norbert Schönenberger, Kenneth J Leedle, Huiyang Deng, Andrew Ceballos, Heinar Hoogland, Axel Ruehl, Ingmar Hartl, Ronald Holzwarth, et al. Elements of a dielectric laser accelerator. *arXiv preprint arXiv:1604.07684*, 2016.

[29] Kenneth J Leedle, Andrew Ceballos, Huiyang Deng, Olav Solgaard, R Fabian Pease, Robert L Byer, and James S Harris. Dielectric laser acceleration of sub-100 kev electrons with silicon dual-pillar grating structures. *Optics Letters*, 40(18):4344–4347, 2015.

[30] Kenneth J Leedle, Dylan S Black, Yu Miao, Karel E Urbanek, Andrew Ceballos, Huiyang Deng, James S Harris, Olav Solgaard, and Robert L Byer. Phase-dependent laser acceleration of electrons with symmetrically driven silicon dual pillar gratings. *Optics letters*, 43(9):2181–2184, 2018.

[31] Xintian Eddie Lin. Photonic band gap fiber accelerator. *Physical Review Special Topics - Accelerators and Beams*, 4(5):051301, 2001.

[32] Amit Mizrahi and Levi Schächter. Optical bragg accelerators. *Physical Review E*, 70(1):016505, 2004.

[33] Amit Mizrahi and Levi Schächter. Bragg reflection waveguides with a matching layer. *Optics express*, 12(14):3156–3170, 2004.

[34] Benjamin M Cowan. Two-dimensional photonic crystal accelerator structures. *Physical Review Special Topics-Accelerators and Beams*, 6(10):101301, 2003.

[35] Benjamin M Cowan. Three-dimensional dielectric photonic crystal structures for laser-driven acceleration. *Physical Review Special Topics-Accelerators and Beams*, 11(1):011301, 2008.

[36] M Kozák, P Beck, H Deng, J McNeur, N Schönenberger, C Gaida, F Stutzki, M Gebhardt, J Limpert, A Ruehl, et al. Acceleration of sub-relativistic electrons with an evanescent optical wave at a planar interface. *Optics Express*, 25(16): 19195–19204, 2017.

[37] DA Walsh, DS Lake, EW Snedden, MJ Cliffe, DM Graham, and SP Jamison. Demonstration of sub-luminal propagation of single-cycle terahertz pulses for particle acceleration. *Nature communications*, 8(1):421, 2017.

[38] Huiyang Deng, Jiaqi Jiang, Yu Miao, Kenneth J Leedle, Hongquan Li, Olav Solgaard, Robert L Byer, and James S Harris. Design of racetrack ring resonator based dielectric laser accelerators. *arXiv preprint arXiv:1701.08945*, 2017.

[39] Peter Baum and Ahmed H Zewail. Breaking resolution limits in ultrafast electron diffraction and microscopy. *Proceedings of the National Academy of Sciences*, 103 (44):16105–16110, 2006.

[40] Mitsuru Uesaka and Kazuyoshi Koyama. Advanced accelerators for medical applications. *Reviews of Accelerator Science and Technology*, 09:235–260, 2016.

[41] Li Lan, Satoshi Nakajima, Kenshi Komatsu, Andre Nussenzweig, Akira Shimamoto, Junko Oshima, and Akira Yasui. Accumulation of werner protein at dna double-strand breaks in human cells. *Journal of cell science*, 118(18):4153–4162, 2005.

[42] Li Lan, Satoshi Nakajima, Yoshitsugu Oohata, Masashi Takao, Satoshi Okano, Mitsuko Masutani, Samuel H Wilson, and Akira Yasui. In situ analysis of repair processes for oxidative dna damage in mammalian cells. *Proceedings of the National Academy of Sciences of the United States of America*, 101(38):13738–13743, 2004.

[43] Kazuyoshi Koyama, Shohei Otsuki, Mitsuru Uesaka, Mitsuhiro Yoshida, and Aimiding Aimidula. Parameter study of a laser-driven dielectric accelerator for radiobiology research. *Journal of Physics B: Atomic, Molecular and Optical Physics*, 47 (23):234005, 2014.

[44] Dominik Ehberger, Jakob Hammer, Max Eisele, Michael Krüger, Jonathan Noe, Alexander Högele, and Peter Hommelhoff. Highly coherent electron beam from a laser-triggered tungsten needle tip. *Physical review letters*, 114(22):227601, 2015.

[45] Tatsunori Shibuya, Noriyosu Hayashizaki, and Mitsuhiro Yoshida. Fabrication of two dimensional nano-scale photocathode arrays in transparent conductor for high coherence beam generation. In *Proceedings of IPAC 2016, Busan, Korea*, pages 2645–2647, 2016.

[46] URL `https://www.cst.com`.

[47] John Breuer, Roswitha Graf, Alexander Apolonski, and Peter Hommelhoff. Dielectric laser acceleration of nonrelativistic electrons at a single fused silica grating structure: Experimental part. *Physical Review Special Topics-Accelerators and Beams*, 17(2):021301, 2014.

[48] Kenneth J Leedle. *Laser acceleration and deflection of sub-100 keV electrons with silicon dielectric laser accelerator structures*. PhD thesis, Stanford University, 2016.

[49] Eric Esarey, Phillip Sprangle, and Jonathan Krall. Laser acceleration of electrons in vacuum. *Physical Review E*, 52(5):5443, 1995.

[50] Zhaofu Chen, Kazuyoshi Koyama, Mitsuru Uesaka, Mitsuhiro Yoshida, and Rui Zhang. Resonant enhancement of accelerating gradient with silicon dual-grating structure for dielectric laser acceleration of subrelativistic electrons. *Applied Physics Letters*, 112(3):034102, 2018.

[51] Carlos FR Mateus, Michael CY Huang, Lu Chen, Connie J Chang-Hasnain, and Yuri Suzuki. Broad-band mirror (1.12-1.62/spl mu/m) using a subwavelength grating. *IEEE Photonics Technology Letters*, 16(7):1676–1678, 2004.

[52] Carlos FR Mateus, Michael CY Huang, Yunfei Deng, Andrew R Neureuther, and Connie J Chang-Hasnain. Ultrabroadband mirror using low-index cladded subwavelength grating. *IEEE Photonics Technology Letters*, 16(2):518–520, 2004.

[53] Michael CY Huang, Y Zhou, and Connie J Chang-Hasnain. A surface-emitting laser incorporating a high-index-contrast subwavelength grating. *Nature Photonics*, 1(2): 119–122, 2007.

[54] Corrado Sciancalepore, B Ben Bakir, Xavier Letartre, Julie Harduin, Nicolas Olivier, Christian Seassal, Jean-Marc Fedeli, and Pierre Viktorovitch. Cmos-compatible ultra-compact 1.55-μm emitting vcsels using double photonic crystal mirrors. *IEEE Photonics Technology Letters*, 24(5):455, 2012.

[55] Thilo Stoferle, Nikolaj Moll, Thorsten Wahlbrink, Jens Bolten, Thomas Mollenhauer, Ullrich Scherf, and Rainer F Mahrt. Ultracompact silicon/polymer laser with an absorption-insensitive nanophotonic resonator. *Nano Letters*, 10(9):3675–3678, 2010.

[56] Alireza Taghizadeh, Jesper Mørk, and Il-Sug Chung. Vertical-cavity in-plane heterostructures: Physics and applications. *Applied Physics Letters*, 107(18):181107, 2015.

[57] Zhaorong Wang, Bo Zhang, and Hui Deng. Dispersion engineering for vertical microcavities using subwavelength gratings. *Physical Review Letters*, 114(7):073601, 2015.

[58] Weijian Yang, James Ferrara, Karen Grutter, Anthony Yeh, Chris Chase, Yang Yue, Alan E Willner, Ming C Wu, and Connie J Chang-Hasnain. Low loss hollow-core waveguide on a silicon substrate. *Nanophotonics*, 1(1):23–29, 2012.

[59] Ye Zhou, Vadim Karagodsky, Bala Pesala, Forrest G Sedgwick, and Connie J Chang-Hasnain. A novel ultra-low loss hollow-core waveguide using subwavelength high-contrast gratings. *Optics Express*, 17(3):1508–1517, 2009.

[60] Connie J Chang-Hasnain and Weijian Yang. High-contrast gratings for integrated optoelectronics. *Advances in Optics and Photonics*, 4(3):379–440, 2012.

[61] Alireza Taghizadeh, Gyeong Cheol Park, Jesper Mørk, and Il-Sug Chung. Hybrid grating reflector with high reflectivity and broad bandwidth. *Optics Express*, 22 (18):21175–21184, 2014.

[62] Edgar Armando Peralta. *Accelerator on a chip: design, fabrication, and demonstration of grating-based dielectric microstructures for laser-driven acceleration of electrons*. PhD thesis, Stanford University, 2015.

[63] Tyler W Hughes, Si Tan, Zhexin Zhao, Neil V Sapra, Kenneth J Leedle, Huiyang Deng, Yu Miao, Dylan S Black, Olav Solgaard, James S Harris, et al. On-chip laser-power delivery system for dielectric laser accelerators. *Physical Review Applied*, 9 (5):054017, 2018.

[64] Nur Ismail, Cristine Calil Kores, Dimitri Geskus, and Markus Pollnau. Fabry-pérot resonator: spectral line shapes, generic and related airy distributions, linewidths,

finesses, and performance at low or frequency-dependent reflectivity. *Optics Express*, 24(15):16366–16389, 2016.

[65] Vadim Karagodsky, Forrest G Sedgwick, and Connie J Chang-Hasnain. Theoretical analysis of subwavelength high contrast grating reflectors. *Optics Express*, 18(16): 16973–16988, 2010.

[66] M. G. Moharam, T. K. Gaylord, Drew A Pommet, and Eric B Grann. Stable implementation of the rigorous coupled-wave analysis for surface-relief gratings: enhanced transmittance matrix approach. *Journal of the Optical Society of America A*, 12(5):1077–1086, 1995.

[67] Samuel Earnshaw. On the nature of the molecular forces which regulate the constitution of the luminferous ether. *Transactions of the Cambridge Philosophical Society*, 7:97–112, 1842.

[68] T Plettner, P P Lu, and R L Byer. Proposed few-optical cycle laser-driven particle accelerator structure. *Physical Review Special Topics - Accelerators and Beams*, 9 (11):111301, 2006.

[69] R. H. Siemann. Energy efficiency of laser driven, structure based accelerators. *Physical Review Special Topics - Accelerators and Beams*, 7(6):061303, 2004.

[70] Y. C. Neil Na, R. H. Siemann, and R. L. Byer. Energy efficiency of an intracavity coupled, laser-driven linear accelerator pumped by an external laser. *Physical Review Special Topics - Accelerators and Beams*, 8:031301, Mar 2005.

[71] Carl A Bauer, Gregory R Werner, and John R Cary. Truncated photonic crystal cavities with optimized mode confinement. *Journal of Applied Physics*, 104(5): 053107, 2008.

[72] Emiliano Di Gennaro, C Zannini, S Savo, A Andreone, MR Masullo, G Castaldi, I Gallina, and V Galdi. Hybrid photonic-bandgap accelerating cavities. *New Journal of Physics*, 11(11):113022, 2009.

[73] Steven G Johnson and John D Joannopoulos. Block-iterative frequency-domain methods for maxwell's equations in a planewave basis. *Optics express*, 8(3):173–190, 2001.

[74] Adi Hanuka, Elron Goldemberg, Almog Zilka, and Levi Schächter. Metamaterials for optical bragg accelerators. *Applied Physics Letters*, 112(10):101902, 2018.

[75] Levi Schächter, RL Byer, and RH Siemann. Wake field in dielectric acceleration structures. *Physical Review E*, 68(3):036502, 2003.

[76] Kazuyoshi Koyama, Zhaofu Chen, Hayato Okamoto, Mitsuru Uesaka, and Mitsuhiro Yoshida. Development of a laser driven dielectric accelerator for radiobiology research. In *Proceeding of IPAC 2017, Copenhagen, Denmark*, pages 3272–3274, 2017.

[77] Stanley Humphries. *Principles of charged particle acceleration*. Courier Corporation, 2013.

[78] Brent Fultz and James M Howe. *Transmission electron microscopy and diffractometry of materials*. Springer Science & Business Media, 2012.

[79] T Kalvas. Beam extraction and transport. *arXiv preprint arXiv:1401.3951*, 2014.

[80] Paul Bounin. Application of fermat's principle to magnetic spectrometers. *Review of Scientific Instruments*, 38(9):1305–1312, 1967.

[81] I Chavet and M Menat. Focal plane slope of a homogeneous magnetic sector. *Nuclear Instruments and Methods*, 99(1):115–119, 1972.

[82] Jack T.. Tanabe. *Iron Dominated Electromagnets: Design, Fabrication, Assembly and Measurements*. World Scientific, 2005.

[83] T Shibuya. *Coherent microscopy based on ultra-fine electron beam*. PhD thesis, Tokyo Institute of Technology, 2017.

[84] M. G. Moharam and T. K. Gaylord. Rigorous coupled-wave analysis of planar-grating diffraction. *Journal of the Optical Society of America*, 71(7):811–818, 1981.

[85] M. G. Moharam and T. K. Gaylord. Rigorous coupled-wave analysis of grating diffraction–e-mode polarization and losses. *Journal of the Optical Society of America*, 73(4):451–455, 1983.

[86] M. G. Moharam and T. K. Gaylord. Three-dimensional vector coupled-wave analysis of planar-grating diffraction. *Journal of the Optical Society of America*, 73(9): 1105–1112, 1983.

[87] John J Hench and Zdeněk Strakoš. The rcwa method–a case study with open questions and perspectives of algebraic computations. *Electronic Transactions on Numerical Analysis*, 31:331–357, 2008.

[88] M. G. Moharam and T. K. Gaylord. Diffraction analysis of dielectric surface-relief gratings. *Journal of the Optical Society of America*, 72(10):1385–1392, 1982.

[89] M. G. Moharam and T. K. Gaylord. Rigorous coupled-wave analysis of metallic surface-relief gratings. *Journal of the Optical Society of America A*, 3(11):1780–1787, 1986.

[90] M. G. Moharam. Coupled-wave analysis of two-dimensional dielectric gratings. In I. Cindrich, editor, *Holographic Optics: Design and Applications*, volume 883, pages 8–12. International Society for Optics and Photonics, 1988.